A Geometallurgical Approach to Assessing Critical Metal Mobility and Recoverability from Ultramafic Mine Tailings

by

Makoto Jamieson Honda-McNeil

A thesis submitted in partial fulfillment of the requirements for the degree of

Master of Science

Department of Earth & Atmospheric Sciences

University of Alberta

ABSTRACT

Critical metals (e.g., nickel and cobalt) are increasingly in demand for the production and storage of cleaner energy but their supplies are finite. Ultramafic mine tailings could be reprocessed as a source of critical metals. These waste materials host an array of critical transition metals and can sequester atmospheric carbon during weathering. However, the partitioning behavior of nickel and cobalt between mineral phases and the abundances of these metals in ultramafic tailings and greenfield ore deposits is imprecisely known. Ultramafic tailings and ore from post-mining (Lord Brassey, Tasmania) and pre-mining (Record Ridge, British Columbia) settings were analyzed in order to observe the behavior of critical transition metals over the mining lifecycle. X-ray diffraction (XRD) supplemented by scanning electron microscopy (SEM) with energy dispersive X-ray spectroscopy (EDS) were used to identify widespread sulfides, oxides and alloys, which host numerous critical transition metals. Raman spectroscopy was used to identify amorphous carbonate and iron oxyhydroxide minerals, which sequester these metals upon alteration and weathering, and X-ray fluorescence microscopy (XFM) displayed an increase in the concentration of nickel and cobalt in weathered and sulfide-rich zones. The integration of quantitative X-ray diffraction (QXRD) and electron probe micro-analysis (EPMA) data from the Lord Brassey samples was used to (1) determine that these tailings qualify as low-grade nickel and cobalt ore and (2) produce an analytical tool for accurate calculation of whole rock elemental abundances that provides supplementary mineralogical abundances and compositions. This methodology produced results comparable to an industry whole rock analysis and provides a better understanding of mineralogy, stoichiometry and the grade of tailings with general applicability to geometallurgical assessments of tailings and ore. The results of this thesis indicate there is merit

in reprocessing ultramafic mine tailings for nickel and cobalt and we suggest that tailings storage facilities could be incorporated into the ore processing circuit as part of mine plans.

PREFACE

This thesis is an original work by Makoto Jamieson Honda-McNeil. No part of this thesis has been previously published.

DEDICATION

"Boys, be ambitious! Be ambitious not for money or for selfish aggrandizement, not for that evanescent thing which men call fame. Be ambitious for that attainment of all that a man ought to be."

-Dr. William S. Clark to the students of Sapporo Agricultural College (now Hokkaido University) upon his departure from Japan, April 16, 1877.

"When you're old you don't want to be thinking about the things you didn't do"
"Yeah but you want to be thinking about the things you DID do"

-Jukka Hildén & Jarppi Leppälä, Season 1, Episode 1 of The Dudesons.

"You make yourself"

-Toyoaki Honda (my grandfather) to me, multiple times throughout our dinner conversations.

"My soul is tormented! I've been up and down the four corners of this big old world! I've seen it all! I've done it all! I've fought many a good man, and laid many a good woman! I've had riches and fame and adventure...I've tasted life to the fullest, and still my heart cries out, yes, cries out in this hungry, tortured, wrecked quest: 'More!"

-Fritz the Cat, 1972

ACKNOWLEDGEMENTS

First, I would like to thank my supervisor Dr. Sasha Wilson for the guidance and support throughout my degree. You would be hard-pressed to find a more compassionate, giving, enthusiastic, patient and understanding individual, not just as a supervisor. I will not forget the kindness you have shown me, nor the endless stream of opportunities you threw at me. I would also like to thank my adopted co-supervisor Dr. Andrew Locock for overseeing the EPMA work and coaching me through the data integration, error propagation and thesis writing. I am extremely grateful for the knowledge and criticism throughout the process, allowing me to barge into your lab at a moment's notice, and going out of your way to ensure I was on the right track.

I would like to acknowledge the funding sources that made this project possible, including the Natural Sciences and Engineering Research Council of Canada (NSERC) Discovery Grants program, the Natural Resources Canada Clean Growth Program and the Canada Research Chairs Program. Numerous individuals were also involved in this project who I would like to acknowledge. Thank you to Dr. Nathan Gerein and Guibin Ma for their extreme patience and guidance with the SEM work. Thank you to Rebecca Funk for performing XRD analysis on my samples and thanks to Dr. Matthew Steele-MacInnis, Marko Szmihelsky and Spencer Poulette for their assistance with the Raman spectroscopy. Special thanks to Dr. Jessica Hamilton, Dr. Daryl Howard, Dr. David Paterson, Dr. Gord Southam, Jordan Poitras and Thomas Jones for their assistance with the remote synchrotron data collection and processing my XFM and XANES data. Thanks to Mark Labbe and Walter Harley at the U of A thin section lab and Vancouver Petrographics for thin section preparation and thanks to SGS Minerals for the whole rock analysis. Thanks to Dr. Simon Jowitt, Dr. Connor Turvey and Ben Mililli for their part in the Lord Brassey fieldwork and thank you to Frank Marasco, Tom Jones and Daralyn Fox of WHY Resources for the knowledge and assistance with the Record Ridge fieldwork.

A thank you to all my colleagues in the Environmental Economic Geology Laboratory, especially Dr. Nina Zeyen, Baolin Wang, Colton Vessey and Avni Patel, for their comradery and tutelage, in and out of the lab. I would like to thank the other numerous groups and organizations through university that led me to this point, namely: The Kappa Sigma Fraternity - Epsilon Alpha Chapter, the Helium Boyz, The Commune, The Golden Bears Varsity Wrestling Team and Coach

Owen Dawkins, the Nor'westers Athletic Association, U of A Event Staff, ATLAS, P.S. Warren, Garage Gym and the Mahsi Fellowship. Finally, thanks to my father and mother, Jamie and Hiromi, my brother Keisuke, my grandfather Toyoaki (Ojii), my cat Kabocha and the rest of my family and friends for the unconditional support, insight and inspiration. Blessed does not begin to define the life I have been given.

TABLE OF CONTENTS

LIST OF TABLES

LIST OF FIGURES

LIST OF ABBREVIATIONS

μXRF – Micro X-ray Fluorescence

χ^2 – Goodness of fit (chi-squared)

ANSTO – Australian Nuclear Science and Technology Organization

apfu – Atoms Per Formula Unit

ASCI – Australian Synchrotron Compute Interface

BSE – Backscattered Electron

CSA – Carbon-Sulfur Analysis

DW – Durbin Watson

EDS – Energy Dispersive X-ray Spectroscopy

EEGL – Environmental Economic Geology Lab

EPMA – Electron Probe Micro-Analysis

HPAL – High Pressure Acid Leaching

KB – Kirkpatrick-Baez

LOD – Limit of Detection

LOI_V – Loss On Ignition

ICP-MS – Inductively Coupled Plasma Mass Spectrometry

ICP-OES – Inductively Coupled Plasma Optical Emission Spectrometry

MLA – Mineral Liberation Analysis

n – number of points taken for the sample

N – number of sample set averages used for calculation.

NIR – Near Infrared

NSERC – Natural Sciences and Engineering Research Council of Canada

PONKCS – Partial Or No Known Crystal Structure

QEMSCAN – Quantitative Evaluation of Minerals by Scanning Electron Microscopy

QXRD – Quantitative X-ray Diffraction

R^2 – Coefficient of Determination

RGB – Red Green Blue

RRUFF – Not an acronym, named after the cat owned by the project's main backer.

R_{wp} – Weighted Profile R-Factor

SEM – Scanning Electron Microscopy

TDI – Time Dependent Intensity

TSF – Tailings Storage Facility

UV – Ultraviolet

VP-FESEM – Variable Pressure Field Emission Scanning Electron Microscope

WDS – Wavelength Dispersive Spectrometry

WD-XRF – Wavelength Dispersive X-ray Fluorescence

WHY – West High Yield

wt% – Weight Percent

XFM – X-ray Fluorescence Microscopy

XRD – X-ray Diffraction

XRF – X-ray Fluorescence

ZM – Calibrated mass value for the unit cell of each phase

CHAPTER 1: INTRODUCTION

Nickel and cobalt are critical metals. Critical metals are essential in the production of renewable and responsible energies (e.g., batteries, wind turbines), they are used in medicine, agriculture and information technology, but they are also finite and depleting in supply (Government of Canada, 2021). In order to secure these resources and meet growing demand, ore cutoff grades are lowering, companies are digging deeper into the Earth and alternative sources are being explored. One such alternative source is the reprocessing of mine tailings.

Mine tailings are the "uneconomic" fraction of processed ore. They are disposed of in subaqueous or subaerial storage facilities with roughly 8–14 billion tonnes of this waste produced annually (Lutandula and Maloba, 2013; Kandji et al., 2017; Alcalde et al., 2018; Parbhakar-Fox et al., 2018; Baker et al., 2020). While many tailings management strategies have been developed, such as incorporation into construction projects, revegetation and burial, reprocessing for desirable resources is growing in popularity (Meyer, 1980; West High Yield Resources, 2013; Power et al., 2014). For the mining industry to adopt any new practice, such as the reprocessing of mine tailings, it must remain cost-effective for owners while providing acceptable returns to shareholders (Power et al., 2014). Tailings from ultramafic deposits have been of particular interest as they commonly host economic first row critical transition metals (e.g., nickel, cobalt) and also weather to produce carbonate minerals which can sequester atmospheric carbon for tens of thousands of years (Lackner, 2003; Wilson et al., 2006; Wilson et al., 2009a; Hamilton et al., 2018). The reprocessing of ultramafic mine tailings could serve as a powerful economic motivator for mines to embrace more sustainable procedures for ore processing and tailings management.

Little is known regarding the mineralogical and elemental associations of critical metals in tailings, from an economic geology perspective, and how these characteristics change over time as tailings weather. Understanding the distribution and abundances of critical metals in mineral phases within tailings is a necessary step in evaluating whether resource recovery is economic and what techniques should be used for reprocessing. In addition, the methodological approach to grading ore and tailings, and assessing elemental abundance has typically been limited to a whole-rock analysis using either inductively coupled plasma – mass spectrometry (ICP-MS) or X-ray fluorescence (XRF) (e.g., Keays and Jowitt, 2013; Britten, 2017; Parbhakar-Fox et al., 2018;

Ostadrahimi et al., 2020). Developing an accurate analytical tool to determine both mineralogical abundances and stoichiometry within tailings would aid in our assessment of economic viability and may be applied generally to the ore grading process.

1.1. Research Objectives

The objectives of this thesis are as follows:

1) Characterize the identities and deportment of transition metals within weathered, ultramafic mine tailings from Tasmania, Australia, and within samples from a weathered, ultramafic deposit in British Columbia, Canada.

2) Examine transition metal behavior, quantify element partitioning amongst gangue and ore minerals within these samples and assess whether the transition metals are present at an economically viable abundance for recovery.

3) Develop an analytical tool for calculating whole rock elemental abundances by integrating quantitative X-ray diffraction and electron probe micro-analysis data and then compare the results to an industry whole rock analysis to validate and justify the methodology.

4) Evaluate whether the overall results justify further analysis, and suggest potential recovery methods for critical metals.

1.2. Thesis Organization

This thesis consists of two research papers (Chapters 2 and 3), plus a general introduction (Chapter 1) and summary (Chapter 4). The first research paper (Chapter 2) qualitatively analyzes and compares serpentinized ultramafic mine tailings from the Lord Brassey mine, Tasmania and weathered serpentinite from Record Ridge, British Columbia. Chapter 3 quantitatively analyzes only the Lord Brassey samples and focuses on developing an analytical tool to calculate whole rock elemental abundances from the integration of QXRD and EPMA data.

CHAPTER 2: INVESTIGATING ALTERATION STYLES AND TRANSITION METAL SINKS AT THE LORD BRASSEY MINE, TASMANIA AND RECORD RIDGE DEPOSIT, BRITISH COLUMBIA

2.1. Abstract

As global population increases and nations seek to achieve carbon neutrality, so too does the demand for metals that are critical for the production and storage of cleaner energy in a more sustainable future. Ultramafic ore deposits contain a diverse array of such metals, including nickel and cobalt, but their partitioning behavior between ore, accessory and alteration minerals is imprecisely known. Here we describe the deportment of nickel and other critical metals in samples from a pre-mining (Record Ridge deposit, British Columbia, Canada) and a post-mining (Lord Brassey mine, Tasmania, Australia) environment. Scanning electron microscopy (SEM) with energy dispersive X-ray spectroscopy (EDS) revealed the greatest variety of transition metals to be hosted in sulfides, which were coarse-grained in Lord Brassey and micrometer-sized at Record Ridge. Mineral identification using powder X-ray diffraction (XRD) and Raman spectroscopy revealed that magnetite and chromite are abundant and common hosts to transition metals at both localities; however, ferrihydrite becomes an increasingly important host to these elements in weathered mineral wastes (Lord Brassey) and outcropping ore (Record Ridge). Synchrotron X-ray fluorescence microscopy (XFM) was used to describe the spatial distribution of nickel and other transition metals within sulfide minerals. XFM results showed cobalt on the margins of Ni-bearing sulfide grains in relatively unweathered samples, and the preferential uptake of nickel by low-temperature carbonate minerals and cobalt by iron oxyhydroxides in weathered samples. These results demonstrate that multiple minerals host critical metals in ultramafic rocks and that which minerals should be considered “ore minerals” changes as a result of weathering. Over time, chemical weathering and alteration of ultramafic ore deposits and tailings will break down the numerous minerals that host critical transition metals and concentrate them into a few distinct mineral phases. Understanding and being able to identify the final sinks of these metals improves the capacity for recovery and overall yield during ore processing and future remediation. Therefore, targeted recovery for particular metals in these styles of deposits is achievable and should be explored further in a quantitative manner and at the deposit scale.

2.2. Introduction

In order to build a cleaner, more sustainable and more digitized economy while the global population increases, a number of metals dubbed "critical metals" are needed (e.g., Government of Canada, 2021; Liu et al., 2021). Critical metals are aptly named due to their significance in the production and storage of renewable and environmentally responsible energy, playing a major role in the products from many important fields (e.g., medicine, agriculture), and also due to their finite and rapidly depleting supply (Liu et al., 2021; Australian Government, 2022). Examples of such metals include nickel and cobalt, which are used in electronics and batteries (Bacon et al., 2002; Sovacool, 2019; Government of Canada, 2021).

Mineral resources are finite, and exploration is shifting to search deeper underground and further into more isolated localities while mines reduce their ore cutoff grades to meet demand (Lutandula and Maloba, 2013). One solution to the growing issue of where to find critical metals is the reprocessing of mine tailings, of which the mining industry produces roughly 8–14 billion tonnes annually (Lutandula and Maloba, 2013; Parbhakar-Fox et al., 2018; Baker et al., 2020). Tailings are the "uneconomic" byproducts of the ore processing circuit, deemed as such by their low resource content. Having been milled and separated from the valuable material, tailings are typically disposed of in subaerial or subaqueous storage facilities, where they may pose immediate geoenvironmental or health risks such as acid mine drainage or aerosol and dust ejection (e.g., Adiansyah et al., 2015; Parbhakar-Fox et al., 2018; Stankovic et al., 2018; Park et al., 2019). As it can be costly to manage tailings, historically these wastes were sometimes abandoned for long periods of time, which can add to the chance of geoenvironmental problems occurring (Adiansyah et al., 2015; Schoenberger, 2016; Figueiredo et al., 2019b). Nowadays, many forms of tailings management are practiced, such as: incorporating tailings into structural and construction projects, remediation through revegetation or burial, prolonged storage and monitoring in the aforementioned tailings storage facilities (TSF), or reprocessing (e.g., Meyer, 1980; West High Yield Resources, 2013; Power et al., 2014; Slack et al., 2017; Stefaniak and Wróżyńska, 2017; Figueiredo et al., 2019a).

The efficiency of critical metal extraction is far from perfect, with some world-class mines such as the Mount Keith nickel mine of Western Australia reporting nickel recoveries around only 70% with the remaining 30% remitted to "waste" (Grguric et al., 2006). These waste piles can

contain extremely high metal contents that rival world-class deposits and are already under the ownership of mines, making them accessible sources of economic metals ripe for recovery. Having previously borne the stigma of being unusable and dangerous, the idea of tailings being reprocessed for valuable metals has gained increased traction to not only meet the growing demand for mineral resources, but adhere to sustainable mining practices, stricter environmental regulations and a greener societal outlook. Reprocessing tailings offers the benefits of reducing exploration costs and eliminating the capital expenditure of building new mines, while reducing waste output and environmental impacts as well as prolonging the life of mines and providing jobs and stability for mining communities (Lutandula and Maloba, 2013; Parbhakar-Fox et al., 2018; Figueiredo et al., 2019a; Figueiredo et al., 2019b). While mine tailings hosting a diversity of resources are now being appraised for their valuable resources (e.g. copper porphyry deposits), the interest in ultramafic mine tailings in particular has crescendoed due to their multi-faceted uses as a source of critical metals, a building material and a sink for atmospheric carbon dioxide (CO_2) (e.g., Rampacek, 1982; Wilson et al., 2006; Kandji et al., 2017; Alcalde et al., 2018; Power et al., 2021).

Ultramafic deposits can host economic concentrations of nickel (>0.6% nickel is considered low grade and economic) and cobalt (>0.01% cobalt is considered low grade and economic) which are both critical metals needed for a greener future (EMEW Clean Technologies, 2017; Slack et al., 2017; Hamilton et al., 2018; Government of Canada, 2021). The first-row transition metals (e.g., Fe, Co, Ni) are mostly found in the crystal structures of minerals such as olivine due to the similarity of their charge and ionic radii with magnesium (e.g., Hamilton et al., 2016; Britten, 2017). Hydrothermal alteration (serpentinization) [which shrinks the magnesium sites as the olivine (<Mg–O> = 2.114 Å, Hazen, 1976) converts to serpentine (<Mg–O> = 2.067 Å, Mellini, 1982)] or melt formation under variable O_2 and S_2 fugacities may mobilize some of these transition metals to concentrate into accessory minerals such as sulfides, oxides and alloys (e.g., Sciortino et al., 2015; Britten, 2017; Hamilton et al., 2018; Escuder-Viruete et al., 2019). Oxidation of sulfide minerals during weathering and atmospheric exposure mobilizes transition metals in both pre-mining deposits and post-mining tailings (e.g., Lindsay et al., 2015; Hamilton et al., 2016; Kandji et al., 2017). Decomposition of serpentine and brucite during reaction with the resulting sulfuric acid, and with carbonic acid in rainwater, results in the formation of alteration minerals such as carbonates and oxyhydroxides, which sequester the transition metals via

substitution into magnesium sites or by adsorption onto mineral surfaces (e.g. Hamilton et al., 2016; Kandji et al., 2017). Weathering affects tailings to a greater extent because of their increased surface area that results from milling during metal extraction (Wilson et al., 2006). Alteration minerals act as the final sink for such metals, unless they themselves are broken down via another process (i.e., acid dissolution) (Hamilton et al., 2016). Oxide minerals and alloys are more resistant to weathering, so these accessory minerals should be relatively unaltered in post-mining settings when compared to pre-mining ones (Britten, 2017; Hamilton et al., 2018). Carbonate minerals are of particular interest because of their ability to sequester atmospheric carbon and retain it for over tens of thousands of years, which may aid in reducing global atmospheric CO_2, another motivating factor to adopt tailings reprocessing (Lackner, 2003; Wilson et al., 2006; Wilson et al., 2009a; Wilson et al., 2014).

Transition metals are sequestered during the weathering of serpentinite and formation of carbonate and iron oxyhydroxide minerals, but it is not clear whether particular metals are preferentially taken up by either mineral type (Hamilton et al., 2016; Hamilton et al,. 2018; Hamilton et al., 2020). The extent to which Co and Ni are preferentially partitioned into different alteration minerals may influence their recovery; thus it is important to know which minerals should be considered ore minerals and how this changes over the course of the mining life cycle. This study examines samples from both a post-mining and pre-mining scenario: ultramafic mine tailings from the derelict Lord Brassey mine, Tasmania and a weathered serpentinite deposit from the anticipated mine at the Record Ridge project, Canada. Samples were obtained from both sites and analyzed using powder X-ray diffraction (XRD), scanning electron microscopy (SEM) with energy dispersive X-ray spectroscopy (EDS), Raman spectroscopy and synchrotron X-ray fluorescence microscopy (XFM) to assess how the deportment of iron, nickel, cobalt and other transition metals are affected by weathering. The aim of this study is to investigate transition metal partitioning and behavior from two climatically-similar localities to provide context regarding their final mineral sinks and potential recovery.

2.3. Sampling and Analytical Methods

2.3.1. Field Localities

The derelict Lord Brassey mine is located in western Tasmania, Australia within the Heazlewood district, roughly 240 km northwest of Hobart (Anderson et al., 2002) (Fig. 2.1A). Heazlewoodite (Ni_3S_2) was mined via a single adit in 1896 and again in the 1950s, but no work has since taken place due to the relatively inaccessible location and rough terrain (Anderson et al., 2002). Summer in the Lord Brassey area averages a high of 20 °C, winter averages a high of 9 °C and yearly precipitation averages 1954 mm (Australian Government, 2021). The relative humidity ranges from 62% to 92% year round, and coupled with the numerous rough and heavily vegetated hills and swift rivers, makes for an unfavorable setting that remains sparsely populated to this day (Anderson et al., 2002; Australian Government, 2021) (Fig. 2.1B). The Lord Brassey mine site is situated in the Heazlewood River Mafic-Ultramafic complex, which is composed of Cambrian-age serpentinized ultramafics with an ophiolitic origin (Alpine-type ultramafic complex) (Anderson et al., 2002; West High Yield Resources, 2013). The Brassey Hill Harzburgite Sequence within the district, which hosts the Lord Brassey mine, is noted to contain harzburgite and dunite (Peck and Keys, 1990). The area is praised and pilfered by collectors for its abundance of nickel carbonates, such as zaratite [nominally $Ni_3CO_3(OH)_4•4H_2O$] and hellyerite ($NiCO_3•6H_2O$) and nickel sulfide minerals, primarily heazlewoodite, (Anderson et al., 2002).

The Record Ridge deposit is a late–stage magnesium exploration project located in British Columbia, Canada, 7.5 km southwest of the town of Rossland and 400 km east of Vancouver (West High Yield Resources, 2013) (Fig. 2.1C). The mineral rights are owned by West High Yield (WHY) Resources who began exploration in 2007 with mapping, surveying and drilling campaigns, and who intend to develop the site into a mine for magnesium. Summer temperatures average a high of 22 °C, winters average a high of –2 °C and yearly precipitation averages 900 mm (West High Yield Resources, 2013). The humidity ranges from an average of 44% in the summer to an average of 82% in the winter and the site is centered in the more developed and hospitable coniferous forests of the Rocky Mountains (West High Yield Resources, 2013; Climate-Data, 2021) (Fig. 2.1D). The Record Ridge site is situated primarily on the Record Ridge ultramafic body which is composed of Paleozoic serpentinized and carbonated ultramafics and has an area of roughly 7.5 km^2 (West High Yield Resources, 2013). The body is a result of magmatic

emplacement of mafic-ultramafic intrusives (Alaskan-type ultramafic complex) and contains significant dunite and wehrlite (Himmelberg and Loney, 1995). The widespread, dominantly serpentinized ultramafic zones host economic concentrations of magnesium (West High Yield Resources, 2013).

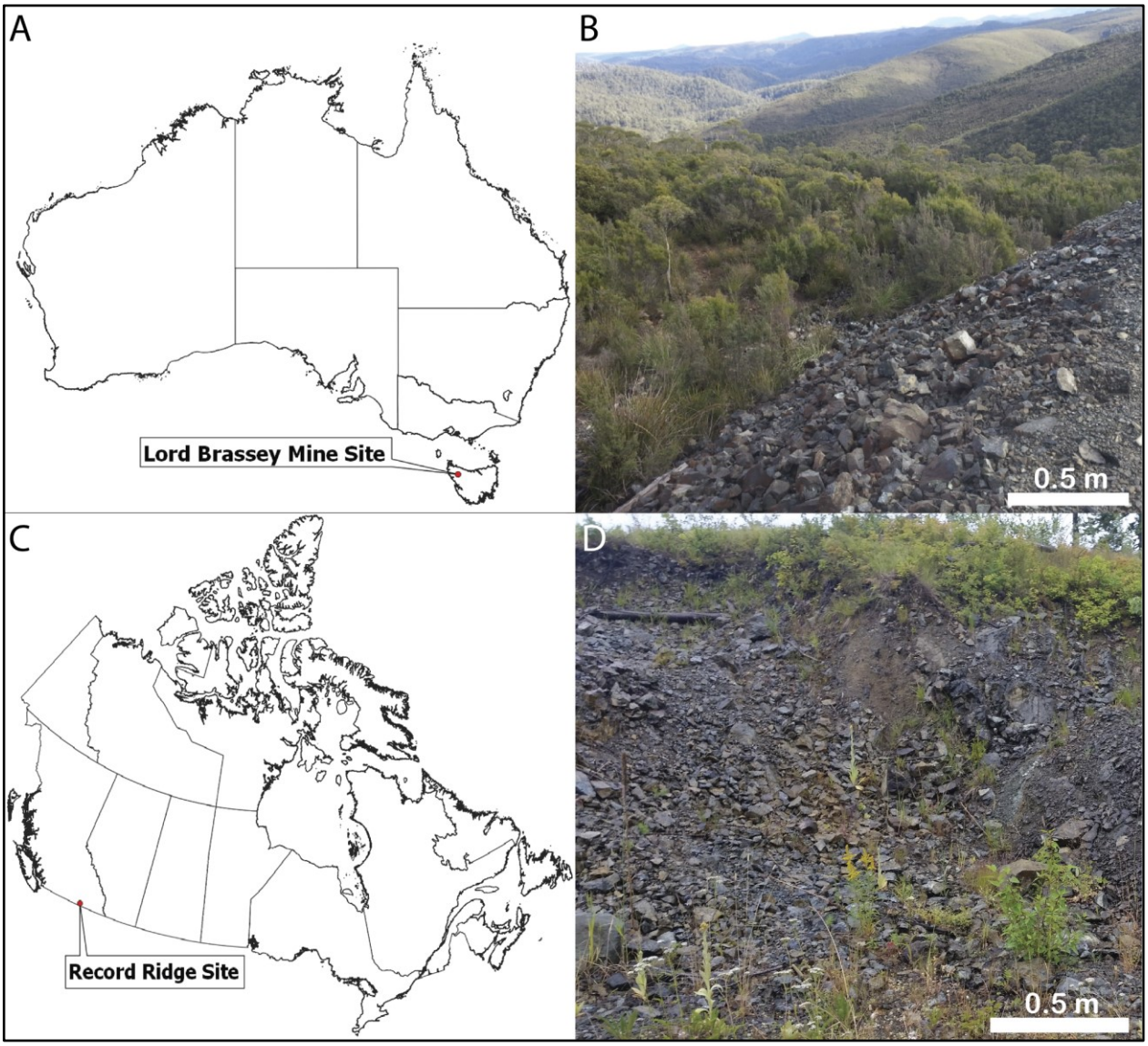

Fig. 2.1. A) The Lord Brassey mine site location within Australia. B) Lord Brassey tailings pile. C) The proposed Record Ridge mine site location within Canada. D) An exposed outcrop from the Record Ridge site.

2.3.2. Sample Acquisition

The Lord Brassey samples were collected in July 2014 and over fifty geological samples were collected from two tailings piles (Mililli, 2014). Of these samples, twenty-seven rock samples were used in this research. The Record Ridge deposit was visited in August, 2020. Twenty-one rock samples were collected from outcrops at two separate field sites. For both sites, the analyzed samples were selected with a focus on weathered crusts, alteration minerals, accessory minerals and representativeness of the deposit geology.

2.3.3. Powder X-ray Diffraction (XRD)

Samples were powdered and micronized prior to analysis. The samples were first crushed with a sledgehammer on a steel plate and then pulverized for seven minutes each in a Spex shatterbox using a tungsten-carbide dish with a ring and puck. Record Ridge samples that showed a layered weathering rind were separated into two subsamples to study differences between the weathered rind and fresh interior. Afterwards, 5 mL aliquots of the powders were micronized for seven minutes each with a McCrone micronizing mill using agate grinding elements and anhydrous ethanol. Micronized samples were dried at room temperature and disaggregated using an agate mortar and pestle.

Mineral identification was done using XRD patterns obtained from two different X-ray diffractometers. The Lord Brassey samples were analyzed using the Rigaku Ultima IV diffractometer in the Department of Earth & Atmospheric Sciences XRD Lab, University of Alberta, whereas the Record Ridge samples were analyzed using a Bruker D8 Advance diffractometer in the Environmental Economic Geology Lab (EEGL), University of Alberta. The Rigaku Ultima IV has a D/Tex Ultra detector and a Co X-ray tube that was operated at 38 kV and 38 mA. The Bruker D8 Advance has a LYNXEYE XE-T detector and a Co X-ray tube that was operated at 35 kV and 40 mA. All XRD patterns were collected over a 2θ range of 3–80° using a step size of 0.02° 2θ and a dwell time of 1 second/step.

Mineral phases were identified from the resulting XRD patterns with reference to the ICDD PDF 4+ database using the program DIFFRAC.EVA (Bruker AXS). For samples that were determined to contain smectites, a calcium exchange was performed to stabilize the position of the 001 peak to a *d*-value of ~15 Å. The calcium exchange procedure of Mervine et al. (2018) was

used for this purpose, which involves mixing the micronized sample with 150 mL of 1 M $CaCl_2$•$2H_2O$ in 18.2 MΩ•cm deionized water overnight using a shaker table and filtering multiple times with deionized water. These samples were then dried at room temperature and reanalyzed. Phase identification from XRD results was also informed by scanning electron microscope observations to justify the inclusion of trace phases.

2.3.4. Scanning Electron Microscopy (SEM) and Energy Dispersive X-ray Spectroscopy (EDS)

Nine thin sections of Lord Brassey samples were prepared at the Thin Section Laboratory of the University of Alberta, whereas ten thin sections of Record Ridge rock samples were prepared by Vancouver Petrographics Ltd. SEM was performed in the Department of Earth & Atmospheric Sciences at the University of Alberta using a Zeiss Sigma 300 Variable Pressure Field Emission Scanning Electron Microscope (VP-FESEM). The SEM has a 30 μm aperture which provided a beam current of 315 pA, and uses a field emission gun with a tungsten filament. This instrument is equipped with dual silicon drift detectors (Bruker), each with a resolution of 123 eV and an area of 60 mm^2. Imaging was performed with a backscattered electron (BSE) detector in variable pressure mode at roughly 50 Pa. The accelerating voltage was set at 25 kV and no conductive coating was applied to the samples.

2.3.5. Raman Spectroscopy

Raman spectroscopy was undertaken using the Horiba LabRam HR Evolution Raman microscope in the Fluids & Ore Deposits Lab at the University of Alberta, equipped with green, near-infrared (NIR) and ultra-violet (UV) lasers, covering a spectral range of 200–2200 nm. A number of thin sections were examined as were powdered samples of weathered crusts that were collected using a Dremel drill. Raman spectra were collected using the green laser with a wavelength of 532 nm at 100% power, a grating of 1800 grooves/mm, a hole size of 50 nm and exposure time of 3 seconds for 3 accumulations.

2.3.6. X-ray Fluorescence Microscopy (XFM)

X-ray fluorescence microscopy mapping was carried out on the XFM beamline at the Australian Synchrotron, Australian Nuclear Science and Technology Organization (ANSTO). The

Kirkpatrick-Baez (KB) microprobe (with a spot size range of 1–10 μm) and Maia detector (fluorescence detector with short dwell times of 0.5–5 ms) were used to collect elemental abundance data, which were processed using GeoPIXE via the Australian Synchrotron Compute Interface (ASCI). The beam energy was set to 10 keV and the beam diameter was focused to approximately a 2 μm spot size (via KB mirrors). For the scans of the entire thin sections (known as overviews), there was a step size of 15 μm with a dwell time per pixel of 1.250 ms. There is a notable spectral overlap of the Co Kα and Fe Kβ peaks, as well as the Co Kβ and Ni Kα peaks in the X-ray fluorescence spectra collected on the XFM beamline. Therefore, the data for the distribution of cobalt are not always as reliable as the data for the other transition metals (due to the creation of an artefact making it appear cobalt is present when it may not be); as such, cobalt maps are only reported where the other analytical methods support its presence.

2.4. Results

2.4.1. Hand Sample Observations

The Lord Brassey samples were divided into two distinct categories, "orange" or "green" based on the color of external weathering products and/or matrix minerals (Fig. 2.2A, B). The "green" samples contain minerals having different shades of green, within both their fresher interiors and at weathered surfaces. They are also characterized by veins of white minerals found throughout their interiors and visible at fresh surfaces. A number of "green" samples also displayed an "apple-green" mineral on weathered surfaces, which was identified as the nickel carbonate mineral, zaratite, based on an HCl acid test and Raman spectroscopy (covered in section 2.4.2) (Fig. 2.2B). The "orange" samples contain black matrices and are coated with two different types of orange weathering products: bright-orange minerals in small concentrations and rust-colored rinds that extend across large portions of the exposed crust. A small number of the "orange" samples were observed to have larger blue veins running through them. When sawn to reveal fresh surfaces, a number of these samples, regardless of category contained coarse-grained sulfides, and most contained observable oxides.

The Record Ridge samples are more homogenous in appearance compared to the diversity of the Lord Brassey samples. All samples taken from the Record Ridge area are of the same general appearance but with varying degrees of weathering (Fig. 2.2C, D). They possess a black/gray

matrix with a rind of weathered, white material of varying thickness, and in some circumstances an orange rust-colored rind of varying thickness is present at the surface of the white, weathered rock (noted as “sandwich”) (Fig. 2.2D). When sawn open to reveal fresh surfaces, some samples show visible oxides but there are no visible sulfides present.

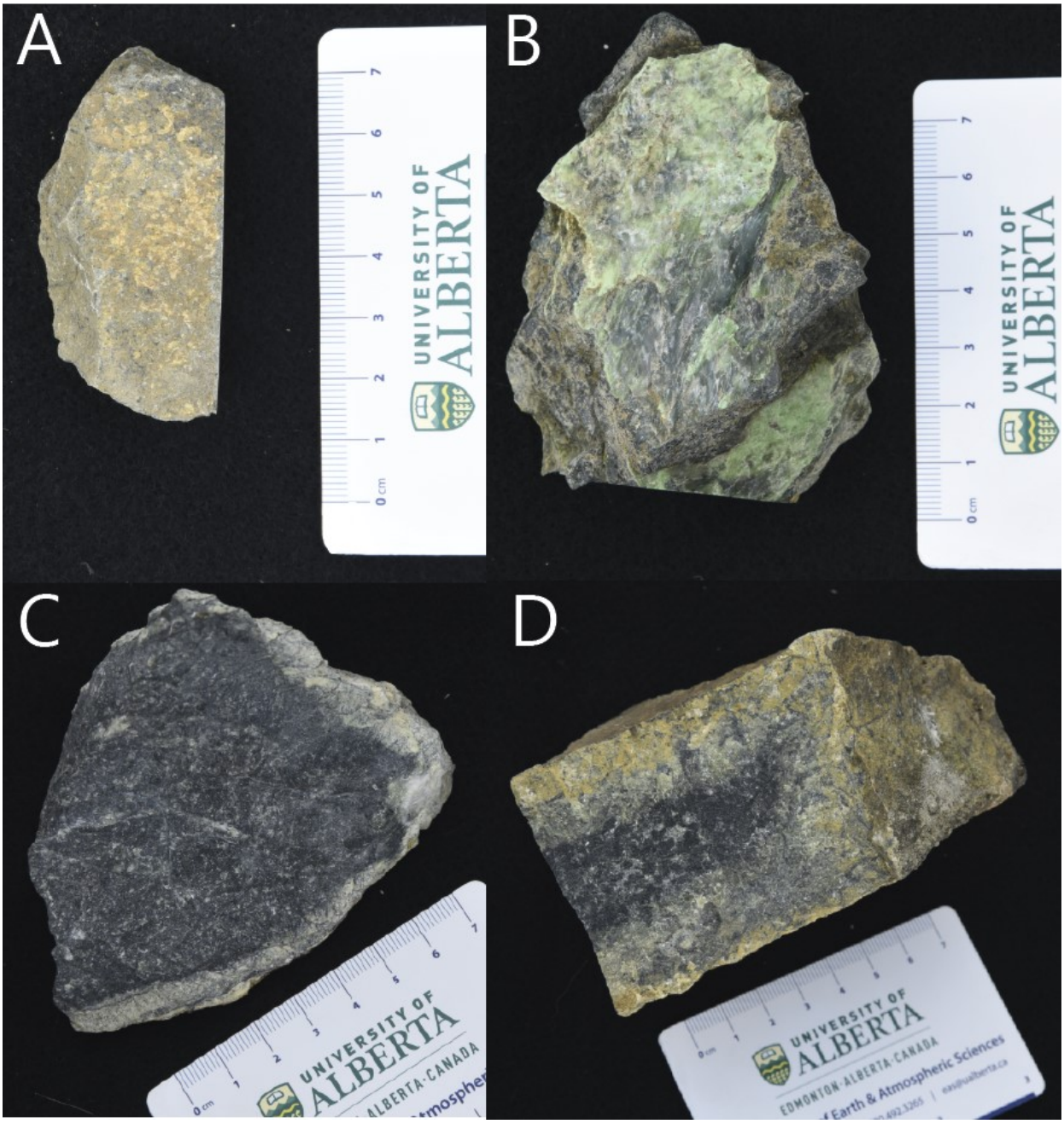

Fig. 2.2. Examples of Lord Brassey samples coated with (A) “orange” and (B) “green” alteration minerals. Examples of (C) lightly weathered and (D) heavily weathered Record Ridge samples.

2.4.2. Qualitative Mineralogical Results

The bulk mineralogy of the Lord Brassey samples is similar, regardless of the color of surficial alteration minerals (covered in the following chapter in more detail as Table. 3.1). Samples are dominated by serpentine minerals, being mainly lizardite [$Mg_3Si_2O_5(OH)_4$] with minor amounts of its polymorph, antigorite. All samples also contain minor amounts of garnets {pre-dominantly andradite [$Ca_3Fe_2(SiO_4)_3$]} and clinochlore [$(Mg,Fe^{2+})_5Al(Si_3Al)O_{10}(OH)_8$] (Fig. 2.3A). Minor to trace amounts of the spinels chromite ($FeCr_2O_4$) and/or magnetite (Fe_3O_4) were present in all samples analyzed and some samples were found to have sulfides (heazlewoodite) and detectable awaruite (Ni_3Fe) (Fig. 2.3B). There were no carbonate minerals or iron oxyhydroxides detectable from XRD patterns. However, zaratite is generally considered to be an amorphous phase and iron oxyhydroxides are typically amorphous or nanocrystalline. As such, it is not unexpected that these phases could not be detected using XRD.

The bulk mineralogy of the Record Ridge samples (Table A.1) is dominated by a serpentine matrix (mainly lizardite and antigorite), with some samples containing small amounts of forsterite-rich olivine (Mg_2SiO_4) (Fig. 2.3C, D). All samples contain spinels in the form of magnetite with some also containing chromite, but there are no observable sulfide minerals (Fig. 2.3C). Almost all the samples contain minor amounts of chlorite (clinochlore), actinolite [$Ca_2(Mg,Fe)_5Si_8O_{22}(OH)_2$], magnesite ($MgCO_3$), calcite ($CaCO_3$), and brucite [$Mg(OH)_2$] (Fig. 2.3C, D). A few samples contain trace amounts of the low-temperature magnesium carbonate minerals, hydromagnesite [$Mg_5(CO_3)_4(OH)_2{\bullet}4H_2O$] and pyroaurite [$Mg6Fe2(CO_3)(OH)_{16}{\bullet}4H_2O$] (Fig. 2.3D). Subsamples of weathered rind and fresh rock from individual Record Ridge samples produced similar XRD patterns with some mineralogical differences (Fig. 2.3D).

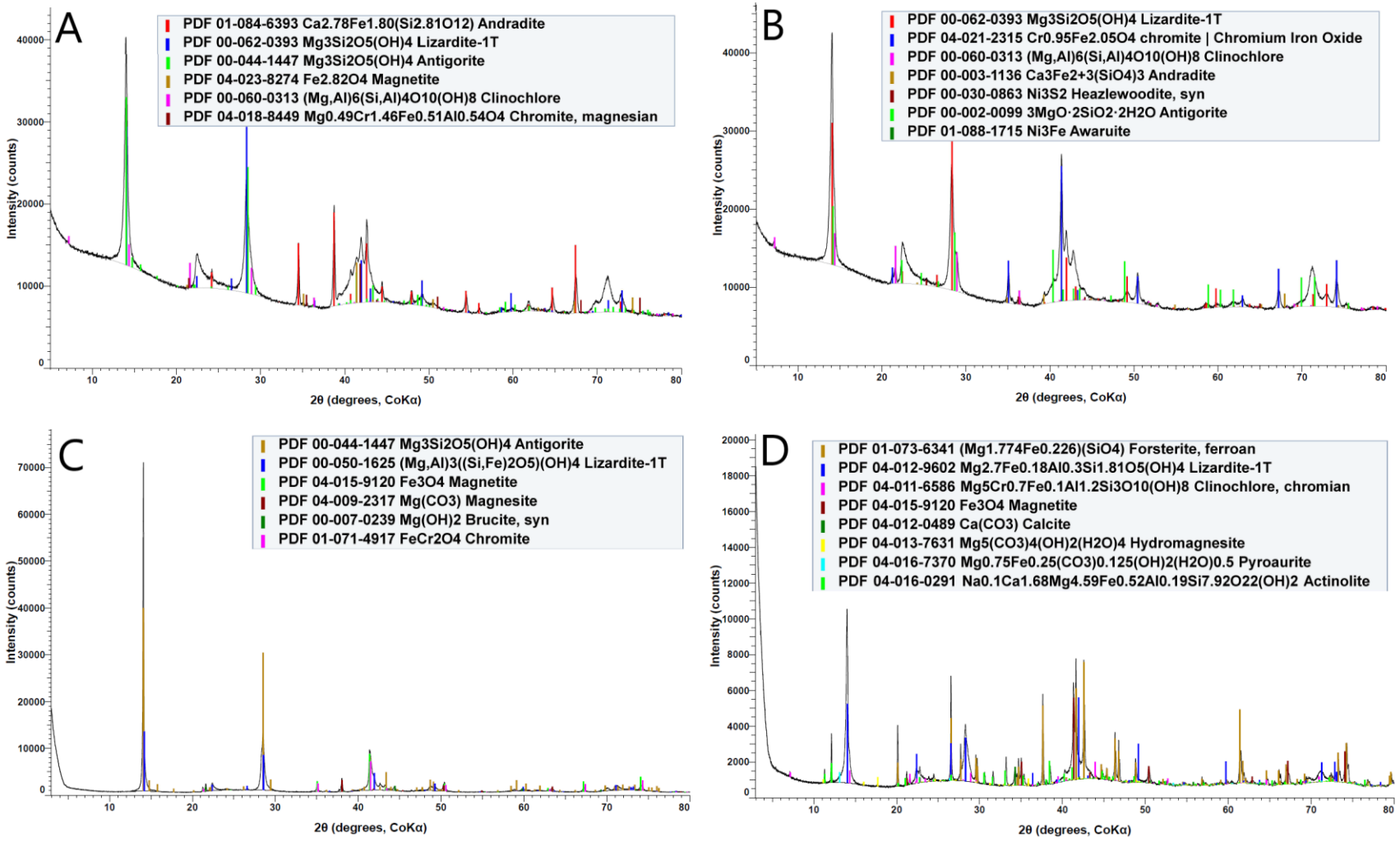

Fig. 2.3. Representative XRD patterns for (A) Lord Brassey "green" sample 14LBM1-10, (B) Lord Brassey "orange" sample 14LBM1-31, (C) lightly weathered Record Ridge sample 20RRP1-1 and (D) heavily weathered Record Ridge sample 20RRP1-12A.

Closer analysis of the Lord Brassey samples using SEM revealed that most of the accessory minerals are associated with weathered serpentine. Zones of chlorite, indicated by elevated aluminum content relative to serpentine minerals, are common in the sample matrix, as are zones of andradite-rich garnet. No carbonate minerals were observed with SEM, but there was visible iron oxyhydroxide in a weathering rind (Fig. 2.4A). Oxide minerals were spread throughout the samples and most common forms of these were single grains of chromite with magnetite overgrowths and nearby magnetite veins that were sometimes spatially associated with isolated grains (Fig. 2.4B). Coarse-grained sulfide zones, some measuring millimeters across, were also associated with weathered serpentine (Fig. 2.4C). Upon closer inspection, EDS showed that these zones contained various sulfide minerals each dominated by a different transition metal, such as Ni, Co, Cu and Cd, which were confirmed via electron probe micro-analysis (EPMA) to be: heazlewoodite, cobaltpentlandite (Co_9S_8), anilite (Cu_7S_4) and hawleyite/greenockite (CdS) respectively (Fig. 2.4D). Cobaltpentlandite was found on the outskirts of the sulfide zones and the hawleyite/greenockite is typically associated with heazlewoodite. Awaruite was observed sparsely as 1–10 μm grains, or associated with heazlewoodite within sulfide zones (Fig. 2.4E).

Record Ridge samples have a matrix of serpentine minerals with some relict forsterite, and the weathered portions possess higher concentrations of accessory minerals, akin to the Lord Brassey samples. No iron oxyhydroxide or carbonate minerals (beyond bedrock magnesite which contained no critical transition metals) were observed in the thin sections. Spinels are found throughout the samples as chromite grains with magnetite overgrowths (like at Lord Brassey) that are sometimes cross cut by calcite veins, and as veins consisting of numerous magnetite grains (Fig. 2.4F). Sulfides are present in the samples but there are no coarse-grained sulfide zones as in the Lord Brassey samples. Sulfide minerals occurred at low abundance with grains ranging from 1–100 μm in diameter, typically disseminated within the matrix with magnetite veins running through them. Regarding the variety of these sulfides, based on the EDS results, they appear to consist mainly of unknown nickel sulfide, as well as rare, unknown copper sulfide (due to the lack of EPMA data) (Fig. 2.4G). There were no alloy minerals found within the samples, however an unknown nickel arsenide mineral was identified with EDS and is typically associated with the nickel sulfides (Fig. 2.4H).

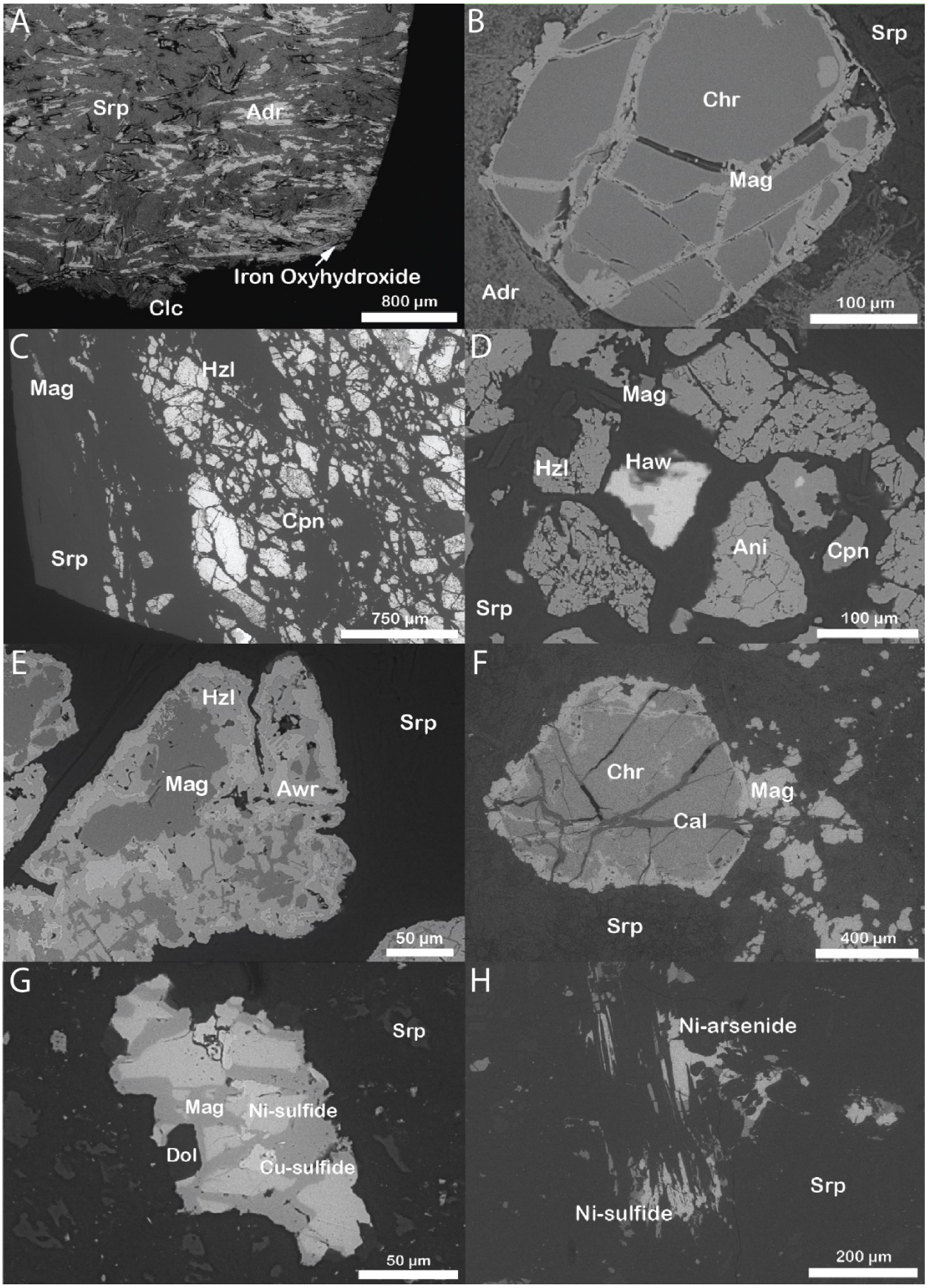
A
Srp
Adr
Iron Oxyhydroxide
Clc
800 µm
B
Srp
Chr
Mag
Adr
100 µm
C
Mag
Hzl
Cpn
Srp
750 µm
D
Mag
Hzl
Haw
Ani
Cpn
Srp
100 µm
E
Hzl
Srp
Mag
Awr
50 µm
F
Chr
Mag
Cal
Srp
400 µm
G
Srp
Mag
Ni-sulfide
Dol
Cu-sulfide
50 µm
H
Ni-arsenide
Srp
Ni-sulfide
200 µm

Fig. 2.4. BSE images for Lord Brassey (A–E) and Record Ridge (F–H) samples. A) Iron oxyhydroxide in a weathered rind, B) chromite grain with magnetite overgrowths, C) sulfide zone, D) variable mineralogy in a sulfide zone, E) awaruite intergrown with sulfides as an overgrowth of magnetite, F) chromite grain with magnetite overgrowth and calcite veins, G) sulfide grain and H) nickel arsenide associated with nickel sulfide.

Five samples for Lord Brassey and Record Ridge were examined using Raman spectroscopy to better characterize the weathering products. Owing to the challenges with sample fluorescence, a coherent Raman spectrum was only produced for the orange crust of 14LBM1-3 from a thin section (Fig. 2.5A) and the "apple-green" mineral in the crust from the 14LBM1-28 hand sample (Fig. 2.5B). The orange mineral was identified as ferrihydrite (nominally $5Fe_2O_3 \bullet 9H_2O$) based on the diagnostic peaks at 361, 508 and 707 cm^{-1} (Das and Hendry, 2011). The "apple-green" mineral was determined to be zaratite based on the diagnostic peaks at 458, 982, 1073 and 1609 cm^{-1}, the hydroxyl stretch peak at ~3600 cm^{-1}, and the amorphous nature of the spectrum (intensity falls below 100 counts) (Frost et al., 2008; Garcia-Guinea et al., 2013). Data were collected for what appeared to be carbonate minerals within thin sections and isolated powder, which were all determined to be andradite through comparison with Raman spectra in the RRUFF database (Lafuente et al. 2016). The powdered sample and the points on the hand samples failed to produce any comprehensible spectra. For Record Ridge, the Raman spectra produced from weathered rinds were also very poor and disregarded, but were similar in appearance to the Lord Brassey rejected spectra.

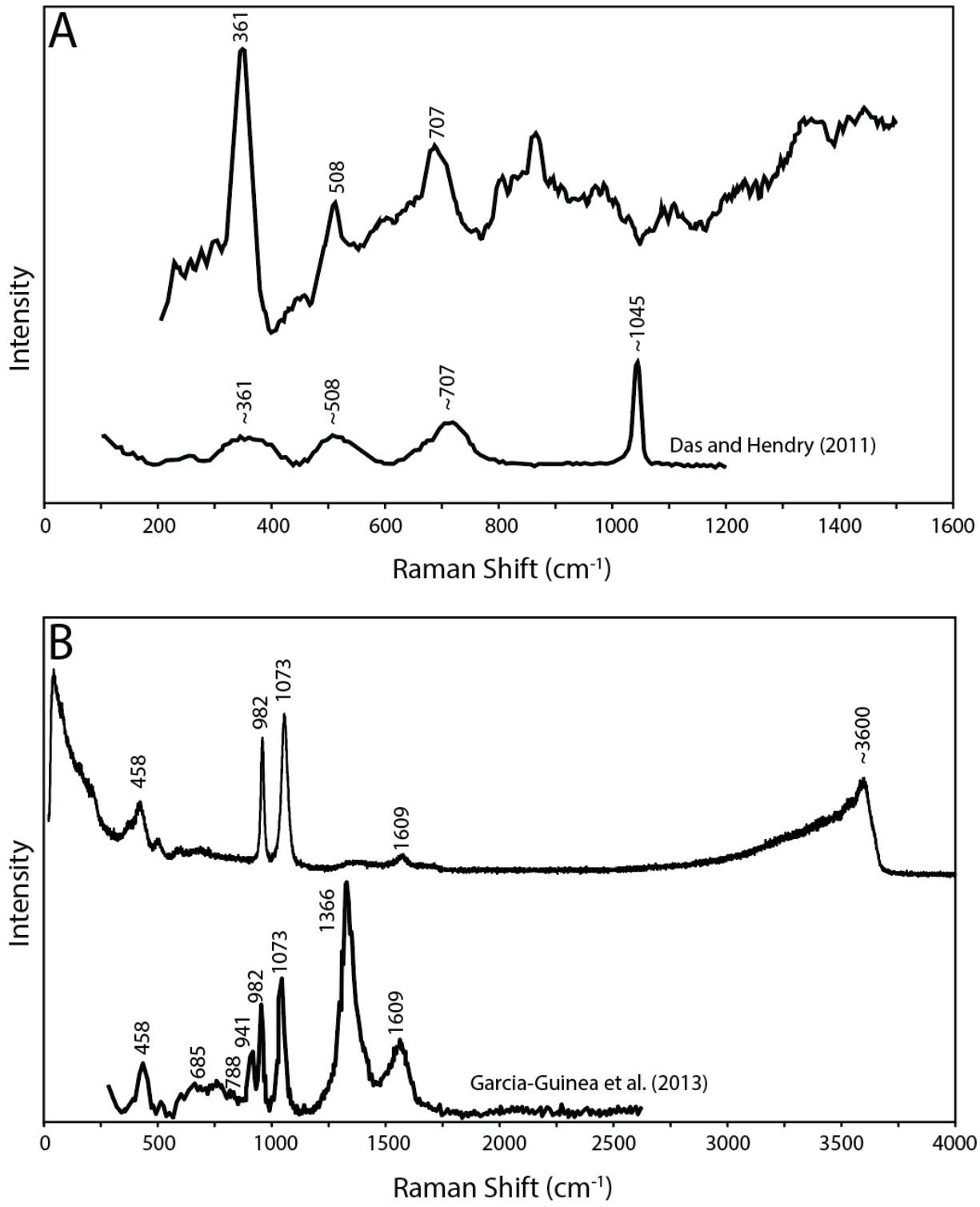

Fig. 2.5. Raman spectra from Lord Brassey samples. A) Ferrihydrite spectrum from the weathered rind of sample 14LBM1-3 (top) compared to ferrihydrite spectrum from Das and Hendry, 2011

(bottom). B) Zaratite spectrum from the crust of sample 14LBM1-28 (top) compared to zaratite spectrum from Garcia-Guinea et al. 2013 (bottom).

The XFM maps permitted interpretation of the distribution and partitioning of transition metals within ore, gangue and alteration minerals from the two localities. Figure 2.6 depicts a tricolor map for Lord Brassey sample 14LBM1-28, showing the locations of iron (red), nickel (blue) and cobalt (green) in accessory minerals, as well as intensity maps for their weight percentages (wt%). Nickel is hosted primarily within the sulfide zones in high concentrations and is effectively absent in the other accessory minerals (Fig. 2.6A, B). Iron is found within the grains of garnets and oxide minerals but is only present as veins that crosscut the sulfides rather than in the sulfides themselves (Fig. 2.6A, C). Cobalt was shown to be isolated in grains (which were confirmed to be cobaltpentlandite via EPMA) on the margins of these coarse-grained sulfides, which is supported by the SEM results, and contain a lower concentration overall (Fig. 2.4C, D, 2.6A, D). For the weathered areas of the Lord Brassey sample, a color map was also acquired with nickel (blue) and cobalt (green), but calcium (red) was used in place of iron to distinguish between the garnets and iron oxyhydroxides such as ferrihydrite (Fig. 2.7A). Calcium, like iron, is present in the many garnet grains spread throughout the weathered area but is absent in the iron oxyhydroxides of the weathering rind. Nickel concentration increases in the serpentine matrix as the degree of alteration increases but is absent in the iron oxyhydroxide, whereas XFM data indicate cobalt is associated with iron oxyhydroxides of the weathering rind, which is supplemented by EDS data showing higher cobalt concentrations in these minerals, though this may be an artefact (Fig. 2.7A). Figure 2.7B depicts an area within the weathered Lord Brassey sample that was used to identify element associations for iron, cobalt and nickel. There are elemental association plots that show the direct relationship between cobalt and iron (most likely as an artefact) (Fig. 2.7C), the inverse relationship between nickel and iron (Fig. 2.7D) and the lack of relationship between cobalt and nickel (Fig. 2.7E) within heavily weathered areas of the Lord Brassey samples.

The Record Ridge samples possess similar distributions of transition metals with the exception that this deposit lacks the coarse-grained sulfide zones present in the Lord Brassey samples. As a result of the lack of coarse-grained minerals beyond the commonplace chromite/magnetite, only a tricolor map of a weathered area for the Record Ridge samples is

presented (Fig. 2.8A), displaying chromium (red), nickel (blue) and cobalt (green). Chromium is present solely in chromite grains whereas cobalt distribution is similar to the Lord Brassey samples, mainly being found in all areas containing iron (most likely as an artefact), but of a lower concentration (Fig. 2.8A). Nickel abundance was shown to increase in areas where serpentine has experienced greater weathering, but an intensity map uncovered the presence of nickel-bearing, micrometer-scale grains spread throughout the matrix, in contrast to the Lord Brassey samples (Fig. 2.8A, B). The elemental association maps taken from the area shown in Fig. 2.8B, indicate two relationships are present for the elements. There are two direct relationships between cobalt and iron (Fig. 2.8C), one for the spinels (larger, steep vertical spike) and one for the micrometer-scale grains (smaller, shallow horizontal spike). Isolating the points for each peak of this elemental association plot further demonstrates the trends in iron–cobalt associations apply to two different mineral phases: spinels for the steep vertical peak (Fig. 2.9A, B) and sulfide/alloy minerals for the shallow horizontal peak (Fig. 2.9C, D). The elemental association graphs for nickel and iron (Fig. 2.8D) and cobalt and nickel (Fig. 2.8E) possess weaker non-linear relationships for the matrix (larger spike along the vertical axis for Fig. 2.8D and small spike along the horizontal axis for Fig 2.8E) and a direct relationship for the elements within micrometer-scale grains (smaller diagonal spike for Fig 2.8D and larger diagonal spike for Fig 2.8E). Additionally, the plots for Record Ridge also indicate a higher concentration of iron, nickel and cobalt in the samples (with nickel and cobalt measured at an order of magnitude greater), compared to those of Lord Brassey (Figs. 2.7C–E, 2.8C–E). As well, the concentration of nickel exceeds that of cobalt in the Record Ridge samples (with a resultingly stronger association between nickel and iron), whereas in the Lord Brassey samples the nickel and cobalt concentrations are on par (Figs. 2.7D, E, 2.8D, E).

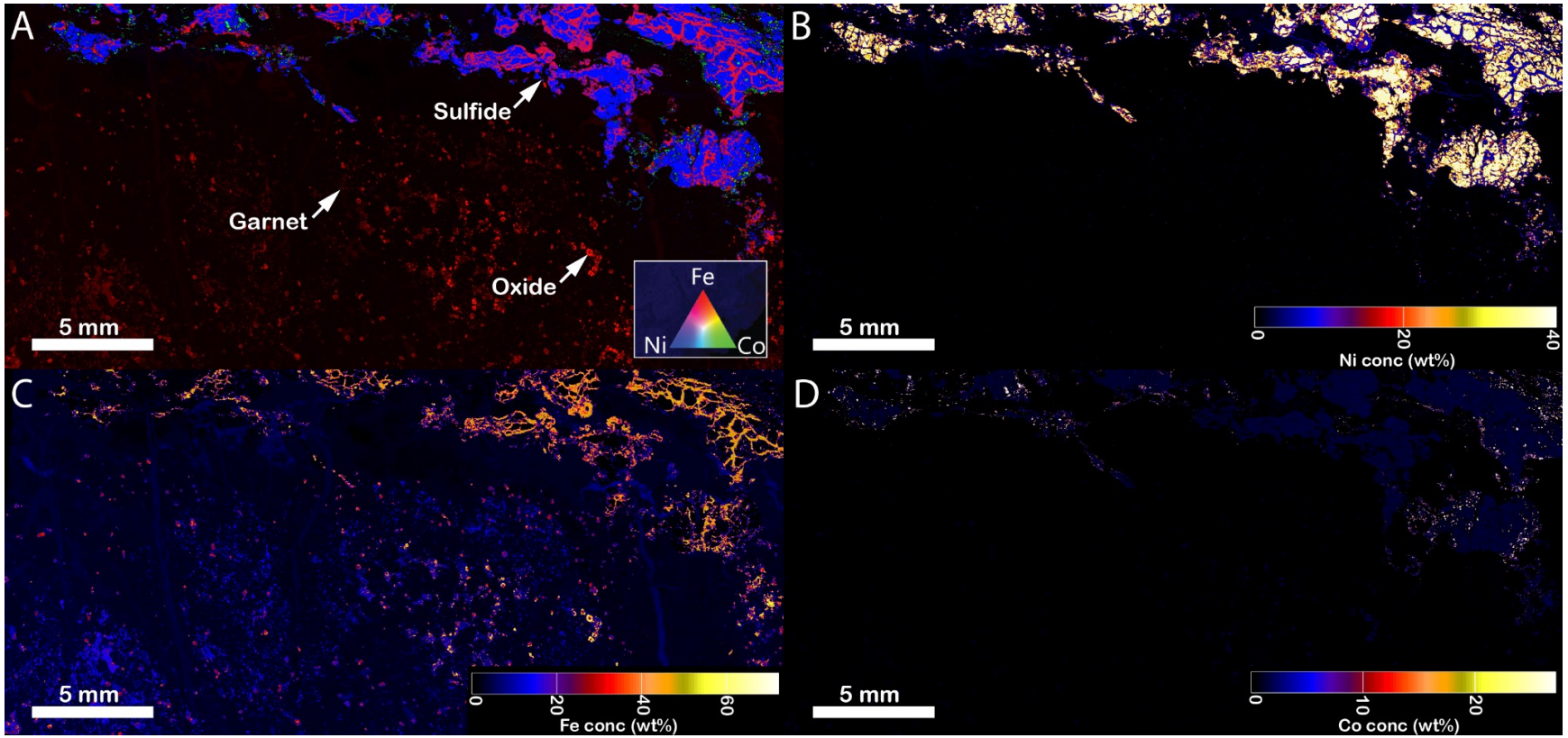

Fig. 2.6. Full thin section XFM scans of a sulfide zone within Lord Brassey sample 14LBM1-28. (A) RGB map of Fe (red), Co (green) and Ni (blue). Intensity maps of (B) nickel, (C) iron and (D) cobalt.

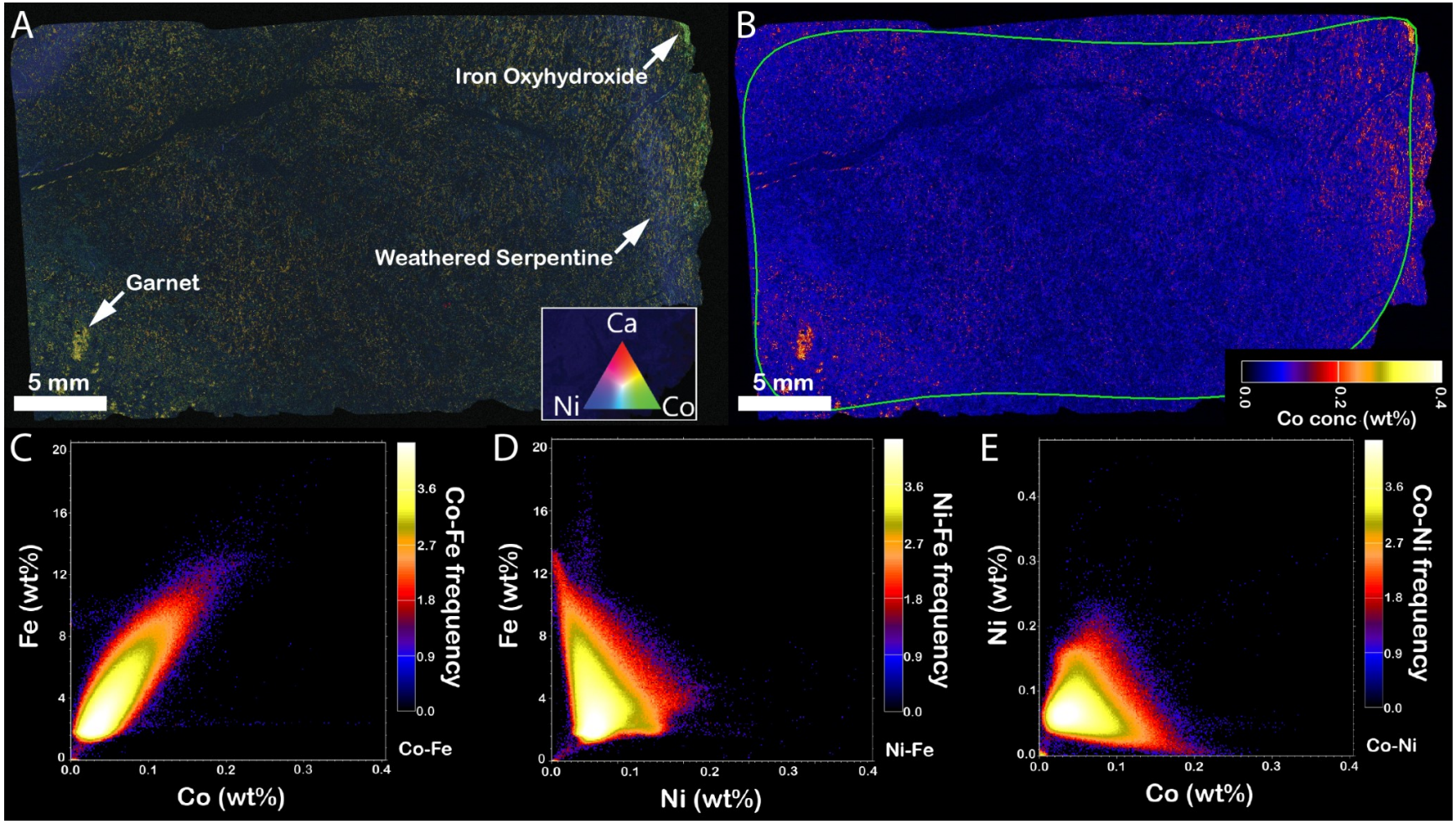

Fig. 2.7. Full thin section XFM scans of a weathered area from Lord Brassey sample 14LBM1-3. (A) RGB map of Ca (red), Co (green) and Ni (blue). (B) Intensity map of cobalt to show area of analysis for the element association plots for (C) Co-Fe, (D) Ni-Fe and (E) Co-Ni.

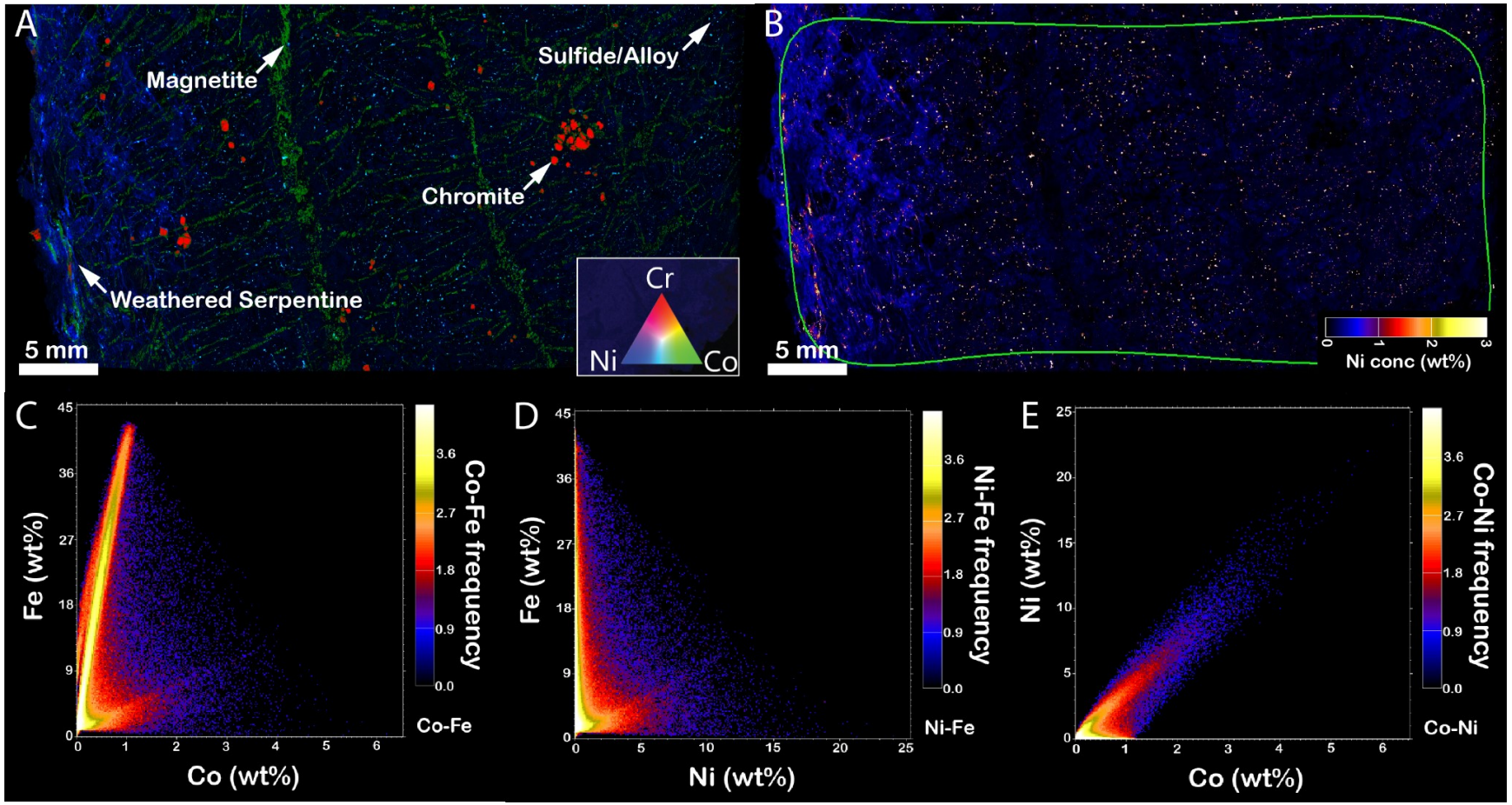

Fig. 2.8. Full thin section XFM scans of a weathered area from Record Ridge sample 20RRP1-1. (A) RGB map of Cr (red), Co (green) and Ni (blue). (B) Intensity map of nickel to show area of analysis for the element association plots for (C) Co-Fe, (D) Ni-Fe and (E) Co-Ni.

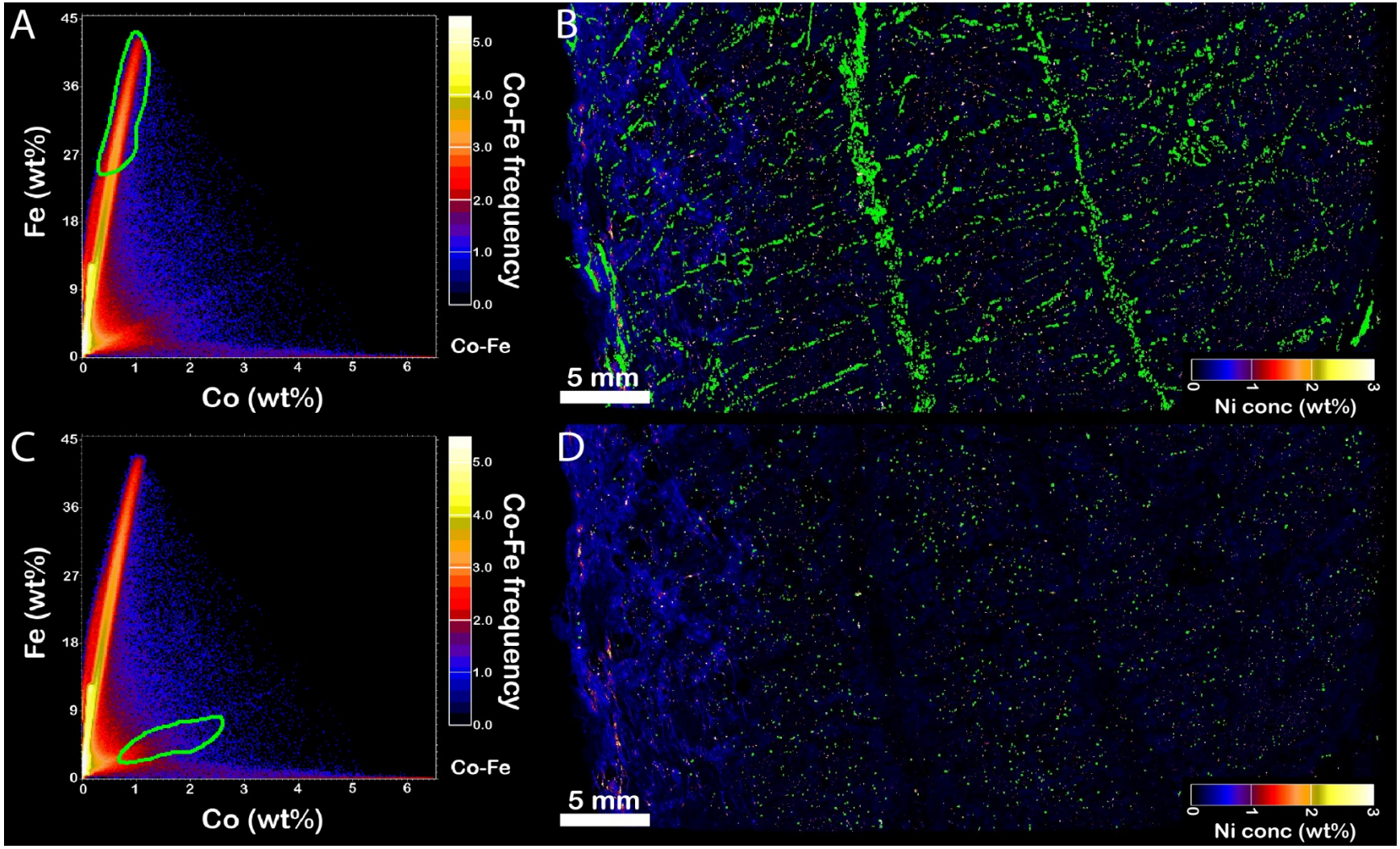

Fig. 2.9. Full thin section XFM scan of Record Ridge sample 20RRP1-1. (A) Co-Fe elemental association plot with spline over the larger, steep vertical spike with (B) the areas corresponding to those points highlighted in green. (C) The same elemental association plot with spline over the smaller, shallow horizontal spike with (D) the areas corresponding to those points highlighted in green.

2.5. Discussion

Despite the Lord Brassey and Record Ridge sites being different types of mineral deposits, Alpine and Alaskan ultramafic complexes respectively, both localities contain similar mineral assemblages: serpentines, spinels, nickel sulfides and Ni-Fe alloy (among other minerals) (Dick, 1974; Filippidis, 1985). Meteoric alteration has taken place at both localities as noted by the presence of weathering rinds and alteration minerals. The Lord Brassey tailings have weathered over the last 118 years between deposition and sampling, while the Record Ridge deposit has been exposed to the atmosphere since at least the last glaciation, over 20,000 years ago, but lacking the increased surface area of mine wastes. In addition to the pre-existing accessory minerals that resulted from serpentinization and host dissolution, weathering produces new sinks for transition metals at both deposits.

2.5.1. Accessory Minerals

The nickel-rich Lord Brassey area is known for its wide array of sulfide minerals (Anderson et al., 2002) and this is where the greatest assortment of transition metals (i.e., Fe, Ni, Co, Cd, Cu) were observed within coarse-grained sulfide zones (Figs. 2.4C, D, 2.6). Although compositionally similar sulfides were noted in the Record Ridge samples, no coarse-grained sulfide zones were found. Instead, Ni-sulfides appeared as 1–100 μm isolated grains (Fig. 2.4G), that are ubiquitous throughout the matrix (Fig. 2.8). SEM results confirm the relationship observed in XFM elemental-association graphs (i.e., the positive correlation of nickel with cobalt, and both of these with iron); coupled with EDS data revealing high iron content in the place of sulfur in some portions of these grains, these grains can be deduced to be a mixture of sulfides and alloys (Fig. 2.8). Iron-cobalt elemental association plots for Record Ridge samples show two populations of potentially cobalt-bearing minerals (Fig. 2.9). The strongest trend, which has the greatest slope, corresponds to the Fe-rich, Co-poor spinels (Fig. 2.9A, B) whereas the weaker trend, with a smaller slope, applies to the smaller grains, which are also nickel-bearing (Fig. 2.9C, D). Nickel- and cobalt-bearing alloys, such as awaruite and wairuite (CoFe), are common in ultramafic complexes (with the Lord Brassey area being no exception) and are commonly associated with sulfides (Fig. 2.4E) (e.g., Bird & Weathers, 1979; Anderson et al., 2002). Nickel arsenides/arsenates (Fig. 2.4H), such as oregonite (Ni_2FeAs_2) or annabergite [$Ni_3(AsO_4)_2 \bullet 8H_2O$], provide another source of this

metal and they have previously been reported from Lord Brassey and other ultramafic deposits (Dick, 1974; Bird and Weathers, 1979; Anderson et al., 2002; Mindat, 2022).

Oxide minerals (i.e., spinels) were present in samples from both Lord Brassey and Record Ridge, at greater abundance and with a relatively uniform composition and grain size, compared to the sulfide minerals. Magnetite, a common product of serpentinization, was present in both sets of samples as veins and associated with chromite grains. The chromite compositions are similar in both deposits (Fig. 2.4B, F). The oxide minerals are relatively devoid of nickel (roughly 0.10 wt% on average as confirmed using EPMA) instead containing iron and chromium, and the XFM maps suggest that cobalt is present in all cases where iron is observed (Figs. 2.7, 2.8). Cobalt substitutes for iron during the formation of iron-bearing minerals (e.g., Liao et al., 1991), but it rarely exceeds 1.0 wt% in the oxides and weathered areas of our samples (Figs. 2.6, 2.7, 2.8). Due to the aforementioned spectral overlap of iron and cobalt when using XFM, false detection of cobalt in oxide minerals is likely the artefact of this technique. Therefore, the most important source of cobalt during weathering of these samples, as confirmed using EPMA, is the sulfides (Fig. 2.6).

2.5.2. Serpentine Weathering and Alteration Minerals

A number of alteration minerals observed in the samples resulted from oxidation of sulfides and carbonation of serpentine and accessory minerals. The matrix serpentine contains large amounts of magnesium and lesser amounts of iron, some of which was mobilized during weathering. The XFM maps reveal that the nickel content associated with the matrix serpentine increases with the degree of weathering (proximity to the weathered rind which is deduced by the change in color in the XFM maps) (Figs. 2.7, 2.8). In areas where sulfide and alloy minerals are less common, nickel partitions into serpentine, where it remains inaccessible to recovery until the host is broken down via chemical weathering (Sciortino et al., 2015). The nickel and cobalt content of the serpentine is quite low and maxes out at roughly 1.0% and 0.1% concentration respectively, whereas the nickel and cobalt content in sulfides peaks at roughly 40% and 20% concentration respectively (Figs. 2.6, 2.7, 2.8). Sulfide minerals are thus the major source of nickel and cobalt observed in the oxyhydroxide and carbonate alteration minerals. Sulfide minerals contained identical transition metals to what were observed in the carbonates (nickel) and iron oxyhydroxides (cobalt at Lord Brassey, nickel at Record Ridge), and were absent from any weathered sample

surface, having undergone oxidation and dissolution from atmospheric exposure and reaction with carbonate-rich groundwater (as previously observed in serpentinites by Anderson et al., 2002; Hamilton et al., 2016; Kandji et al., 2017). Conversely, oxide minerals are noted to be more stable and resistant to weathering and they retain the hosted transition metals over the mining life cycle (Britten, 2017; Hamilton et al., 2018). This is consistent with our observations which show that magnetite and chromite grains in weathered tailings (Fig. 2.4B) appear nearly identical in habit and composition to those in an unprocessed deposit (Fig. 2.4F), with no obvious chemical or physical alteration. The alloy grains in Record Ridge samples were too small to make any detailed textural observations, but it is assumed that they will resist weathering through the mining phase (Britten, 2017; Kandji et al., 2017; Hamilton et al., 2018; Hamilton et al., 2020).

Samples from both Lord Brassey and Record Ridge had carbonate coatings on their surfaces, which are common products from the weathering of ultramafic rocks and tailings (e.g., Wilson et al., 2006; Wilson et al., 2009a). The nickel carbonate mineral zaratite is present on the exposed surfaces of some Lord Brassey samples, which has likely formed as a dehydration and decarbonation product of hellyerite (Anderson et al., 2002). Zaratite was not observed in any of the powder XRD results but is notoriously hard to detect via XRD due to its lack of long-range crystalline order. Hydrated magnesium carbonate minerals have previously been reported from Lord Brassey and were observed for Record Ridge using XRD as part of this study. The magnesite observed in the Record Ridge samples formed via metasomatism and did not contain any critical transition metals, which contrasts with the nickel-rich zaratite and hydrated Mg-carbonate minerals that form by weathering at Lord Brassey and other ultramafic-hosted mines. There was an expectation for the Lord Brassey samples to contain plentiful carbonates, but these were unexpectedly absent from many samples and a number of factors may play into this. The Lord Brassey mine site is a valued location for fossickers and it is renowned as the type locality for several rare and visually attractive carbonate minerals. Previous sampling has likely biased preservation of the strongest signals of nickel mobility.

Iron oxyhydroxides are another common weathering product of ultramafic rocks, and can act as sinks for remobilized transition metals. Iron oxyhydroxides were observed on the surfaces of many Lord Brassey samples, but very few from Record Ridge (Figs. 2.4A, 2.7). Raman spectroscopy was used to identify ferrihydrite, which is a common weathering product of

ultramafic rocks (Figs. 2.4A, 2.5A) (e.g., Hamilton et al., 2020). The ferrihydrite from Lord Brassey contained no nickel, but did contain possible cobalt via XFM and SEM-EDS, which we can attribute to the preferential substitution of cobalt for iron or adsorption of cobalt to the surface of ferrihydrite (Fig. 2.7). At Record Ridge, nickel was concentrated on the weathered crusts of the samples, which is likely made up in part by ferrihydrite (Fig. 2.8A). Which elements are associated with iron oxyhydroxide is dependent on the neutralization potential of the rock, which is largely controlled by the absence or presence of the strongly basic mineral, brucite. Silica-rich serpentinites (like those at Lord Brassey) do not usually contain brucite as it is destroyed to form other minerals when surrounding silicate-rich rocks are incorporated into serpentinization (Berg, 1989; Anderson et al., 2002). Ni binds to ferrihydrite in an environment with a pH of roughly 6–8 and in lower pH environments will instead leach out (Bigham and Nordstrom, 2000). The Lord Brassey samples contain little to no brucite and would have a pH lower than this range, so the nickel did not bind to ferrihydrite and cobalt was captured instead. Whereas the Record Ridge samples, where the serpentinite is more brucite-bearing, have a pH within this range, so the nickel is captured and associated with ferrihydrite. Which elements are concentrated in weathering-derived carbonate minerals will also depend on pH gradients during weathering. At Lord Brassey, nickel is leached from ferrihydrite in weathered cobbles to form nickel carbonate minerals, such as zaratite at grain surfaces. Contrastingly, all of the first row transition metals are associated with an assemblage of hydromagnesite, pyroaurite and ferrihydrite in the brucite-bearing serpentinite tailings at the Woodsreef mine, Australia (Hamilton et al., 2018), which will likely be the fate of transition metals at the mineralogically similar Record Ridge deposit.

2.5.3. Implications

Ultramafic deposits commonly possess high concentrations of critical transition metals, and the Lord Brassey and Record Ridge sites both contain significant concentrations of these metals, particularity nickel and cobalt. Nickel is hosted in the greatest concentration within sulfides and will end up in carbonates (on the exposed surfaces of samples) if these minerals are broken down (which is likely due to atmospheric exposure) as well as associated with iron oxyhydroxide minerals in brucite-bearing rocks. Cobalt is potentially hosted in iron-bearing minerals, and will preferentially be hosted in iron oxyhydroxide in less basic, more silica-rich rocks such as Lord Brassey. Based on these results, carbonate minerals and iron oxyhydroxides should be considered

ore minerals in a post–mining setting. The exceptions to this are carbonate minerals that have formed from metasomatism, such as magnesite, which was determined to contain no critical transition metals. The oxide minerals (spinels) are virtually unaltered following mining, and alloy minerals, such as awaruite are noted to pass through chemical ore processing circuits (e.g., froth flotation) into tailings (Britten, 2017; Kandji et al., 2017). These weathering-resistant minerals are easily recovered with magnetic or gravimetric separation (Britten, 2017; Hamilton et al., 2018). One benefit of recovering nickel and cobalt from carbonate and iron oxyhydroxide weathering products is that they concentrate critical metals not only from sulfide dissolution but also from dissolution of serpentine and brucite. Allowing tailings to weather via oxidation of sulfides to produce sulfuric acid, and reaction with carbonic acid in rainwater, makes accessible the otherwise unrecoverable resources in silicate and hydroxide minerals. Weathering reactions also serve to liberate oxide and alloy minerals (Kandji et al., 2017; Hamilton et al., 2020). Passive weathering is a slow process. Therefore, pretreatments could be made prior to reprocessing tailings for critical metal recovery, such as the use of acid heap leaching, oxidation to force the dissolution of sulfides, or CO_2 injection to accelerate mineral dissolution and formation of carbonate minerals (Power et al., 2014). The quandary for the induced formation of carbonate minerals is that these minerals must be processed for the valuable metals they sequester, which results in the rerelease of CO_2 back into the atmosphere. While there is potential for the recycling of materials for future carbonate mineral formation and CO_2 sequestration, there will be a net increase of CO_2 emissions should the carbonate minerals be processed for critical metal recovery.

The Lord Brassey samples are already waste rock and tailings so the assessment for metal recovery can begin immediately, whereas the Record Ridge deposit has yet to be mined. Due to the high sulfide mineral content in the Lord Brassey mine tailings, and those minerals being the primary source of critical transition metals, it would be wise to process these tailings as sulfide ore via froth flotation (the pinnacle of sulfide ore processing) prior to the aforementioned tailings management treatment (Fuerstenau et al., 2007; Lindsay et al., 2015; Alcalde et al., 2018; MacKay et al., 2020). The sulfide ore of Lord Brassey, which is heavily weathered and covered with iron oxyhydroxides, still contains critical transition metals and could be subject to processing methods such as high pressure acid leaching (HPAL) akin to nickel laterite deposits (e.g., Chang et al., 2016; Siebecker et al., 2018). While the tailings at Lord Brassey hold valuable metals, the likelihood of reprocessing is slim, as the working was quite small and recovery would not be cost

effective at this time. However, larger scale projects with similar geology would benefit from utilizing this information and implementing tailings management and reprocessing. A prime candidate would be the neighboring Avebury nickel deposit, which is co-genetic to the Heazlewood River ultramafic complex, is reported to contain 0.26 Mt of nickel and has resumed operations which would offset the startup (Keays and Jowitt, 2013). The proposed ore processing circuit for Record Ridge relies heavily on acid dissolution and grinding, which will greatly accelerate weathering and the formation of alteration minerals, although the intention is to recover the magnesium resource as carbonates with no plans for any additional metal recovery from the tailings afterwards (West High Yield Resources, 2013). However, these tailings management processes are applicable for other brucite-bearing serpentinites with high concentrations of nickel sulfide minerals and alloys akin to Record Ridge, such as the Dumont Sill, Quebec (Sciortino et al., 2015), the Baptiste deposit, British Columbia (Britten, 2017) and Woodsreef Mine, Australia (Hamilton et al., 2018).

Tailings from Lord Brassey contain 0.095–0.718 wt% nickel with an average of 0.229 wt%, and their cobalt content ranges from 0.008–0.015 wt% with an average of 0.011 wt% (Table. A.2). For Record Ridge, the nickel content ranges from 0.002–0.243 wt% with an average of 0.188 wt%, and the cobalt content ranges from 0.003–0.013 wt% with an average of 0.010 wt% (Table. A.3). Rocks from both localities qualify as low-grade cobalt ore and there are Lord Brassey samples that would be considered low-grade nickel ore (EMEW Clean Technologies, 2017; Slack et al., 2017). This characterization labels these deposits as economic sources of these critical transition metals by today's standards; however, a more detailed, quantitative analysis is required to assess the economic feasibility of metal recovery from current and future tailings resources.

2.6. Conclusions

The qualitative analysis of samples collected from the Lord Brassey mine, Tasmania, and the Record Ridge deposit, Canada, revealed a number of sources and sinks for valuable transition metals during weathering. Coarse-grained sulfide minerals contain the largest concentration and diversity of transition metals, even after 118 years of weathering at Lord Brassey. Oxide minerals resist weathering and may host cobalt due to the association of cobalt and iron, but to a much lesser extent than the sulfides. Alloys host nickel and cobalt while resisting weathering, making them a

desirable target for recovery. Weathering-derived carbonate minerals are the preferential sink for nickel in brucite-poor and brucite-rich ultramafic rocks. Iron oxyhydroxides are the preferred sink for cobalt in brucite-poor ultramafic rocks whereas they concentrate nickel and other transition metals in brucite-bearing rocks. Both carbonate and iron oxyhydroxide alteration minerals will act as the final sink for such metals in tailings. Bedrock carbonate minerals (e.g., magnesite from metasomatism) are unlikely to contain critical transition metals and should not be considered for processing and recovery when pursuing these metals. Recovery of oxides and alloys may be improved owing to their enhanced liberation during weathering. Our results show that which ore minerals host critical metals changes over the life of a mine, giving rise to opportunities for resource recovery from mine tailings and even opening up the possibility of using tailings storage facilities as part of the ore processing circuit. The next step is to develop quantitative geometallurgical tools to determine the economic viability of metal recovery at different stages of the mining cycle.

2.7. Acknowledgments

Funding was provided by the Natural Sciences and Engineering Research Council of Canada (NSERC) Discovery Grants program, the Natural Resources Canada Clean Growth Program and the Canada Research Chairs Program to Dr. Sasha Wilson. Part of this research was undertaken on the XFM beamline at the Australian Synchrotron, part of ANSTO (proposals M15033, M15925 and M17212). Thank you to Frank Marasco, Tom Jones and Daralyn Fox of WHY Resources for the knowledge and assistance with the Record Ridge fieldwork. Thanks to Mark Labbe and Walter Harley at the U of A thin section lab and Vancouver Petrographics for thin section preparation. Thank you to Rebecca Funk for performing XRD analysis on my samples and thanks to Dr. Nathan Gerein and Guibin Ma for their extreme patience and guidance with the SEM. Thanks to Dr. Matthew Steele-MacInnis, Spencer Poulette and Marko Szmihelsky for their assistance with the Raman spectroscopy.

CHAPTER 3: QUANTITATIVE ANALYSIS OF TRANSITION METAL DISTRIBUTION AND RECOVERABILITY FROM SERPENTINITE SKARN TAILINGS FROM LORD BRASSEY MINE, TASMANIA

3.1. Abstract

There is a growing demand for critical metals (e.g., nickel, cobalt and chromium) that are needed for the production and storage of cleaner energy. Ultramafic ore deposits are major hosts for such metals. Historical tailings from ultramafic mines are increasingly being viewed as a source of critical metals, but the distribution and abundance of these metals post-mining tends to be imprecisely known. Here, we examine the distribution and abundance of nickel, cobalt and chromium in weathered tailings from the historical Lord Brassey nickel mine in Tasmania, Australia. We test the utility of three analytical approaches; quantitative X-ray diffraction (QXRD), electron probe micro-analysis (EPMA) and whole rock elemental analysis, for assessing the grade and recoverability of these metals from tailings. Heazlewoodite (Ni_3S_2) and awaruite (Ni_3Fe) were detectable using XRD in a subset of samples and spinels were detectable in every sample, but it was not possible to determine their stoichiometry using XRD alone. EPMA data confirmed the major sources of nickel to be heazlewoodite and awaruite, cobaltpentlandite (Co_9S_8) to be the major host of cobalt, and chromite ($FeCr_2O_4$) to be the major host of chromium. Whole rock elemental compositions were calculated from the integration of QXRD and EPMA data for comparison with industry measured whole rock elemental data. The calculated results revealed that serpentine is another major source of nickel due to the high abundance counteracting the low oxide wt%, and the similarity of the combined QXRD and EPMA results with the measured elemental abundance data justify their use in the economic assessment of ore deposits and tailings. Measured whole rock elemental analysis results show that tailings from Lord Brassey qualify as low-grade nickel and cobalt ore, while the calculated results from integrated QXRD and EPMA data provide accurate and precise geometallurgical context for the distribution of nickel and cobalt amongst sulfides, alloys, oxides, silicates and other minerals. Our results demonstrate that integrating QXRD and EPMA datasets provides estimates of whole rock geochemistry that are comparable to standard industry whole rock analysis methods while providing much-needed context about the complex and evolving mineralogy of critical metals in mine tailings. A better

geometallurgical understanding of the mineralogy, and the grade, of tailings offers enticing possibilities for including reprocessing as part of a tailings management strategy.

3.2. Introduction

As the global population increases in size and wealth, a number of "critical metals" are needed in order to build a more sustainable and more digitized economy (Government of Canada, 2021). Critical metals are so named due to their significance in several important fields (ex. medicine, agriculture, information technology), their major role in the production of renewable and environmentally responsible energies and due to their finite and rapidly depleting supply. Examples of such metals include nickel, cobalt and chromium (used in electronics, batteries and stainless steel), (Bacon et al., 2002; Sovacool, 2019; Bystrov et al., 2021; Government of Canada, 2021).

As the resources from mining are finite, companies are resorting to exploring at greater depths, in more isolated localities and to reducing ore cutoff grade at mines to meet demand (Lutandula and Maloba, 2013). The reprocessing of mining waste such as tailings, of which the mining industry produces roughly 8–14 billion tonnes annually, is one solution to the issue of where to find critical metals (Lutandula and Maloba, 2013; Parbhakar-Fox et al., 2018; Baker et al., 2020). Tailings are the "uneconomic" products of the ore processing circuit, regarded as such due to their low resource content. Once milled and separated from the valuable material, tailings are dumped into subaerial or subaqueous storage facilities where they now may pose geoenvironmental or health risks such as acid mine drainage or aerosol ejection (Adiansyah et al., 2015; Parbhakar-Fox et al., 2018; Stankovic et al., 2018; Park et al., 2019). Historically these wastes were sometimes abandoned due to the costs of remediation, increasing the chances of geoenvironmental catastrophe occurring (Adiansyah et al., 2015; Schoenberger, 2016; Figueiredo et al., 2019b). Nowadays, there are many forms of tailings management practiced, such as: incorporating tailings into structural and construction projects, remediation through revegetation or burial, prolonged storage and monitoring in the aforementioned tailings storage facilities (TSF), or reprocessing (Meyer, 1980; West High Yield Resources, 2013; Power et al., 2014; Slack et al., 2017; Stefaniak and Wróżyńska, 2017; Figueiredo et al., 2019a). Companies may recover critical metals from tailings that are already under their ownership to reduce environmental impacts and

waste output. Once thought to be useless, dangerous and problematic, mine tailings can be reprocessed for valuable metals and this concept is becoming worthy of recognition, consideration and exploration (Alcalde et al., 2018; Figueiredo et al., 2019b). Ultramafic mine tailings are of a particular interest due to their potential to host economic concentrations of critical metals such as nickel, cobalt and chromium (Rampacek, 1982; Wilson et al., 2006; Kandji et al., 2017; Hamilton et al., 2018; Government of Canada, 2021). These tailings also weather to produce carbonate minerals that can sequester atmospheric carbon and retain it for over tens of thousands of years, which may aid in reducing global atmospheric carbon dioxide (CO_2) concentrations (Lackner, 2003; Wilson et al., 2006; Wilson et al., 2009a; Wilson et al., 2014).

In order to determine how economic a mineral deposit is, the ore is assigned a grade based on the concentration of the valuable mineral or element therein, with "high-grade" containing lots of the resource and "low-grade" containing sparse amounts (Britannica, 2021). The grade is dependent on what resource is being sought, for example: >0.6% nickel is considered low-grade and economic, whereas >0.01% cobalt is considered low-grade and economic (EMEW Clean Technologies, 2017; Slack et al., 2017). Ore with a grade that falls below a certain value (known as the cutoff grade) is considered unprofitable to mine and process despite hosting the valuable resource (Britannica, 2021). These parameters are calculated by taking into account the production expenditures, sales recuperations and most importantly, the resource estimates. There are a number of ways to determine the valuable contents of ore (known as assaying) and assign it a grade, from ancient combustion methods, wet methods such as chemical titration, and the modern approach of instrumental assessment (AngloAmerican, 2022). Ore deposits are commonly assessed by elucidating tonnage from drill core, but tailings, which have been milled and disregarded as "uneconomic" already, must be assessed using the aforementioned assaying methods. The most common instrumental techniques for whole rock analysis are inductively coupled plasma – mass spectrometry (ICP-MS) and X-ray fluorescence (XRF) spectrometry, which provide the elemental abundances of the whole rock sample (e.g., Keays and Jowitt, 2013; Britten, 2017; Parbhakar-Fox et al., 2018; Ostadrahimi et al., 2020). While knowing the elemental composition of rocks is important for an economic assessment, the understanding of the mineralogical abundances and compositions will provide more insight into elemental behavior per deposit and assist in targeted recovery of resources. Whole rock analyses, such as ICP-MS and XRF, fall short, as they cannot be used to distinguish where the valuable resources are within an ore sample. These methods can

neither provide context about preferential sources and sinks for valuable elements nor elemental distribution amongst the minerals in an ore body. Therefore, other methods must be incorporated to cover this gap in the knowledge.

Here we test whether it is possible to use quantitative mineralogical data to confidently assign an ore grade to tailings samples from a derelict, ultramafic-hosted nickel deposit. We assess whether calculated elemental abundances from this mineralogically rich dataset are comparable to measured results from a traditional industry whole rock analysis.

We examine the same ultramafic mine tailings from the Lord Brassey mine, Tasmania from Chapter 2, to ascertain mineral abundances, mineral compositions and whole rock elemental abundances with a focus on transition metal contents. The qualitative assessment of Lord Brassey mine tailings was done in Chapter 2 to identify which minerals host critical transition metals (Ni and Co). Samples were analyzed using quantitative X-ray diffraction (QXRD) and electron probe micro-analysis (EPMA) and these datasets were integrated to produce calculated whole rock elemental compositions. Calculated whole rock elemental compositions were compared with whole rock XRF, ICP-MS and inductively coupled plasma – optical emission spectrometry (ICP-OES) results to gauge the accuracy of the QXRD + EPMA methodology. The aim of this study is to investigate the transition metal content of the various mineral phases within the Lord Brassey mine tailings samples to boost our understanding of transition metal distribution and partitioning, while creating an analytical tool that provides geometallurgical context about mineral abundance and mineral composition, while accurately reflecting measured whole rock elemental abundances.

3.3. Materials & Methods

3.3.1. Field Site & Samples

The derelict Lord Brassey mine is located in western Tasmania, Australia within the Heazlewood district, roughly 240 km northwest of Hobart (Fig. 3.1A, B). Heazlewoodite (Ni_3S_2) was mined at Lord Brassey in 1896 and again in the 1950s via a single adit (Anderson et al., 2002). The Lord Brassey mine is situated in the Heazlewood River Mafic-Ultramafic Complex, which is composed of Cambrian age serpentinized ultramafics with an ophiolitic origin (alpine-type ultramafic complex), (Anderson et al. 2002). The area is praised and pilfered by collectors for its

abundance of nickel carbonates, such as zaratite [$Ni_3CO_3(OH)_4 \bullet 4H_2O$], hellyerite ($NiCO_3 \bullet 6H_2O$), and nickel sulfide minerals, especially heazlewoodite (Anderson et al., 2002). The site was visited in July 2014 and over 50 geological samples were collected from two tailings piles (Mililli, 2014). Of these samples, 9 rock samples were analyzed in detail as part of this study. Samples coated with alteration minerals were preferentially selected to examine how weathering affects which minerals host critical transition metals (Fig. 3.1C, D).

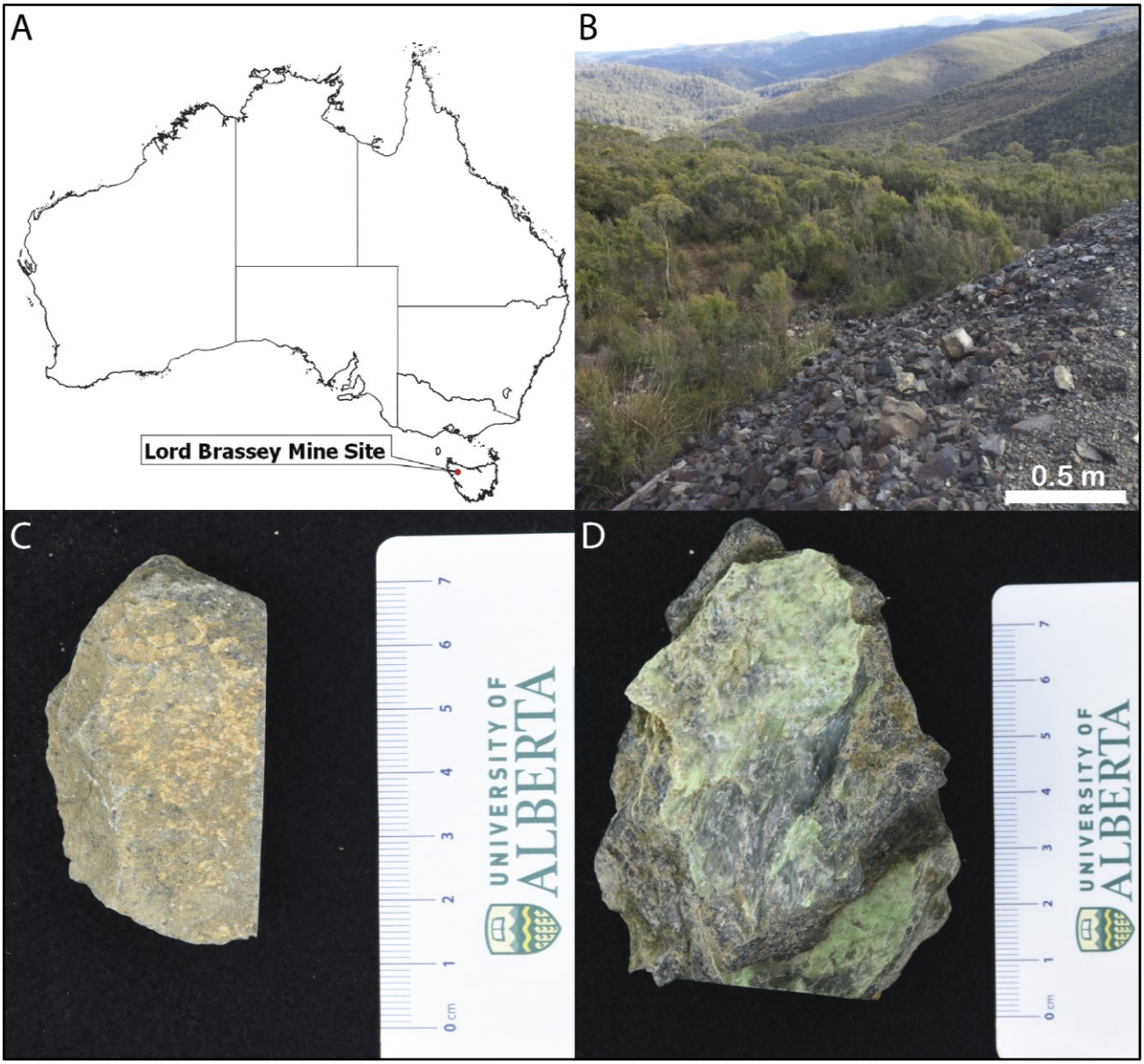

Fig. 3.1. A) The Lord Brassey mine site location within Australia. B) Lord Brassey tailings pile. Examples of Lord Brassey samples coated with (C) "orange" and (D) "green" alteration minerals.

3.3.2. Quantitative X-ray Diffraction (QXRD)

Samples were crushed with a hammer before being pulverized for seven minutes in a Spex shatterbox using a tungsten dish. Afterwards, 5 mL aliquots of powder were micronized for an additional seven minutes under ethanol with a McCrone micronizing mill containing agate grinding pellets. XRD patterns were obtained using a Rigaku Ultima IV diffractometer in the Department of Earth & Atmospheric Sciences XRD Lab, University of Alberta. The Rigaku Ultima IV has a D/Tex Ultra detector and a Co X-ray tube which operates at 38 kV and 38 mA. All XRD patterns were collected over a 2θ range of 3–80° using a step size of 0.02° 2θ and a dwell time of 1 second/step. Mineral phases were identified from the resulting XRD patterns with reference to the ICDD PDF 4+ database with the program DIFFRAC.EVA (Bruker AXS).

A calcium-exchange was performed on samples that contained smectites in order to stabilize the position of the 001 peak to a *d*-value of ~15 Å. The calcium exchange procedure of Mervine et al. (2018) was used for this purpose, which involves mixing the micronized sample with 150 mL of 1 M $CaCl_2$•$2H_2O$ in 18.2 MΩ•cm deionized water overnight using a shaker table and filtering multiple times with deionized water. These samples were then reanalyzed using XRD. Phase identification from XRD patterns was also informed by scanning electron microscopy (SEM) observations to justify the inclusion of trace phases.

Rietveld refinements (Rietveld, 1969; Hill and Howard, 1987; Bish and Howard, 1988) with XRD patterns were done using fundamental parameters peak fitting (Cheary and Coehlo, 1998) for all phases in TOPAS 5 (Bruker AXS). The Poorly Ordered or No Known Crystal Structure (PONKCS) method (Scarlett and Madsen, 2006), was used to fit the peaks of structurally disordered clay minerals. PONKCS models were made using XRD patterns collected from three 50:50 wt% mixtures of NIST 676a α-Al_2O_3 and (1) an in-house lizardite standard (Wilson et al., 2009b), (2) an in-house antigorite standard (Wilson et al., 2006) and (3) Ca-exchanged SWy-2 montmorillonite obtained from the Clay Minerals Society Source Clay Repository. Unit-cell parameters and space groups were obtained from Mellini and Viti (1994) for lizardite, from Uehara (1998) for antigorite, and from Viani et al. (2002) for Ca-montmorillonite. Montmorillonite was used as a proxy for the trioctahedal smectites most commonly found in weathered serpentinites. Peaks for these three clay phases were fitted using the Pawley method (Pawley, 1981), without reference to atomic scattering information, to refine a calibrated mass, *ZM*, value for the unit cell

of each phase. The March-Dollase correction (March, 1932; Dollase, 1986) for preferred orientation was used to model the peaks of diopside. A default Brindley radius of 2.5 μm was used to account for microabsorption contrast (Brindley, 1945).

Refinements were done a number of times, incorporating SEM and EPMA observations to justify the inclusion of low abundance phases in the models. Some phases observed via SEM and EPMA were present in quantities below the level of detection for QXRD (which is between 0.1 and 0.5 wt% under the conditions employed here) and were therefore not included in the final models. The weighted profile R-factor (R_{wp}), Durbin Watson (DW) statistic and goodness of fit (χ^2) are reported alongside modelled wt% mineral abundances.

3.3.3. Scanning Electron Microscopy (SEM) and Energy Dispersive X-ray Spectroscopy (EDS)

SEM was performed in the Department of Earth & Atmospheric Sciences at the University of Alberta using a Zeiss Sigma 300 Variable Pressure Field Emission Scanning Electron Microscope (VP-FESEM). The SEM has a 30 μm aperture which provided a beam current of 315 pA, and uses a field emission gun with a tungsten filament. This instrument is equipped with dual silicon drift detectors (Bruker AXS), each with a resolution of 123 eV and an area of 60 mm^2. Imaging was performed with a backscattered electron (BSE) detector in variable pressure mode at roughly 50 Pa. The accelerating voltage was set at 25 kV and no conductive coating was applied to the samples.

3.3.4. Electron Probe Micro-Analysis (EPMA)

EPMA was conducted using a CAMECA-SX100 instrument in the Electron Microprobe Laboratory at the University of Alberta. Thin sections were coated with 25 nm of amorphous carbon. Measurements were made with wavelength dispersive spectrometry (WDS) while the Probe-for-EPMA software (Donovan et al. 2015) corrected for the effects of dead-time. Limits of detection at 99% confidence were determined in the Probe-for-EPMA software to indicate the lowest concentration of analyte measureable with 99% certainty (Potts, 1992).

Twelve elements were measured for the silicate, oxide, pyroxene and chalcophanite-group minerals (Na, Ca, Fe, Mg, Ti, Mn, Al, Cr, Ni, K, Si, and V) and reported as oxides. The operating

conditions were: 15 kV accelerating voltage, 20 nA beam current and varied beam size (5 μm for silicates and <1 μm for the others). For peaks and backgrounds, the count times used were: 30 seconds for Na, Ca, Fe, Ti, Mn, Cr, Ni, K, V, 40 seconds for Si, Al, and 60 seconds for Mg. The X-ray lines, diffraction crystals, and standards were: Na *K*α, LTAP, albite; Ca *K*α, PET, diopside; Fe *K*α, LLIF, fayalite (except Gore Mountain garnet used for chromite); Mg *K*α, LTAP, pyrope (except diopside used for pyroxene and chalcophanite); Ti *K*α, PET, synthetic rutile; Mn *K*α, LLIF, spessartine; Al *K*α, TAP, labradorite; Cr *K*α, PET, synthetic Cr_2O_3; Ni *K*α, LLIF, synthetic Ni; Kα, LPET, sanidine; Si *K*α, TAP, pyrope; and V *K*α, LPET, synthetic vanadium. The intensity of the data was corrected for Time Dependent Intensity (TDI) loss (or gain) using a self-calibrated correction for Na *K*α, Ca *K*α, Fe *K*α, K *K*α, Si *K*α, and corrections were applied to Mn for interference by Cr, to Cr for interference by V, and to V for interference by Ti (Donovan et al., 1993). The X-ray intensity data were reduced following Armstrong (1988) and included oxygen calculated by stoichiometry.

Fifteen elements were measured for sulfides and alloys (Mg, S, Cu, Fe, Si, Ag, Zn, Cd, Co, Mn, As, Mo, Ni, Cr and Pb). The operating conditions were: 20 kV accelerating voltage, beam current of 20–30 nA and beam size of <1 μm (fully focused beam). For peaks and backgrounds, a count time of 30 seconds was used for all elements. The X-ray lines, diffraction crystals, and standards were: Mg *K*α, LTAP, dolomite; S *K*α, PET, marcasite; Cu *K*α, LLIF, synthetic copper; Fe *K*α, LLIF, pyrrhotite for sulfides and synthetic iron for alloys; Si *K*α, LTAP, sanidine; Ag *K*α, PET, synthetic acanthite; Zn *K*α, LLIF, synthetic sphalerite; Cd *K*α, PET, synthetic cadmium sulfide; Co *K*α, LLIF, synthetic cobalt; Mn *K*α, PET, alabandite; As *K*α, LLIF, synthetic gallium arsenide; Mo *K*α, PET, synthetic molybdenum; Ni *K*α, LLIF, synthetic nickel; Cr *K*α, PET, synthetic Cr_2O_3; and Pb *K*α, PET, synthetic galena. Interference corrections were applied to Mg and Cd for interference by Ag; to S for interference by both Co and Mo; to Si for interference by Co; to Fe, As, and Cr for interference by Pb; and to Ag and Mn for interference by Cr (Donovan et al., 1993). In order to improve the X-ray counting statistics for sulfur, two spectrometers were used for its measurement and their net intensities aggregated (Donovan et al., 2011).

Final formulae were calculated for serpentine and chlorite using the Excel program developed by Yavuz et al., (2015) based on 10 oxygen atoms and 8 hydroxyl groups. Final wt%

values were based on the stoichiometric H_2O, ferrous and ferric iron abundances. Analyses with Al_2O_3 contents greater than 12 wt% were considered to be for chlorite after the empirical suggestions of Gillery (1959). Serpentine formulae were then recalculated for 5 oxygen atoms and 4 hydroxyl groups. Garnet stoichiometry was determined using the Excel program developed by Locock, (2008) on the basis of 12 oxygen atoms and adjusting H_2O to fill the tetrahedral site. Stoichiometry was used to separate the values into the appropriate site for ferrous and ferric iron, as well as Mn^{2+} and Mn^{3+}, resulting in final wt% values and garnet end-member concentrations. For the spinels, an unpublished program from the University of Alberta Electron Microprobe Laboratory website for anhydrous oxides was used, with initial oxide wt% values used to calculate stoichiometry, which is in turn used to differentiate between ferrous and ferric iron wt%. For jianshuiite, an unpublished general formula program, also from the University of Alberta Electron Microprobe Laboratory website, was used to calculate H_2O content based on oxide wt% values, and then the stoichiometry based on the generated formula.

3.3.5. Whole Rock Analysis

Whole rock analysis was performed by SGS Minerals based in Burnaby, Canada. Samples were pulverized by the same method used for XRD analysis (section 3.3.2. above), but were not micronized. Carbon and sulfur contents were collected via a LECO carbon–sulfur analyzer, in which samples are combusted in a ceramic crucible at 1350 °C and converted into CO_2 and SO_2 for measurement by infrared absorption. For major-element abundances, an aliquot of each sample was first fused with a lithium tetraborate/metaborate mixture into a homogenous glass disk. These prepared disks were then analyzed with wavelength dispersive X-ray fluorescence (WD-XRF) spectroscopy. The loss on ignition (LOI_V) was determined separately and gravimetrically at 1000 °C and the final abundances were reported as oxides. For minor-element and trace-element abundances, a portion of each sample was digested and fused in a glassy carbon crucible using sodium peroxide (Na_2O_2) and then dissolved in HNO_3, before being analyzed using inductively coupled plasma mass spectrometry (ICP-MS) for elements requiring a lower detection limit, and inductively coupled plasma optical emission spectrometry (ICP-OES) for elements that had a higher abundance. These standard industrial laboratory methodologies were validated through the use of reference materials, blanks, replicates and duplicates. The reference materials used were:

GS314-2 for the carbon-sulfur analysis (CSA), OREAS751 for the WD-XRF, and both OREAS 681 and OREAS 70b for the ICP-MS and ICP-OES.

3.3.6. Data Integration & Error Propagation

Once collection and processing of the QXRD and EPMA data were complete, they were integrated to calculate whole rock elemental abundances. The oxide wt% data for each point measured with EPMA for each mineral in each sample were averaged to obtain an overall mean oxide wt% for individual mineral species. EPMA data were converted to the identical whole rock analysis oxide through conversion factors if different stoichiometric oxides were present in the data analysis output (e.g. Ni converted to NiO). These EPMA values were scaled by the wt% mineral abundances from QXRD for the corresponding mineral and sample, which were then summed to produce oxide wt% values for the whole sample. The resulting calculated oxide wt% values (from the combined QXRD and EPMA data, Table A.4) were plotted against the measured oxide wt% values from the industry whole rock analysis (LOI_V, XRF, ICP-MS and ICP-OES). As some samples, or mineral phases within a particular sample, were not analyzed using EPMA, an average of the collected points for each mineral phase across all analyzed samples was substituted when necessary. The oxide wt% values of stoichiometric brucite were assumed in calculations because EPMA data could not be collected from this mineral.

Error propagation was carried out with errors added in quadrature, to account for (1) the uncertainty of the different analytical methods, (2) the use of numerous data points, each with its own error, and (3) the heterogeneity of mineral compositions within the samples (Ku, 1966; Giaramita and Day, 1990; Potts, 1992). First, the relative uncertainty of the EPMA data was calculated for each different oxide within each mineral phase for each individual sample, by dividing the measured absolute uncertainty value by the corresponding oxide wt% value. The relative uncertainty of the QXRD data was calculated for each mineral phase for each sample, by dividing the absolute uncertainty by the corresponding refined mineral abundance in wt%. Uncertainties on refined mineral abundances were found or extrapolated from QXRD studies using synthetic ultramafic rocks made from weighed mixtures of standard minerals (Wilson et al., 2006; Wilson et al., 2009a; Turvey et al., 2018). On a per sample basis, the relative uncertainties of the EPMA oxide data and the corresponding QXRD mineral phase abundances (for each individual

oxide in each mineral phase) were added in quadrature to yield the combined relative uncertainty of each oxide per mineral phase. These relative uncertainties were multiplied by the whole rock portion of oxide per mineral phase (the QXRD mineral wt% multiplied by the EPMA mineral phase oxide wt%) to yield the whole rock absolute uncertainties for each oxide per the individual mineral phases. Finally, these calculated absolute uncertainties (for all the mineral phases in the sample) were added in quadrature to yield the whole rock absolute uncertainties of the data integration, for each oxide that was measured. For samples lacking any EPMA uncertainty data, the corresponding known uncertainties were added in quadrature and used in place (e.g. calculated final MgO absolute uncertainties for serpentine in all samples added in quadrature and used as serpentine absolute uncertainty for samples with no serpentine EPMA data). Uncertainties from the industry whole rock analysis (LOI_V, XRF, ICP-MS and ICP-OES) were calculated from the results of replicate analyses.

3.4. Results

3.4.1. Elemental Compositions

The samples are dominated by silicon and magnesium (together, roughly 80 wt% of bulk composition) (Table A.2). Iron, aluminum, calcium and loss on ignition (e.g., water, carbon, sulfur) make up roughly an additional 15 wt% of the bulk composition. Nickel and chromium are observed in some samples, each reaching up to 0.7 wt% while manganese reached almost 0.2 wt% in one case (14LBM1-3). Cobalt averaged ~0.01 wt% in all samples whereas cadmium and copper fell below their limits of detection despite being visible in some micrometer-scale sulfide grains using SEM and X-ray fluorescence microscopy mapping (Chapter 2) (Table A.2).

3.4.2. Mineralogical Compositions

The mineralogical compositions of the Lord Brassey samples acquired from QXRD were dominated by a small number of minerals with some trace phases. Serpentine [$Mg_3Si_2O_5(OH)_4$, primarily lizardite with minor amounts of its polymorph antigorite] was the major component of the samples with minor chlorite [clinochlore, $(Mg,Fe^{2+})_5Al(Si_3Al)O_{10}(OH)_8$] (Table 3.1). All samples contained minor amounts of garnet: primarily andradite [$Ca_3Fe_2(SiO_4)_3$] and some grossular [$Ca_3Al_2(SiO_4)_3$] presented in a solid solution which was modeled in Rietveld refinements

as two separate components based on presence of two discrete sets of garnet peaks. All samples also contained spinels: mostly chromite ($FeCr_2O_4$) with some magnetite (Fe_3O_4) present as distinct but co-occurring phases (Table 3.1). Trace amounts of diopside ($CaMgSi_2O_6$), brucite [$Mg(OH)_2$], jianshuiite [$(Mg,Mn,Ca)Mn_3O_7 \cdot 3H_2O$], heazlewoodite ($Ni_3S_2$) and awaruite ($Ni_3Fe$) were detected in XRD patterns with confirmation from SEM and electron microprobe data. The R_{wp} values for Rietveld refinements were all below 10%, meaning most of the area under the observed peaks fell within the calculated model (Toby, 2006; Kniess et al., 2012).

Serpentine and chlorite do not host >1.5 oxide wt% of any critical transition metals and are distinguished from each other in this study empirically by their aluminum content being above (chlorite) or below (serpentine) 12 wt% (Gillery, 1959) (Table 3.2, 3.3, 3.4, 3.5). The garnets are mainly andradite with minor amounts of grossular and they are relatively uniform in composition (Table 3.6, 3.7, 3.8). EPMA data establish that garnets are not notable sources of critical transition metals. For the spinels, the magnetite was uniform in composition and the chromite was much more varied (Table 3.9, 3.10). Chromite contained the largest oxide wt% values for chromium of any minerals within the samples (>44 oxide wt% on average across all samples). EPMA was used to confirm the presence of the nickel sulfide phase as heazlewoodite and the nickel-bearing alloy as awaruite (Table 3.11), with both minerals containing over 70 wt% Ni. Other common sulfides were identified as cobaltpentlandite (Co_9S_8), anilite (Cu_7S_4), hawleyite/greenockite (CdS) which are polymorphs, and molybdenite (MoS_2) (Table 3.12). These phases were all undetectable in the QXRD analysis due to their low abundances. The presence of diopside and jianshuiite at trace abundances was also confirmed via EPMA, but only jianshuiite hosts a significant amount of a critical transition metal (manganese) (Table 3.13).

Table 3.1. Quantitative X-ray diffraction data of mineralogical abundances in Lord Brassey samples.

Sample	14LBM1-3	14LBM1-5	14LBM1-9	14LBM1-10	14LBM1-19	14LBM1-21	14LBM1-28	14LBM1-31	14LBM1-32
Mineral	(wt%)	(wt%)	(wt%)	(wt%)	(wt%)	(wt%)	(wt%)	(wt%)	(wt%)
Lizardite	62.0	68.0	65.3	71.6	72.8	77.7	64.5	74.7	73.8
Antigorite	18.7	9.7	22.5	19.5	18.9	15.0	17.3	12.8	19.6
Clinochlore	6.3	7.5	3.5	2.0	2.0	1.8	8.7	6.1	2.0
Diopside		1.7							
Andradite	12.3	12.4	4.9	5.6	0.6	1.7	7.1	0.6	0.5
Grossular			1.3				1.2		
Magnetite		0.1	1.1	0.6		3.1	0.8		
Chromite	0.7	0.5	0.8	0.7	5.7	0.7	0.4	5.5	3.7
Jianshuiite			0.2						
Brucite			0.4						0.4
Heazlewoodite		0.1						0.1	
Awaruite								0.2	
Total	100.0	100.0	100.0	100.0	100.0	100.0	100.0	100.0	100.0
R_{WP} [1] (%)	3.6	3.2	3.8	3.7	3.7	3.7	3.9	3.9	4.2
DW [2]	0.2	0.2	0.1	0.1	0.1	0.1	0.1	0.1	0.1
χ^{2} [3]	3.4	3.0	3.9	3.7	4.0	3.8	3.8	3.9	4.3

[1]Weighted profile R-factor percentage indicating area under the peak unaccounted for by model.

[2]Durban Watson statistic for serial correlation.

[3]Chi-squared statistic for goodness of fit.

Table 3.2. Electron microprobe analyses of serpentine in Lord Brassey samples.

Sample	14LBM1-3[1]		14LBM1-9[1]		14LBM1-10[1]		14LBM1-21[1]		14LBM1-28[1]		AVERAGE[1]	
Oxide	wt%	n=6	wt%	n=20	wt%	n=26	wt%	n=21	wt%	n=40	wt%	N=5
SiO_2	41.92	(1.60)	37.48	(2.44)	39.18	(1.67)	38.09	(0.89)	38.17	(2.89)	38.97	(4.52)
TiO_2	0.01	(0.01)	0.01	(0.04)	0.01	(0.02)	0.00	(0.01)	0.02	(0.03)	0.01	(0.06)
Al_2O_3	1.17	(0.87)	5.91	(3.06)	3.18	(2.41)	1.85	(1.36)	3.23	(3.91)	3.07	(5.76)
FeO [(2)]	3.53	(0.92)	4.32	(2.87)	4.94	(3.03)	3.11	(0.85)	4.57	(1.47)	4.10	(4.60)
Fe_2O_3 [(2)]	0.44	(0.11)	0.53	(0.35)	0.61	(0.37)	0.38	(0.11)	0.56	(0.18)	0.51	(0.57)
Cr_2O_3	0.36	(0.20)	0.14	(0.09)	0.66	(0.62)	0.17	(0.12)	0.53	(0.48)	0.37	(0.82)
MnO	0.19	(0.09)	0.10	(0.06)	0.15	(0.05)	0.09	(0.04)	0.17	(0.05)	0.14	(0.14)
MgO	39.50	(1.78)	38.71	(4.11)	37.81	(3.13)	40.71	(0.79)	38.18	(2.93)	38.98	(6.25)
NiO	0.14	(0.04)	0.12	(0.03)	0.14	(0.08)	0.22	(0.07)	0.24	(0.25)	0.17	(0.27)
CaO	0.11	(0.03)	0.09	(0.39)	0.06	(0.06)	0.03	(0.02)	0.05	(0.04)	0.07	(0.40)
Na_2O	0.00	(0.01)	0.01	(0.03)	0.02	(0.03)	0.00	(0.01)	0.00	(0.00)	0.01	(0.04)
K_2O	0.00	(0.00)	0.01	(0.01)	0.02	(0.02)	0.00	(0.00)	0.00	(0.00)	0.01	(0.02)
H_2O^+	12.74	(0.05)	12.64	(0.18)	12.62	(0.22)	12.73	(0.06)	12.63	(0.11)	12.67	(0.32)
Total	100.11	(1.14)	100.07	(0.37)	99.40	(1.21)	97.38	(0.73)	98.35	(4.51)	99.08	(4.88)

[1]Uncertainties in parentheses for analyzed quantities are reported to 1σ.

[2]Ferrous and ferric iron wt% calculated by stoichiometry.

Abbreviations: n = number of points taken for the sample. N = number of sample set averages used for calculation.

Table 3.3. Formula proportions for serpentine in Lord Brassey samples, based on 5 oxygen atoms and 4 hydroxyl groups.

Sample	14LBM1-3[1]		14LBM1-9[1]		14LBM1-10[1]		14LBM1-21[1]		14LBM1-28[1]		AVERAGE[1]	
Element	apfu	n=6	apfu	n=20	apfu	n=26	apfu	n=21	apfu	n=40	apfu	N=5
Tetrahedral												
Si	1.968	(0.049)	1.774	(0.098)	1.875	(0.071)	1.856	(0.045)	1.849	(0.072)	1.864	(0.155)
Al	0.036	(0.044)	0.223	(0.103)	0.122	(0.074)	0.099	(0.063)	0.086	(0.088)	0.113	(0.172)
Octahedral												
Al	0.030	(0.021)	0.109	(0.086)	0.059	(0.067)	0.017	(0.018)	0.090	(0.130)	0.059	(0.171)
Ti	0.000	(0.001)	0.000	(0.001)	0.001	(0.001)	0.000	(0.001)	0.001	(0.001)	0.000	(0.001)
Fe^{2+}	0.139	(0.038)	0.172	(0.048)	0.198	(0.123)	0.127	(0.035)	0.184	(0.054)	0.164	(0.151)
Fe^{3+}	0.016	(0.004)	0.019	(0.006)	0.022	(0.014)	0.014	(0.004)	0.021	(0.006)	0.018	(0.017)
Cr	0.014	(0.008)	0.005	(0.007)	0.025	(0.024)	0.007	(0.005)	0.020	(0.018)	0.014	(0.031)
Mn	0.008	(0.004)	0.004	(0.001)	0.016	(0.002)	0.004	(0.002)	0.007	(0.002)	0.006	(0.005)
Ni	0.006	(0.002)	0.005	(0.005)	0.016	(0.003)	0.009	(0.003)	0.010	(0.010)	0.007	(0.012)
Mg	2.765	(0.099)	2.733	(0.120)	2.696	(0.209)	2.957	(0.047)	2.774	(0.335)	2.785	(0.427)
Interlayer												
Ca	0.006	(0.002)	0.005	(0.011)	0.003	(0.003)	0.002	(0.001)	0.003	(0.002)	0.004	(0.011)
Na	0.001	(0.001)	0.001	(0.002)	0.002	(0.003)	0.000	(0.001)	0.000	(0.000)	0.001	(0.003)
K	0.000	(0.000)	0.001	(0.001)	0.001	(0.001)	0.000	(0.000)	0.000	(0.001)	0.000	(0.001)
Total	4.989	(0.031)	5.051	(0.025)	5.016	(0.022)	5.082	(0.019)	5.045	(0.103)	5.035	(0.114)

[1]Uncertainties in parentheses for analyzed quantities are reported to 1σ.

Abbreviations: apfu = atoms per formula unit. n = number of points taken for the sample. N = number of sample set averages used for calculation.

Table 3.4. Electron microprobe analyses of chlorite in Lord Brassey samples.

Sample	14LBM1-3[1]		14LBM1-9[1]		14LBM1-10[1]		14LBM1-21[1]		14LBM1-28[1]		AVERAGE[1]	
Oxide	wt%	n=6	wt%	n=8	wt%	n=11	wt%	n=1	wt%	n=14	wt%	N=4
SiO_2	31.56	(0.82)	31.11	(2.57)	33.49	(0.63)	31.69	N/A	32.25	(0.39)	32.02	(2.79)
TiO_2	0.00	(0.00)	0.05	(0.01)	0.02	(0.02)	0.00	N/A	0.01	(0.02)	0.02	(0.03)
Al_2O_3	17.43	(1.68)	16.58	(3.14)	13.64	(0.84)	14.11	N/A	14.84	(1.20)	15.32	(3.85)
FeO [(2)]	4.44	(0.75)	7.21	(1.15)	4.23	(0.22)	6.34	N/A	3.88	(0.84)	5.22	(1.62)
Fe_2O_3 [(2)]	0.55	(0.09)	0.89	(0.14)	0.52	(0.03)	0.78	N/A	0.48	(0.10)	0.64	(0.20)
Cr_2O_3	1.04	(0.08)	0.04	(0.18)	1.13	(0.30)	0.00	N/A	0.94	(0.61)	0.63	(0.71)
MnO	0.02	(0.02)	0.16	(0.03)	0.03	(0.02)	0.14	N/A	0.04	(0.05)	0.07	(0.06)
MgO	33.15	(0.41)	30.89	(2.12)	34.36	(0.44)	33.08	N/A	34.27	(1.52)	33.15	(2.68)
NiO	0.14	(0.02)	0.03	(0.12)	0.17	(0.02)	0.09	N/A	0.25	(0.10)	0.14	(0.16)
CaO	0.04	(0.01)	0.41	(0.21)	0.03	(0.02)	0.08	N/A	0.01	(0.02)	0.12	(0.21)
Na_2O	0.00	(0.01)	0.05	(0.01)	0.01	(0.02)	0.00	N/A	0.00	(0.00)	0.01	(0.02)
K_2O	0.00	(0.01)	0.01	(0.01)	0.02	(0.01)	0.01	N/A	0.01	(0.03)	0.01	(0.04)
H_2O^+	12.60	(0.05)	12.46	(0.08)	12.62	(0.02)	12.50	N/A	12.64	(0.06)	12.56	(0.12)
Total	100.97	(0.26)	99.89	(1.08)	100.27	(0.47)	98.82	N/A	99.62	(0.85)	99.91	(1.47)

[1]Uncertainties in parentheses for analyzed quantities are reported to 1σ, unless only one point was taken.

[2]Ferrous and ferric iron wt% calculated by stoichiometry.

Abbreviations: n = number of points taken for the sample. N = number of sample set averages used for calculation.

Table 3.5. Formula proportions for chlorite in Lord Brassey samples, based on 10 oxygen atoms and 8 hydroxyl groups.

Sample	14LBM1-3[1]		14LBM1-9[1]		14LBM1-10[1]		14LBM1-21[1]		14LBM1-28[1]		AVERAGE[1]	
Element	apfu	n=6	apfu	n=20	apfu	n=26	apfu	n=21	apfu	n=40	apfu	N=5
Tetrahedral												
Si	2.964	(0.081)	2.993	(0.184)	3.167	(0.062)	3.079	N/A	3.072	(0.032)	3.055	(0.213)
Al	1.036	(0.081)	1.007	(0.184)	0.833	(0.062)	0.921	N/A	0.928	(0.032)	0.945	(0.213)
Octahedral												
Al	0.892	(0.106)	0.880	(0.208)	0.687	(0.038)	0.694	N/A	0.738	(0.104)	0.778	(0.259)
Ti	0.000	(0.000)	0.004	(0.003)	0.001	(0.001)	0.000	N/A	0.001	(0.001)	0.001	(0.004)
Fe^{2+}	0.349	(0.060)	0.584	(0.245)	0.335	(0.019)	0.515	N/A	0.309	(0.072)	0.419	(0.263)
Fe^{3+}	0.039	(0.007)	0.065	(0.027)	0.037	(0.002)	0.057	N/A	0.034	(0.008)	0.047	(0.029)
Cr	0.077	(0.006)	0.003	(0.007)	0.084	(0.022)	0.000	N/A	0.071	(0.047)	0.047	(0.053)
Mn	0.001	(0.002)	0.013	(0.005)	0.002	(0.001)	0.012	N/A	0.003	(0.004)	0.006	(0.007)
Ni	0.010	(0.002)	0.003	(0.002)	0.013	(0.002)	0.007	N/A	0.019	(0.008)	0.010	(0.008)
Mg	4.640	(0.059)	4.425	(0.515)	4.844	(0.048)	4.791	N/A	4.865	(0.190)	4.713	(0.554)
Interlayer												
Ca	0.004	(0.001)	0.042	(0.040)	0.003	(0.002)	0.008	N/A	0.001	(0.002)	0.012	(0.040)
Na	0.001	(0.001)	0.009	(0.005)	0.002	(0.003)	0.000	N/A	0.000	(0.000)	0.002	(0.006)
K	0.000	(0.001)	0.001	(0.001)	0.003	(0.002)	0.001	N/A	0.002	(0.004)	0.002	(0.004)
Total	10.013	(0.019)	10.029	(0.047)	10.011	(0.028)	10.085	N/A	10.043	(0.048)	10.037	(0.075)

[1]Uncertainties in parentheses for analyzed quantities are reported to 1σ, unless only one point was taken.
Abbreviations: apfu = atoms per formula unit. n = number of points taken for the sample. N = number of sample set averages used for calculation.

Table 3.6. Electron microprobe analyses of garnets in Lord Brassey samples.

Sample	14LBM1-3[1]		14LBM1-5[1]		14LBM1-9[1]		14LBM1-10[1]		14LBM1-21[1]		14LBM1-28[1]		AVERAGE[1]	
Oxide	wt%	n=21	wt%	n=25	wt%	n=18	wt%	n=20	wt%	n=8	wt%	n=25	wt%	N=6
SiO_2	35.20	(0.60)	34.47	(0.44)	33.51	(1.46)	33.61	(2.45)	33.92	(0.43)	31.95	(1.31)	33.78	(3.25)
TiO_2	0.11	(0.06)	0.06	(0.10)	0.23	(0.38)	1.94	(2.31)	0.15	(0.05)	0.69	(0.87)	0.53	(2.50)
Al_2O_3	3.87	(0.54)	2.21	(1.01)	3.85	(0.80)	1.81	(0.62)	1.89	(0.16)	0.44	(0.25)	2.35	(1.55)
Cr_2O_3	0.72	(0.49)	1.05	(1.63)	0.06	(0.06)	0.95	(0.44)	0.43	(0.22)	0.65	(1.98)	0.64	(2.65)
V_2O_3	0.04	(0.01)	0.01	(0.02)	0.05	(0.06)	0.11	(0.11)	0.02	(0.01)	0.02	(0.03)	0.04	(0.14)
FeO [(2)]	0.18	(0.48)	0.00	(0.00)	0.19	(0.51)	1.54	(1.88)	0.04	(0.08)	0.38	(0.69)	0.39	(2.13)
Fe_2O_3 [(2)]	25.01	(0.93)	26.54	(2.76)	25.14	(1.60)	24.04	(5.50)	27.66	(0.10)	28.82	(2.74)	26.20	(6.99)
MnO [(3)]	0.04	(0.03)	0.00	(0.00)	0.05	(0.02)	0.05	(0.06)	0.09	(0.04)	0.02	(0.02)	0.04	(0.08)
MgO	0.36	(0.14)	0.32	(0.14)	0.41	(0.91)	0.44	(0.67)	0.27	(0.16)	0.22	(0.09)	0.34	(1.17)
CaO	33.55	(0.52)	33.41	(0.19)	33.29	(1.33)	33.42	(0.60)	32.95	(0.46)	33.52	(0.23)	33.36	(1.65)
Na_2O	0.01	(0.01)	0.00	(0.00)	0.02	(0.02)	0.01	(0.02)	0.00	(0.01)	0.00	(0.00)	0.01	(0.03)
H_2O^+ [(4)]	0.76	(0.35)	0.83	(0.26)	1.58	(1.07)	1.56	(1.57)	1.01	(0.26)	2.37	(0.82)	1.35	(2.13)
Total	99.85	(0.38)	98.90	(0.42)	98.38	(0.95)	99.48	(1.21)	98.43	(0.58)	99.08	(0.60)	99.02	(1.84)

[1]Uncertainties in parentheses for analyzed quantities are reported to 1σ.

[2]Ferrous and ferric iron wt% calculated by stoichiometry.

[3]Mn^{2+} wt% calculated by stoichiometry.

[4]H_2O calculated from stoichiometry to fit tetrahedral site.

Abbreviations: n = number of points taken for the sample. N = number of sample set averages used for calculation.

Table 3.7. Electron microprobe stoichiometry for the garnets in Lord Brassey samples, on the basis of 12 oxygen atoms.

Sample	14LBM1-3[1]		14LBM1-5[1]		14LBM1-9[1]		14LBM1-10[1]		14LBM1-21[1]		14LBM1-28[1]		AVERAGE[1]	
Element	apfu	n=21	apfu	n=25	apfu	n=18	apfu	n=20	apfu	n=8	apfu	n=25	apfu	N=6
Tetrahedral														
Si	2.897	(0.048)	2.885	(0.036)	2.781	(0.147)	2.785	(0.215)	2.858	(0.037)	2.670	(0.114)	2.813	(0.293)
H_4	0.104	(0.048)	0.116	(0.036)	0.219	(0.147)	0.216	(0.215)	0.142	(0.037)	0.330	(0.114)	0.188	(0.293)
Octahedral														
Ti	0.007	(0.004)	0.004	(0.006)	0.014	(0.024)	0.121	(0.142)	0.010	(0.003)	0.043	(0.055)	0.033	(0.154)
Al	0.375	(0.051)	0.218	(0.099)	0.377	(0.074)	0.177	(0.059)	0.188	(0.016)	0.043	(0.024)	0.230	(0.149)
Cr	0.047	(0.032)	0.069	(0.107)	0.004	(0.004)	0.062	(0.029)	0.029	(0.014)	0.043	(0.128)	0.042	(0.173)
V	0.003	(0.001)	0.001	(0.001)	0.003	(0.004)	0.007	(0.008)	0.001	(0.000)	0.001	(0.002)	0.003	(0.009)
Fe^{2+}	0.012	(0.003)	0.000	(0.000)	0.013	(0.016)	0.107	(0.131)	0.003	(0.003)	0.027	(0.044)	0.027	(0.139)
Fe^{3+}	1.549	(0.062)	1.671	(0.179)	1.570	(0.107)	1.499	(0.349)	1.754	(0.014)	1.812	(0.178)	1.643	(0.449)
Mg	0.007	(0.014)	0.036	(0.017)	0.018	(0.036)	0.027	(0.032)	0.015	(0.007)	0.027	(0.011)	0.022	(0.054)
Dodecahedral														
Mn^{2+}	0.003	(0.002)	0.000	(0.000)	0.004	(0.002)	0.004	(0.004)	0.006	(0.003)	0.001	(0.001)	0.003	(0.006)
Mg	0.038	(0.012)	0.004	(0.010)	0.033	(0.081)	0.028	(0.054)	0.018	(0.026)	0.000	(0.014)	0.020	(0.103)
Ca	2.958	(0.039)	2.996	(0.013)	2.961	(0.090)	2.967	(0.053)	2.975	(0.033)	3.001	(0.030)	2.976	(0.121)
Na	0.002	(0.002)	0.000	(0.001)	0.003	(0.003)	0.002	(0.003)	0.000	(0.001)	0.000	(0.001)	0.001	(0.005)
Total	8.002	(0.000)	8.000	(0.000)	8.000	(0.000)	8.002	(0.000)	7.999	(0.000)	7.998	(0.000)	8.001	(0.000)

[1]Uncertainties in parentheses for analyzed quantities and are reported to 1σ.

Abbreviations: apfu = atoms per formula unit. n = number of points taken for the sample. N = number of sample set averages used for calculation.

Table 3.8. Garnet end-member composition for Lord Brassey samples.

Sample	14LBM1-3[1]		14LBM1-5[1]		14LBM1-9[1]		14LBM1-10[1]		14LBM1-21[1]		14LBM1-28[1]		AVERAGE[1]	
End-members	wt%	n=21	wt%	n=25	wt%	n=18	wt%	n=20	wt%	n=8	wt%	n=25	wt%	N=6
Katoite	3.48	(1.61)	3.86	(1.27)	7.29	(4.89)	7.19	(5.29)	4.73	(1.25)	2.17	(1.20)	4.79	(7.68)
Hydroandradite	0.00	(0.00)	0.00	(0.00)	0.00	(0.00)	0.00	(0.00)	0.00	(0.00)	8.84	(4.49)	1.47	(4.49)
Morimotoite	0.68	(0.31)	0.00	(0.00)	1.32	(1.63)	10.67	(13.14)	0.28	(0.25)	2.66	(4.38)	2.60	(13.95)
NaTi garnet	0.00	(0.00)	0.00	(0.00)	0.06	(0.09)	0.08	(0.16)	0.00	(0.00)	0.00	(0.00)	0.02	(0.18)
Morimotoite-Mg	0.00	(0.00)	0.38	(0.60)	0.00	(0.00)	1.26	(1.28)	0.67	(0.44)	1.68	(1.37)	0.67	(2.02)
Goldmanite	0.13	(0.04)	0.03	(0.07)	0.17	(0.19)	0.37	(0.38)	0.07	(0.02)	0.07	(0.11)	0.14	(0.44)
Uvarovite	2.34	(1.59)	3.47	(5.36)	0.20	(0.20)	3.11	(1.44)	1.43	(0.71)	2.15	(6.38)	2.12	(8.63)
Spessartine	0.09	(0.07)	0.00	(0.00)	0.12	(0.06)	0.12	(0.08)	0.21	(0.10)	0.00	(0.00)	0.09	(0.16)
Pyrope	1.25	(0.45)	0.13	(0.35)	1.09	(2.70)	0.93	(0.59)	0.61	(0.57)	0.00	(0.00)	0.67	(2.88)
Grossular	13.94	(4.08)	6.90	(4.77)	10.34	(4.36)	0.61	(2.95)	3.83	(1.95)	0.00	(0.00)	5.94	(8.42)
Andradite	77.43	(3.08)	83.57	(8.78)	78.51	(5.37)	74.95	(19.47)	87.70	(0.77)	81.77	(10.79)	80.66	(24.73)
Remainder	0.64	(0.63)	1.64	(0.92)	0.91	(1.60)	0.72	(1.60)	0.46	(0.29)	0.67	(0.68)	0.84	(2.63)
Total	99.98	(0.01)	99.98	(0.01)	100.01	(0.01)	100.01	(0.01)	99.99	(0.01)	100.01	(0.01)	100.01	(0.02)

[1]Uncertainties in parentheses for analyzed quantities and are reported to 1σ.

Abbreviations: n = number of points taken for the sample. N = number of sample set averages used for calculation.

Table 3.9. Electron microprobe analyses of spinels in Lord Brassey samples.

Sample - Chromite	14LBM1-3[1]		14LBM1-5[1]		14LBM1-21[1]		14LBM1-28[1]		AVERAGE[1]	
Oxide	wt%	n=1	wt%	n=3	wt%	n=8	wt%	n=9	wt%	N=4
Na_2O	0.00		0.01	(0.01)	0.00	(0.00)	0.04	(0.10)	0.01	(0.04)
MgO	2.97		10.28	(0.08)	10.27	(0.41)	2.15	(0.62)	6.42	(0.37)
Al_2O_3	7.37		21.23	(1.31)	19.98	(0.89)	4.20	(1.15)	13.19	(1.11)
SiO_2	0.05		0.01	(0.01)	0.01	(0.01)	0.23	(0.57)	0.07	(0.20)
CaO	0.46		0.07	(0.06)	0.00	(0.00)	0.01	(0.01)	0.13	(0.03)
TiO_2	0.16		0.16	(0.12)	0.17	(0.06)	0.64	(0.25)	0.28	(0.14)
V_2O_3	0.31		0.17	(0.04)	0.18	(0.01)	0.34	(0.14)	0.25	(0.06)
Cr_2O_3	52.98		44.63	(1.39)	45.30	(0.92)	44.53	(3.19)	46.86	(1.84)
MnO	0.38		0.27	(0.01)	0.26	(0.02)	0.52	(0.17)	0.36	(0.07)
NiO	0.00		0.09	(0.02)	0.09	(0.02)	0.11	(0.04)	0.07	(0.03)
FeO [(2)]	28.03		19.61	(0.16)	19.63	(0.61)	29.23	(0.94)	24.13	(0.57)
Fe_2O_3 [(2)]	7.80		4.37	(0.47)	5.29	(0.41)	17.96	(2.76)	8.86	(1.21)
Total	100.51		100.90	(0.50)	101.18	(0.15)	99.96	(0.97)	100.63	(0.54)

Sample - Magnetite					14LBM1-21[1]		14LBM1-28[1]		AVERAGE[1]	
Oxide					wt%	n=8	wt%	n=2	wt%	N=2
MgO					0.21	(0.14)	0.47	(0.01)	0.34	(0.08)
Al_2O_3					0.07	(0.06)	0.04	(0.00)	0.05	(0.03)
SiO_2					0.46	(0.23)	0.55	(0.03)	0.50	(0.13)
CaO					0.06	(0.09)	0.00	(0.00)	0.03	(0.05)
TiO_2					0.01	(0.02)	0.04	(0.06)	0.03	(0.04)
Cr_2O_3					0.91	(1.20)	0.68	(0.05)	0.79	(0.63)
MnO					0.09	(0.03)	0.02	(0.02)	0.05	(0.02)
NiO					0.03	(0.04)	0.29	(0.02)	0.16	(0.03)
FeO [(2)]					31.41	(0.32)	30.99	(0.21)	31.20	(0.26)
Fe_2O_3 [(2)]					67.55	(1.29)	67.52	(0.44)	67.54	(0.86)
Total					100.80	(0.31)	100.60	(0.51)	100.69	(0.41)

[1]Uncertainties in parentheses for analyzed quantities are reported to 1σ, unless only one point was taken.

[2]Ferrous and ferric iron wt% calculated by stoichiometry.

Abbreviations: n = number of points taken for the sample. N = number of sample set averages used for calculation.

Table 3.10. Formula proportions of spinels in Lord Brassey samples, based on 4 oxygen atoms.

Sample - Chromite	14LBM1-3[1]		14LBM1-5[1]		14LBM1-21[1]		14LBM1-28[1]		AVERAGE[1]	
Element	wt%	n=1	wt%	n=3	wt%	n=8	wt%	n=9	wt%	N=4
Na	0.000		0.000	(0.001)	0.000	(0.000)	0.003	(0.007)	0.001	(0.007)
Mg	0.155		0.479	(0.005)	0.480	(0.017)	0.116	(0.033)	0.308	(0.038)
Al	0.305		0.782	(0.046)	0.738	(0.029)	0.179	(0.048)	0.501	(0.073)
Si	0.002		0.000	(0.000)	0.000	(0.000)	0.008	(0.020)	0.003	(0.020)
Ca	0.017		0.002	(0.002)	0.000	(0.000)	0.000	(0.000)	0.005	(0.002)
Ti	0.004		0.004	(0.003)	0.004	(0.001)	0.017	(0.007)	0.007	(0.007)
V	0.009		0.004	(0.001)	0.005	(0.000)	0.010	(0.004)	0.007	(0.004)
Cr	1.469		1.103	(0.035)	1.123	(0.027)	1.274	(0.091)	1.242	(0.101)
Mn	0.011		0.007	(0.000)	0.007	(0.001)	0.016	(0.005)	0.010	(0.005)
Fe^{2+}	0.822		0.513	(0.002)	0.515	(0.018)	0.885	(0.030)	0.684	(0.035)
Fe^{3+}	0.206		0.103	(0.012)	0.125	(0.010)	0.489	(0.077)	0.231	(0.079)
Ni	0.000		0.002	(0.001)	0.002	(0.000)	0.003	(0.001)	0.002	(0.001)
Total	3.000		2.999	(0.000)	2.999	(0.000)	3.000	(0.000)	2.999	(0.000)

Sample - Magnetite	14LBM1-21[1]		14LBM1-28[1]		AVERAGE[1]	
Element	wt%	n=8	wt%	n=2	wt%	N=2
Mg	0.012	(0.008)	0.027	(0.001)	0.019	(0.008)
Al	0.003	(0.003)	0.002	(0.000)	0.002	(0.003)
Si	0.017	(0.009)	0.021	(0.001)	0.019	(0.009)
Ca	0.002	(0.004)	0.000	(0.000)	0.001	(0.004)
Ti	0.000	(0.001)	0.001	(0.002)	0.001	(0.002)
Cr	0.027	(0.036)	0.020	(0.002)	0.024	(0.036)
Mn	0.003	(0.001)	0.001	(0.001)	0.002	(0.001)
Fe^{2+}	1.000	(0.010)	0.986	(0.002)	0.993	(0.010)
Fe^{3+}	1.934	(0.041)	1.934	(0.003)	1.934	(0.041)
Ni	0.001	(0.001)	0.009	(0.001)	0.005	(0.002)
Total	2.999	(0.000)	3.001	(0.000)	3.000	(0.000)

[1]Uncertainties in parentheses for analyzed quantities are reported to 1σ, unless only one point was taken. Abbreviations: apfu = atoms per formula unit. n = number of points taken for the sample. N = number of sample set averages used for calculation.

Table 3.11. Electron microprobe analyses of heazlewoodite and awaruite in Lord Brassey samples.

Heazlewoodite	14LBM1-28[1]		14LBM1-31[1]		AVERAGE[1]		Awaruite	14LBM1-31[1]	
Element	wt%	n=44	wt%	n=18	wt%	N=2	Element	wt%	n=28
Mo	0.00	(0.02)	0.01	(0.02)	0.00	(0.02)	Mo	0.00	(0.00)
Si	0.02	(0.04)	0.03	(0.04)	0.02	(0.04)	Si	0.00	(0.01)
Cr	0.00	(0.01)	0.01	(0.01)	0.00	(0.01)	Cr	0.00	(0.00)
Fe	0.20	(0.28)	1.42	(1.04)	0.81	(0.66)	Fe	24.02	(0.50)
Co	0.03	(0.03)	0.14	(0.02)	0.09	(0.03)	Co	0.22	(0.13)
Ni	72.27	(1.14)	71.54	(1.21)	71.90	(1.17)	Ni	73.50	(0.74)
Cu	0.01	(0.02)	0.00	(0.00)	0.00	(0.01)	Cu	0.07	(0.09)
Mn	0.00	(0.00)	0.00	(0.01)	0.00	(0.00)	Mn	0.00	(0.00)
Mg	0.09	(0.10)	0.16	(0.13)	0.12	(0.11)	Mg	0.05	(0.07)
S	26.54	(0.77)	26.16	(0.56)	26.35	(0.67)	S	0.13	(0.11)
As	0.03	(0.03)	0.11	(0.05)	0.07	(0.04)	As	0.02	(0.03)
Total	99.19	(0.59)	99.58	(0.86)	99.36	(0.72)	Total	98.01	(0.44)

Heazlewoodite	14LBM1-28[1]		14LBM1-31[1]		AVERAGE[1]		Awaruite	14LBM1-31[1]	
Element	apfu	n=44	apfu	n=18	apfu	N=2	Element	apfu	n=28
Mo	0.000	(0.000)	0.000	(0.000)	0.000	(0.001)	Mo	0.000	(0.000)
Si	0.002	(0.004)	0.002	(0.003)	0.002	(0.005)	Si	0.000	(0.001)
Cr	0.000	(0.000)	0.000	(0.001)	0.000	(0.001)	Cr	0.000	(0.000)
Fe	0.009	(0.012)	0.062	(0.046)	0.035	(0.048)	Fe	1.015	(0.021)
Co	0.001	(0.001)	0.006	(0.001)	0.004	(0.002)	Co	0.009	(0.005)
Ni	2.976	(0.055)	2.941	(0.030)	2.958	(0.062)	Ni	2.956	(0.029)
Cu	0.000	(0.001)	0.000	(0.000)	0.000	(0.001)	Cu	0.003	(0.003)
Mn	0.000	(0.000)	0.000	(0.000)	0.000	(0.000)	Mn	0.000	(0.000)
Mg	0.009	(0.009)	0.016	(0.013)	0.012	(0.016)	Mg	0.005	(0.007)
S	2.001	(0.050)	1.969	(0.025)	1.985	(0.056)	S	0.010	(0.008)
As	0.000	(0.000)	0.004	(0.002)	0.002	(0.002)	As	0.001	(0.001)
Total	4.998	(0.001)	5.000	(0.001)	4.998	(0.001)	Total	3.999	(0.001)

[1]Uncertainties in parentheses for analyzed quantities are reported to 1σ.
Abbreviations: apfu = atoms per formula unit. n = number of points taken for the sample. N = number of sample set averages used for calculation.

Table 3.12. Electron microprobe analyses and formula proportions of sulfides in Lord Brassey sample 14LBM1-28.

Sulfide	Cobaltpentlandite[1]		Anilite[1]		cadmium sulfide[1]		Molybdenite[1,2]	
Element	wt%	n=31	wt%	n=4	wt%	n=9	wt%	n=1
Mo	0.00	(0.00)	0.00	(0.00)	0.00	(0.00)	52.96	
Si	0.00	(0.00)	0.02	(0.02)	0.00	(0.00)	1.06	
Zn	0.00	(0.00)	0.00	(0.00)	0.76	(0.08)	0.10	
Cd	0.00	(0.01)	0.02	(0.04)	75.41	(0.62)	0.00	
Cr	0.00	(0.01)	0.00	(0.00)	0.00	(0.00)	0.03	
Fe	2.90	(0.17)	0.05	(0.03)	0.02	(0.02)	0.25	
Co	47.79	(0.84)	0.25	(0.27)	0.02	(0.04)	0.06	
Ni	15.97	(0.62)	0.34	(0.19)	1.22	(0.58)	1.37	
Cu	0.25	(0.87)	76.53	(0.54)	0.21	(0.17)	0.06	
Mn	0.00	(0.01)	0.00	(0.00)	0.00	(0.00)	0.00	
Mg	0.02	(0.02)	0.01	(0.02)	0.01	(0.01)	1.64	
S	32.33	(0.16)	22.52	(0.08)	22.12	(0.10)	37.23	
As	0.05	(0.03)	0.00	(0.00)	0.03	(0.04)	0.00	
Ag	0.00	(0.01)	0.00	(0.00)	0.02	(0.04)	0.00	
Total	99.31	(0.51)	99.74	(0.45)	99.82	(1.02)	94.76	

Sulfide	Cobaltpentlandite[1]		Anilite[1]		cadmium sulfide[1]		Molybdenite[1,2]	
Element	apfu	n=31	apfu	n=4	apfu	n=9	apfu	n=1
Mo	0.000	(0.000)	0.000	(0.000)	0.000	(0.000)	0.951	
Si	0.000	(0.001)	0.003	(0.003)	0.000	(0.000)	0.000	
Zn	0.000	(0.001)	0.000	(0.000)	0.017	(0.002)	0.002	
Cd	0.000	(0.001)	0.001	(0.002)	0.959	(0.009)	0.000	
Cr	0.000	(0.001)	0.000	(0.000)	0.000	(0.000)	0.001	
Fe	0.411	(0.024)	0.006	(0.003)	0.000	(0.001)	0.007	
Co	6.413	(0.109)	0.024	(0.026)	0.001	(0.001)	0.002	
Ni	2.152	(0.078)	0.033	(0.019)	0.030	(0.014)	0.040	
Cu	0.031	(0.109)	6.901	(0.034)	0.005	(0.004)	0.001	
Mn	0.000	(0.001)	0.000	(0.000)	0.000	(0.000)	0.000	
Mg	0.007	(0.005)	0.003	(0.003)	0.001	(0.001)	0.000	
S	7.975	(0.021)	4.024	(0.013)	0.986	(0.008)	2.000	
As	0.005	(0.004)	0.000	(0.000)	0.001	(0.001)	0.000	
Ag	0.000	(0.001)	0.000	(0.000)	0.000	(0.001)	0.000	
Total	16.994	(0.004)	10.995	(0.002)	2.000	(0.001)	3.004	

[1]Uncertainties in parentheses for analyzed quantities are reported to 1σ, unless only one point was taken.
[2]Molybdenite stoichiometry was normalized to 2S; poor polish accounts for low analytical total.
Abbreviations: apfu = atoms per formula unit. n = number of points taken for the sample.

Table 3.13. Electron microprobe analyses and formula proportions of trace phases in Lord Brassey samples.

Diopside	14LBM1-5[1]		Jianshuiite	14LBM1-9[1]	
Oxide	wt%	n=19	Oxide	wt%	n=12
SiO_2	53.79	(1.22)	SiO_2	0.17	(0.25)
TiO_2	0.00	(0.01)	TiO_2	0.00	(0.00)
Al_2O_3	0.20	(0.08)	Al_2O_3	0.04	(0.04)
V_2O_3	0.00	(0.00)	V_2O_3	0.00	(0.00)
Cr_2O_3	0.04	(0.05)	Cr_2O_3	0.00	(0.01)
FeO	2.51	(0.41)	Fe_2O_3	0.48	(0.63)
NiO	0.01	(0.02)	NiO	4.84	(2.77)
MnO	0.29	(0.05)	MnO_2	72.43	(3.78)
MgO	17.94	(1.10)	MgO	4.41	(0.34)
CaO	24.77	(0.64)	CaO	0.77	(0.20)
Na_2O	0.01	(0.01)	Na_2O	0.87	(0.12)
K_2O	0.00	(0.00)	K_2O	0.51	(0.23)
O	0.16	(0.09)	O	0.00	(0.00)
H_2O	0.00	(0.00)	H_2O	14.59	(0.29)
Total	99.72	(0.91)	Total	99.11	(1.46)

Diopside	14LBM1-5[1]		Jianshuiite	14LBM1-9[1]	
Element	apfu	n=19	Element	apfu	n=12
Si	1.961	(0.039)	Si	0.011	(0.016)
Ti	0.000	(0.000)	Ti	0.000	(0.000)
Al	0.009	(0.004)	Al	0.003	(0.003)
V	0.000	(0.000)	V	0.000	(0.000)
Cr	0.001	(0.001)	Cr	0.000	(0.000)
Fe	0.076	(0.013)	Fe^{3+}	0.022	(0.030)
Ni	0.000	(0.001)	Ni	0.240	(0.143)
Mn	0.009	(0.002)	Mn^{4+}	3.086	(0.108)
Mg	0.975	(0.057)	Mg	0.406	(0.037)
Ca	0.968	(0.029)	Ca	0.051	(0.012)
Na	0.000	(0.001)	Na	0.103	(0.015)
K	0.000	(0.000)	K	0.040	(0.018)
O	5.987	(0.032)	O	10.000	(0.000)
H	0.000	(0.000)	H	6.000	(0.000)
Total	9.986	(0.032)	Total	19.962	(0.076)

[1]Uncertainties in parentheses for analyzed quantities are reported to 1σ. Abbreviations: apfu = atoms per formula unit. n = number of points taken for the sample.

3.4.3. Methodology Comparison

For each individual sample, the whole rock composition calculated from QXRD and EPMA data was very similar to the measured whole rock composition (Table A.4). Almost all calculated wt% oxide data fall along the one-to-one line, within error of the known values from whole rock analysis (Fig. 3.2). Linear regression results for individual samples all have slopes near the ideal value of 1.0 (Fig. 3.2). Overall, the calculated and measured compositions appear to produce similar values to the individual samples, although it should be noted that this is due to the data being proportions of a whole with a nearly identical constant sum (closed array) (Chayes, 1960; Chayes and Trochimczyk, 1978).

Results are more varied when oxide wt% values are plotted for specific elements (Fig. 3.3, Table A.4). Oxides that fell below the limit of detection for whole rock geochemistry measurements were not included in this analysis (Table A.2). The oxide that most closely followed to one-to-one line was silica, with all others being systematically underestimated or overestimated in our calculated whole rock compositions (Fig. 3.3). LOI_V values were underestimated whereas magnesium oxide content was overestimated in our calculations (Fig. 3.3). Calculated alumina and chromium oxide values were also overestimated but calcium and iron oxide values were consistently underestimated (Fig. 3.3). Most calculated values for nickel abundance were within error of the measured values; however, one outlier was underestimated in our calculations, which caused a strong deviation from the ideal one-to-one trend line (Fig. 3.3). Strong linear correlations were observed for calculated silica, magnesium, aluminum and calcium oxide abundances, which have a positive correlation with measured abundances, whereas iron and, to a lesser extent, chromium oxide abundances have negative correlations with measured values (Fig. 3.3).

Certain wt% oxide values were summed and the resulting calculated and measured values were plotted in Figure 3.4. The sum of iron and chromium oxide abundances (based on their co-occurrence in spinels) produced a positive relationship, instead of the inverse relationships previously observed, and decreased the disparity between the calculated and measured values (Fig. 3.4). The combination of aluminum and calcium (based on their co-occurrence within the observed garnet phases) centered the points and trend line around the one-to-one line, improving the relationship (Fig. 3.4). The combination of iron and magnesium (based on their presence in

serpentine) produced a positive relationship and brought the points closer to the one-to-one line, although there remained a systematic underestimate for most of the calculated values (Fig. 3.4).

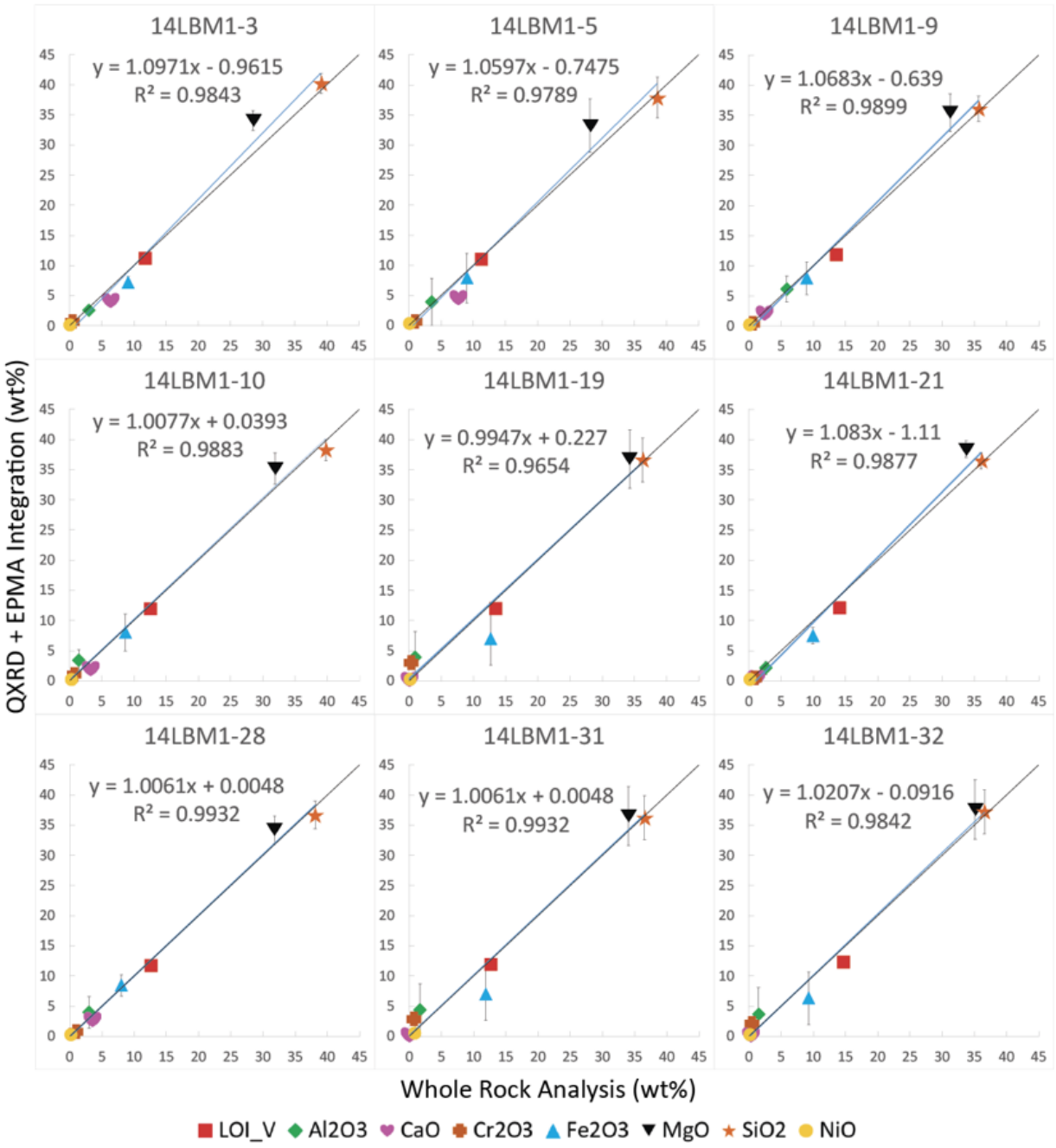

Fig. 3.2. Comparison plots of the various oxide wt% values for each individual sample, from the integration of QXRD and EPMA data (calculated data) and the whole rock analysis (measured data). Total iron is presented as Fe_2O_3. R^2 is the coefficient of determination, which in this case signifies what percentage of data variance from the methods integration is explainable from the whole rock analysis (Miles, 2005). LOI_V was measured following heating to 1000 °C and accounting for mass gain due to oxidation of ferrous iron (Lechler and Desilets, 1987).

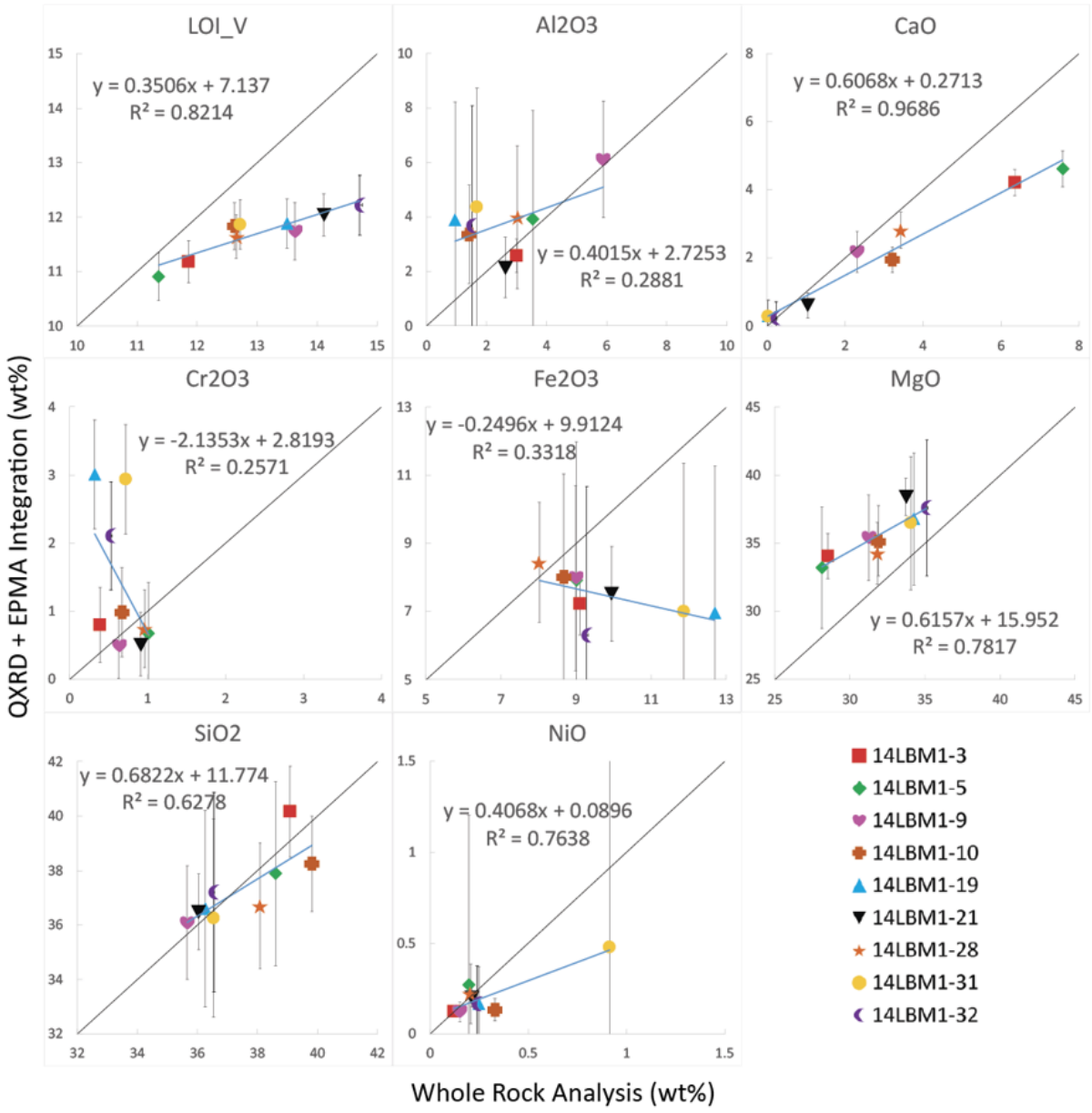

Fig. 3.3. Comparison plots for the individual oxide wt% values for all samples from the integration of QXRD and EPMA data (calculated data) and whole rock analysis (measured data). Total iron is presented as Fe_2O_3. R^2 is the coefficient of determination, which in this circumstance signifies what percentage of data variance from the methods integration is explainable from the whole rock analysis (Miles, 2005). Error bars reflect total propagated uncertainties (including methodological uncertainties and compositional heterogeneities) from both QXRD and EPMA.

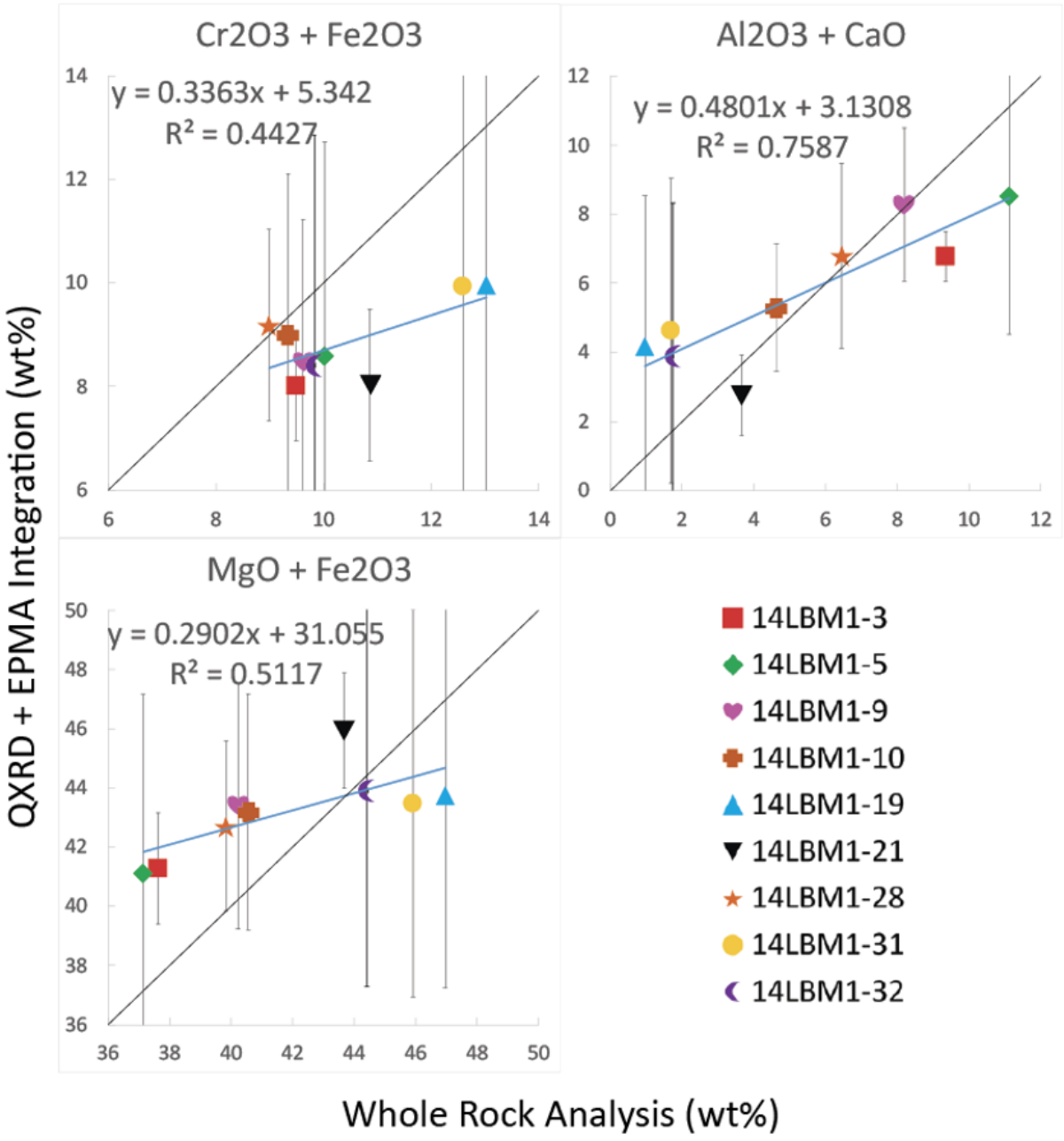

Fig. 3.4. Comparison plots for summed wt% values for select oxides for all samples, from the integration of QXRD and EPMA data (calculated data) and whole rock analysis (measured data). Total iron is presented as Fe_2O_3. R^2 is the coefficient of determination, which in this circumstance signifies what percentage of data variance from the methods integration is explainable from the whole rock analysis (Miles, 2005).

3.5. Discussion

3.5.1. Transition Metal Sources

Aligning with its ultramafic origin, the samples are dominated by groundmass serpentine (mostly lizardite with minor antigorite) intergrown with lesser amounts of chlorite [clinochlore, distinguished empirically from serpentine by its higher aluminum content (Gillery, 1959)] (Tables 3.1, 3.2, 3.4). Clinochlore possesses slightly higher concentrations of iron and chromium (still below 6 and 1 wt% oxide, respectively) than the serpentine, but both contain low amounts of nickel at ~0.15 wt% oxide on average (Tables 3.2, 3.3, 3.4, 3.5). The garnets, which were present in all analyzed samples, were mainly andradite with minor grossular (Table 3.8), both previously observed at Lord Brassey (Anderson et al. 2002). Nickel was not included in the EPMA measurements for garnets due to the anticipated low content. This was supported by its absence in SEM-EDS data and synchrotron XFM analysis of the garnets (Chapter 2). All other critical transition metals, excluding chromium, individually fell below 1.0 wt% abundance on average (Tables 3.6, 3.7, 3.8). The serpentine observed in the samples contain low nickel oxide wt% (Tables 3.2) but has an average whole rock mineral abundance of ~87% (Table 3.1). Due to its abundance within the samples, serpentine contains total nickel oxide wt% comparable to heazlewoodite and awaruite (Table A.4) and in samples that are devoid of heazlewoodite and awaruite, serpentine is the dominant nickel host (Fig. 3.3, Table A.4).

Spinel minerals were observed in every sample through SEM-EDS, and determined via QXRD and SEM-EDS to be mostly chromite with some magnetite (Table 3.1). Chromite is common throughout the Heazlewood Complex as an accessory mineral to serpentinization, occasionally rimmed or crosscut by magnetite (Peck and Keays, 1990; Anderson et al., 2002). EPMA results reveal the magnetite to be almost entirely pure iron oxide (>98 wt%) with traces of chromium, manganese and nickel oxide (summed to ~1 wt% total) (Table 3.9). The chromite was found to consist of ~47 wt% chromium oxide on average with lesser amounts of iron oxide (33 wt%) and aluminum oxide (13 wt%) (Table 3.9, 3.10).

While a number of sulfide and alloy grains were distinctly visible in some samples via SEM-EDS, and confirmed with EPMA, the most intense QXRD peaks of these phases were indistinguishable from background noise for a subset of these samples (Tables 3.1, 3.11, 3.12).

Sulfide mineral species and the alloy mineral, awaruite, were identified with EPMA in samples where they were detectable using QXRD. Heazlewoodite was the most common sulfide mineral, which contained on average 72 wt% nickel and 26.4 wt% sulfur (Table 3.11). The awaruite, which is commonly associated with heazlewoodite, was determined on average to contain roughly 74 wt% nickel and 24 wt% iron (Table 3.11). These nickel-bearing phases were present at a maximum abundance of 0.2 wt% when detected via QXRD (Table 3.1). Of the other sulfides identified with EPMA, only molybdenite was historically reported from Lord Brassey (Anderson et al., 2002). Although previous reports have described pentlandite [$(Fe,Ni)_9S_8$] at this locality (Anderson et al., 2002), our EPMA results revealed it to be entirely cobaltpentlandite, denoted by its high cobalt content (~48 wt% cobalt on average paired with ~16 wt% of nickel) (Table 3.12). The molybdenite contained ~53 wt% molybdenum, the anilite contained ~77 wt% copper and the grenockite/hawleyite polymorph(s) contained ~75 wt% cadmium, although, none of these sulfide minerals were detectable via QXRD.

Both of the remaining trace phases, though varied in their composition, pose little significance in being recoverable sources of transition metals. The trace pyroxene phase, identified as diopside, hosted very low amounts of critical transition metals (<1 wt%) akin to the groundmass minerals and garnets (Table 3.13). Unlike those phases, however, pyroxene is rarely observed in the samples (2 wt% in one sample) and therefore should be overlooked as a source of any significant resources at Lord Brassey. The mineral, jianshuiite, was identified with EPMA and detectable in one sample via QXRD (Table 3.1). This phase has not previously been reported from Lord Brassey, likely because it is a trace phase only observable via SEM-EDS/EPMA and owing to its relatively recent characterization (Guiyin et al., 1992). Despite a hearty manganese oxide component (>72 oxide wt%), due to its scant abundance within the samples (detectable by QXRD in a single sample at roughly 0.2 wt%) this mineral phase should not be sought out as a minable source for manganese in this deposit (Tables 3.1, 3.13).

3.5.2. Methodology Comparison & Practicality

Calculated oxide wt% values for the samples were comparable in most regards with the measured values from whole rock analysis. On a sample-by-sample basis, both methods produced similar outputs corroborated by the trend lines falling near the one-to-one line (Fig. 3.2). However,

as the data are a closed-array (consisting of proportional data that sum to nearly 100%), other measures of accuracy must also be used. Closed arrays of data are characterized by strong negative correlations between major constituents, so as some variables change others will compensate to reach the expected total sum of 100% (Chayes, 1960; Chayes and Trochimczyk, 1978). The coefficients of determination from these data, while close to the ideal value of 1, tell us little about the disparities between the calculated and measured elemental compositions. The comparison of specific oxide wt% values across all samples is where the disparities become apparent (Fig. 3.3).

The diffraction peaks for chromite and magnetite overlap significantly and therefore it is important to confirm which spinels are present through a second technique such as EPMA or SEM-EDS before including them in a Rietveld refinement. Only chromite was accounted for in the QXRD for samples 14LBM1-19 and 14LBM1-31 (Table 3.1), although it was likely they contained magnetite as well. This suspicion is confirmed in the oxide wt% comparison plots (Fig. 3.3) as the calculated values indicate much higher chromium oxide wt% and lower iron oxide wt% values than the measured values from the industry-standard whole rock analysis. When the values for chromium and iron oxide wt% were summed on a per sample basis, a more favorable trend was observed (Fig. 3.4). The aforementioned outliers in the analysis are data for samples where magnetite was not included in Rietveld refinements. It is possible that including magnetite in all of the refinements from which it was missing would produce a more favorable output, but that level of sensitivity is beyond the scope of this study. Partitioning of intensity under Bragg peaks between two members of a solid solution can be challenging, particularly when peak overlap is as strong as for magnetite and chromite. Because these minerals contain much of the iron and chromium in the samples, this presents an important source of error in our analysis. The use of quantitative SEM, EPMA or XRF mapping may be a better way to account for chromium and iron wt% abundances in spinel-rich samples.

The aluminum oxide and calcium oxide wt% plots (Fig. 3.3) show that calculated values systematically overestimate and underestimate these abundances, respectively. When these oxide wt% values are summed to account for the aluminum and calcium content in grossular garnets (whose presence is confirmed via EPMA) they are underestimated at lower wt% values and overestimated at greater values (Table 3.8, Fig. 3.4). We can see that samples with higher amounts of garnets will have higher amounts of calcium and aluminum in the whole rock analysis, and vice

versa, which highlights the variability of the samples (Table 3.1, Fig. 3.4). Our garnet results also reveal an inconsistency in how the data are most likely to be interpreted, as the QXRD results suggest that grossular garnet is present in only a couple of samples (Table 3.1) but the EPMA results indicate grossular is found in most samples (Table 3.8). As well, some of our EPMA analyses describe garnets containing no grossular, such is the case for sample 14LBM1-28, whereas QXRD results report the presence of grossular garnet. EPMA data for garnets revealed that they are solid solutions of many different garnet minerals rather than a pure garnet species (Table 3.8). Therefore, as with the spinel issue mentioned prior, it would be wise to carry out an EPMA analysis first, supplemented by SEM-EDS, and then perform a QXRD analysis, to better account for different species in the same mineral group that have overlapping diffraction peaks.

Summing the magnesium and iron oxide wt% values, based on their co-occurrence and complete substitution in many minerals, produced a comparison plot that reduced both the overestimation of magnesium abundance and underestimation of iron abundance in the calculated results (Fig. 3.4). The numerical disparity between methods was decreased and outliers on the individual magnesium and iron oxide wt% plots were reduced in severity, indicating greater accuracy when summing magnesium and iron oxide wt% data compared to individual use. The LOI_V content is higher for the measured whole rock analysis than for the calculated wt% oxide values in all samples, which is due to a difference in how this variable was defined. The measured LOI_V values for the whole rock analysis account for all volatile loss, including structural H_2O, carbonate, sulfur, hydroxyls and chlorine, whereas the calculated LOI_V results only account for H_2O content. Although the additional volatile phases are present at lower abundances in these samples, it is enough to make an impact on the final values as the calculated values for LOI_V abundance are underestimated (Fig 3.3).

The measured and calculated values for nickel oxide wt% were comparable across all samples except for 14LBM1-31, which contains awaruite and heazlewoodite at abundances that are detectable and quantifiable using QXRD (Table 3.1, Fig. 3.3). Sample 14LBM1-31 also contains the highest measured Ni abundance of all analyzed samples, at 0.72 wt% with the second highest (14LBM1-10) being 0.26 wt% (Table A.2). However, the propagated error for the calculated value of nickel oxide abundance in 14LBM1-31 still falls along the one-to-one line. As all the nickel-bearing phases in this sample were analyzed with EPMA, and included in the data

integration with QXRD, the underestimation of calculated nickel abundance in this sole sample may be due to a sampling error or attributed to the greater relative error on refined abundances of trace phases using QXRD (e.g., Wilson et al., 2006).

A number of the discrepancies between the calculated and measured oxide wt% values can be traced back to differences in observations made using bulk XRD data and using spatially-resolved EPMA data, as previously noted. The use of EPMA data with Rietveld refinement results provides more accurate wt% oxide calculations than assuming stoichiometric mineral compositions. Mineral identification and characterization needs to be done carefully and iteratively using EPMA, SEM-EDS and QXRD results.

Some of the possible pitfalls of using QXRD results alone to calculate the elemental composition of rocks include choosing a compositionally inaccurate mineral within a solid solution or missing diffraction peaks present near the limit of detection for XRD (3σ above background). The first pitfall is well illustrated by the prior discussion of how best to quantify the abundances of magnetite and chromite. The second occurs when the most intense diffraction peaks of a mineral are at the detection limit of XRD so that it is hard to justify including the phase in a Rietveld refinement model. Even if the phase in question is confirmed to be present via other methods, it will not be accounted for in the final calculated output due to its abundance falling below the limit of detection of XRD but not EPMA.

A specific example of how low abundance minerals can affect calculated wt% abundances comes from sample 14LBM1-28, which contains visible sulfide minerals, but no sulfides were detectable from XRD patterns collected on a representative powdered subsample. Cobaltpentlandite contains roughly 477,900 ppm of cobalt based on EPMA data for this sample (Table 3.12). If cobaltpentlandite is considered the sole host of cobalt in this sample, which contains 93.8 ppm of Co (from the industry whole rock analysis, Table A.2) the sample should contain roughly 0.02 wt% cobaltpentlandite. This is an order of magnitude below the detection limit of most minerals for XRD data collected in our laboratory (i.e., ~0.1 wt%). Special care must be taken to ensure the powdered sample for QXRD and the thin section for EPMA are similarly representative of the deposit or inconsistencies will arise. If mineral phases go unobserved using

one technique, their exclusion could shift the final results considerably, particularly for critical transition metals when they are concentrated in minerals present at trace abundance (<1 wt%).

Another possible reason for the difference in outcomes is the lack of EPMA data for some samples. Once a sufficient number of samples and phases have been analyzed via EPMA, it is possible to use averages and errors added in quadrature to accurately predict the compositions of the remaining samples and deposit as a whole. Samples 14LBM1-19 and 14LBM1-32 had no EPMA points taken; instead average values for the other samples were used for integration with their QXRD results, which still produced calculated oxide wt% values similar to the industry whole rock analysis (Figs. 3.2, 3.3, Table A.4).

Despite these limitations, the measurements from the data integration are consistent with those from the whole rock analysis (Figs. 3.3, 3.4), and with more refinements and reassessments the results could be improved further should the user desire it. Overall, the combined use of QXRD and EPMA can provide an accurate calculated whole rock analysis that is comparable with industry standard whole rock data, while also supplementing that with mineral abundances and compositions. Thus, we propose that the integrated use of QXRD and EPMA, in addition to measured whole rock analysis, can be used as an accurate geometallurgical tool to aid in ore deposit characterization (including tailings deposits) and resource recovery.

In the future, the incorporation of a quantitative mineral mapping technique such as QEMSCAN (Quantitative Evaluation of Minerals by Scanning Electron Microscopy)/Mineral Liberation Analysis (MLA) or μXRF (micro X-ray Fluorescence) (e.g., Barker et al., 2021) could be used to provide improved quantification of trace minerals, as well as information about grain size, mineral associations and mineral liberation. QEMSCAN/MLA can also be used to characterize and quantify amorphous and nanocrystalline phases, such as zaratite and ferrihydrite, which are known to host nickel and cobalt respectively at Lord Brassey (Chapter 2). The presence of such phases, which are difficult to detect using QXRD (Ayling et al., 2012), may be another source of analytical error in our calculations. Conversely, QXRD can be used to characterize polymorphs whereas QEMSCAN/MLA cannot. Quantitative SEM and μXRF techniques are limited to 2D space and are dependent on what is visible in the provided exposure, which is a less effective way to assess the bulk composition of a sample. Quantitative SEM and μXRF mapping

techniques provide an incomplete description of stoichiometric data; thus they are not substitutes for either EPMA or QXRD, and should instead be considered supplementary analytical techniques when available.

3.5.3. Implications For Tailings Processing & Metal Recovery

Heazlewoodite, awaruite and serpentine are the primary nickel sources in the Lord Brassey tailings. Heazlewoodite and awaruite contain the highest concentrations of nickel within the present mineral phases but they are only detectable using XRD in a small number of samples (Tables 3.1, 3.11). Serpentine contains trace concentrations of nickel but due to its high abundance within the samples, it contains comparable total nickel oxide wt% to the aforementioned mineral phases (Tables 3.1, 3.2, A.4). Cobaltpentlandite is the primary host for cobalt, but it was not detectable using XRD owing to its relatively low overall abundance. Chromite is the primary host of chromium and present in all samples; however, quantification of chromite abundance using QXRD can be challenging for samples that contain other spinels, such as magnetite, that produce overlapping diffraction peaks. All other critical transition metals and higher concentration mineral phases were either not measured via EPMA or undetectable via QXRD due to their minute abundance, so an accurate ore grade could not be generated from the QXRD and EPMA data on their own. The whole rock analysis provides the most reliable estimate of nickel, cobalt and chromium grades (Table A.2).

For the nickel content, one sample (14LBM1-31) measured 0.72 wt% (Table A.2), which qualifies it as low-grade nickel ore, which is increasingly being mined due to high demand for this resource (EMEW Clean Technologies, 2017). The nickel in this sample is found primarily in heazlewoodite, awaruite and serpentine, meaning that magnetic/gravimetric processes would be needed to recover awaruite in addition to the use of heap leaching or froth flotation for sulfide minerals and serpentine (Lindsay et al., 2015; Alcalde et al., 2018; Hamilton et al., 2018). As there are trace amounts (<1 wt%) of measureable nickel within most mineral phases present, especially the host serpentine, the artificial nickel laterite process proposed by Hamilton et al. (2020) could be used to concentrate nickel from all mineral phases into ferrihydrite for recovery. Additionally, the sulfidation-carbonation method developed by Wang et al., (2021), which uses a steady supply of gas (95% CO_2 and 5% hydrogen sulfide [H_2S]) to accelerate mineral carbonation and the

sulfidation of nickel liberated from olivine/serpentine (which can then be recovered), is another process worth exploring. The average reported whole rock concentration of cobalt is approximately 0.01 wt% qualifying it as low-grade and economic cobalt ore (Slack et al., 2017). The primary host for cobalt is cobaltpentlandite, which as a sulfide mineral, can be recovered using the same processes as heazlewoodite. Chromium oxide has a maximum value of 1.01 wt% in the Lord Brassey samples, which is too low to be considered even refractory grade ore (i.e., >30 wt%) (Mosier et al., 2012).

The tailings facility at Lord Brassey is much too small to be used as a resource for nickel or cobalt recovery. It is not economically feasible to mine the low grades of nickel (<1 wt%) and cobalt (0.01 wt%, the lowest possible grade to qualify as ore) from the small mass of the workings at this site. However, large-scale mining operations with similar geology (such as the Avebury mine, Keays and Jowitt, 2013) could use the knowledge generated here for reprocessing and management of serpentinite skarn tailings. The tailings at the Lord Brassey Mine have been left to weather for more than 100 years. Globally, ~420 Mt of ultramafic tailings (akin to the Lord Brassey tailings), are produced annually and many gigatonnes of ultramafic tailings have been stockpiled, and left to weather, at operating and closed mines (Sandalow et al., 2021). These mine tailings likely contain a vast supply of critical metals such as nickel and cobalt, but the size of the critical metal resource in tailings is very poorly constrained. Furthermore, little is known about how the geometallurgy of tailings changes as a function of time and weathering.

The quantitative geometallurgical tools developed as part of this study and in Chapter 2 provide a framework for assessing where nickel, cobalt and other valuable metals are found in tailings and how ore mineralogy changes over the mining lifecycle. Finally, weathering of ultramafic mine tailings also removes carbon dioxide from the atmosphere, storing it within newly formed carbonate minerals. Accelerated weathering and carbonation reactions can be used as an ore processing technique to recover low-grade nickel and cobalt from ultramafic ore and tailings (Hamilton et al., 2020; Wang et al., 2021). A mineralogical and geometallurgical understanding of the interplay between reactions that recover nickel and cobalt, while binding CO_2 in carbonate minerals will be important for the implementation of such technologies.

3.6. Conclusions

The integration of QXRD with EPMA data provides accurate calculated whole rock elemental compositions that are comparable to measured values obtained using an industry standard method (LOI_V, XRF, ICP-MS, ICP-OES). The results demonstrate that QXRD and EPMA results can accurately reflect the elemental composition of tailings and ore while also providing geometallurgical context about mineral abundances and compositions. The methodology developed here may be used to assess the grades of valuable metals in geological samples, including mine tailings. Fine-tuning of the QXRD results using SEM-EDS and EPMA data was shown to improve the accuracy of the calculated oxide wt% values. Justifying the integration of QXRD and EPMA as an appropriate technique for the appraisal of tailings, for economic value and resource recovery, improves our ability to assess tailings and lends to our growing credibility as mine tailings being a legitimate source for critical metals. Tailings storage facilities, such as the one at the Lord Brassey mine, host economic ore that is waiting to be recovered. In the future, the targeted investigation of weathering products, including alteration minerals and leachates, should be prioritized to understand which minerals play host to valuable metals at the "end" of the mining lifecycle, with the goal of cultivating a framework for economically viable reprocessing of tailings. The more we understand critical transition metal distribution and partitioning within mining waste, the closer we get to a greener, cleaner future where tailings storage facilities are viewed as part of the ore processing circuit.

3.7. Acknowledgements

Funding was provided by grants from the Natural Sciences and Engineering Research Council of Canada (NSERC) Discovery Grants program, the Natural Resources Canada Clean Growth Program and the Canada Research Chairs Program to Dr. Sasha Wilson. Thanks to Mark Labbe and Walter Harley at the U of A thin section lab for thin section construction, and thanks to Dr. Nathan Gerein and Guibin Ma for their extreme patience and guidance with the SEM. Thank you to Rebecca Funk for the XRD analysis and thanks to SGS Minerals for the whole rock analysis.

CHAPTER 4 - CONCLUSIONS & RECOMMENDATIONS

4.1. Key Findings

Valuable critical metals are present in both the Lord Brassey and Record Ridge samples, and their behavior during weathering is predictable based on our results. Coarse-grained sulfide minerals contain the largest concentration and variety of transition metals (e.g., nickel, cobalt, copper, cadmium) which they retain unless oxidized. Oxide minerals and alloys (hosting nickel and cobalt) will resist weathering allowing for their targeted recovery from weathered tailings. Brucite-bearing ultramafic rocks will have nickel sorb to iron oxyhydroxide minerals, whereas in brucite-poor ultramafic rocks, nickel will leach out to be sequestered by weathering-derived carbonates and cobalt will sorb to iron oxyhydroxides instead. Bedrock carbonate minerals observed at Record Ridge are devoid of critical transition metals and should be overlooked for recovery in this locality. The finals sinks for critical transition metals change over the life of a mine as a result of the weathering process. Ultimately, carbonates, iron oxyhydroxides, and the resistant oxides and alloys, should be targeted for recovery of nickel and cobalt from ultramafic mine tailings.

The Lord Brassey samples can be characterized as both low-grade nickel ore and low-grade cobalt ore. Nickel is hosted primarily in heazlewoodite, awaruite and the host serpentine, while cobalt was found in cobaltpentlandite. Integrating QXRD and EPMA results produced calculated whole rock elemental abundances that accurately reflect measured results from industry XRF, ICP-MS and ICP-OES analyses, while also providing mineralogical abundances and compositions. Further refinements of the QXRD data will only improve this accuracy. This analytical tool has worldwide applicability to ultramafic tailings and deposits as only hand samples are needed for an analysis, and further additions such as quantitative SEM or automated XRD for a speedier analysis will further polish this practice. While the reprocessing of Lord Brassey tailings is not justifiable due to the minuteness of the site making startup uneconomic, this information can be applied to ultramafic tailings and deposits worldwide. Inducing the breakdown of the serpentine and sulfides to concentrate critical transition metals into alteration minerals via acid leaching, which will spare the oxide and alloy minerals, is the ideal recovery method to employ at this time due to the varied distribution of nickel in most minerals within the rock.

4.2. Future Work

Based on the results of this research, a number of areas regarding critical transition metal partitioning and recovery from ultramafic deposits and tailings should be further investigated:

- The mineral phases of the Record Ridge samples should be analyzed via EPMA and then integrated with the Record Ridge QXRD data (Table. A.1) in the same fashion as the Lord Brassey samples were in Chapter 3. These two datasets should then be compared to quantitatively display the changes critical transition metals and their sinks experience across the mining lifecycle.

- The carbonate and iron oxyhydroxide minerals from both sample sets should be quantitatively analyzed for their elemental abundances using EPMA. The alteration minerals in this study were not analyzed consistently or thoroughly due to time constraints and the difficulty of quantifying their abundance using QXRD, so a more fleshed out appraisal in needed.

- Performing quantitative SEM (such as QEMSCAN) should be undertaken to supplement the qualitative information on the mineral phase relationships and be integrated into our quantitative analysis. QEMSCAN will also allow the identification of amorphous phases, which was a thorn in this research.

- Forcing the breakdown of the serpentine and chlorite via acid leaching and inducing alteration mineral formation via column experiments will allow a greater understanding and visualization of the pathways the hosted critical transition metals experience within both of these sample sets and additionally assess the potential of acid mine drainage.

REFERENCES

Adiansyah, J. S., Rosano, M., Vink, S., and Keir, G., 2015, A framework for a sustainable approach to mine tailings management: Disposal strategies: Journal of Cleaner Production, v. 108, p. 1050–1062.

Alcalde, J., Kelm, U., and Vergara, D., 2018, Historical assessment of metal recovery potential from old mine tailings: A study case for porphyry copper tailings, Chile: Minerals Engineering, v. 127, p. 334–338.

Anderson, P., Bottrill, R., and Davidson, P., 2002, Famous mineral localities: The Lord Brassey mine, Tasmania: The Mineralogical Record, v. 33, p. 321-332.

AngloAmerican, 2022, What is an assay?, (https://www.angloamerican.com/futuresmart/stories/our-industry/mining-explained/mining-terms-explained-a-to-z/assay-definition)

Armstrong, J.T., 1988, Quantitative analysis of silicate and oxide materials: Comparison of Monte Carlo, ZAF and φ(ρz) procedures: Microbeam Analysis, v. 23, p. 239-246.

Australian Government, Bureau of Meteorology, 2021, Climate Statistics for Australian locations, (http://www.bom.gov.au/climate/averages/tables/cw_097047.shtml)

Australian Government, Geoscience Australia, 2022, Critical Metals, (https://www.ga.gov.au/about/projects/resources/critical-minerals)

Ayling, B., Rose, P., Petty, S., Zemach, E., and Drakos, P., 2012, QEMSCAN® (Quantitative Evaluation of Minerals by Scanning Electron Microscopy): Capability and applications to fracture characterization in geothermal systems: Workshop on Geothermal Reservoir Engineering, 37th, Stanford, California, 2012, 11 p.

Bacon, W. G., Dalvi, A. D., Rochon, B. A., and Selby, M, 2002, Nickel outlook--2000 to 2010: CIM Bulletin, v. 95, p. 47-52.

Baker, E., Davies, M., Fourie, A., Mudd, G., and Thygesen, K, 2020, Chapter II Mine tailings facilities: Overview and industry trends: Towards zero harm – A compendium of papers prepared for the Global Tailings Review, p. 14-24.

Barker, R. D., Barker, S. L. L., Cracknell, M. J., Stock, E. D., and Holmes, G., 2021, Quantitative mineral mapping of drill core surfaces II: Long-wave infrared mineral characterization using μXRF and machine learning: Economic Geology, v. 116, p. 821–836.

Berg, G. W., 1989, The significance of brucite in South African kimberlites, in Ross, J., ed., Kimberlite and related rocks volume 2: Their mantle/crust setting, diamonds and diamond exploration, Geological Society of Australia Special Publication 14: Victoria, Blackwell Scientific, p. 282–296.

Bigham, J. M., and Nordstrom, D. K., 2000, Iron and aluminum hydroxysulfates from acid sulfate waters: Reviews in Mineralogy and Geochemistry, v. 40, p. 351–403.

Bird, J. M., and Weathers, M. S., 1979, Origin of josephinite: Geochemical Journal, v. 13, p. 41–55.

Bish, D. L., and Howard, S. A., 1988, Quantitative phase analysis using the Rietveld method. Journal of Applied Crystallography, v. 21, p. 86–91.

Brindley, G. W., 1945, The effect of grain or particle size on X-ray reflections from mixed powders and alloys, considered in relation to the quantitative determination of crystalline substances by X-ray methods: Philosophy Magazine, v. 36, p. 347-369.

Britannica, 2021, Prospecting and exploration, (https://www.britannica.com/technology/mining/Prospecting-and-exploration)

Britten, R., 2017, Regional metallogeny and genesis of a new deposit type-disseminated awaruite (Ni_3Fe) mineralization hosted in the Cache Creek terrane: Economic Geology, v. 112, p. 517–550.

Bystrov, S. G., Reshetnikov, S. M., Kolotov, A. A., Drozdov, A. Y., and Bayankin, V. Y., 2021, Effect of oxygen ion implantation on physicochemical structure and corrosion-electrochemical behavior of high-chromium steel: Inorganic Materials: Applied Research, v. 12, p. 625–632.

Chang, Y., Zhao, K., and Pešić, B., 2016, Selective leaching of nickel from prereduced limonitic beckerite under moderate HPAL conditions- part I: Dissolution: Journal of Mining and Metallurgy, Section B: Metallurgy, v. 52, p. 127-134.

Chayes, F., 1960, On correlation between variables of constant sum: Journal of Geophysical Research, v. 65, p. 4185-4193.

Chayes, F., and Trochimczyk, J., 1978, An effect of closure on the structure of principal components: Journal of the International Association for Mathematical Geology, v. 10, p. 323–333.

Cheary, R. W., and Coelho, A. A., 1998, Axial divergence in a conventional X-ray powder diffractometer. II. Realization and evaluation in a fundamental-parameter profile fitting procedure: Journal of Applied Crystallography, v. 31, p. 862–868.

Climate-Data, 2021, Rossland climate: Average temperature, weather by month, Rossland weather averages, (https://en.climate-data.org/north-america/canada/british-columbia/rossland-11579/)

Das, S., and Hendry, M. J., 2011, Application of Raman spectroscopy to identify iron minerals commonly found in mine wastes: Chemical Geology, v. 290, p. 101–108.

Dick, H. J. B., 1974, Terrestrial nickel-iron from the Josephine Peridotite, its geologic occurrence, associations, and origin: Earth and Planetary Science Letters, v. 24, p. 291–298.

Dollase, W., 1986, Correction of intensities for preferred orientation in powder diffractometry: Application of the March model: Journal of Applied Crystallography, v. 19(4), p. 267–272.

Donovan, J.J., Snyder, D.A., and Rivers, M.L., 1993, An improved interference correction for trace element analysis: Microbeam Analysis, v. 2, p. 23-28.

Donovan, J. J., Lowers, H. A., and Rusk, B. G., 2011, Improved electron probe microanalysis of trace elements in quartz: American Mineralogist, v. 96, p. 274–282.

Donovan, J.J., Kremser, D., Fournelle, J.H., and Goemann, K., 2015, Probe for EPMA: Acquisition, automation and analysis, (https://www.probesoftware.com/)

EMEW Clean Technologies, 2017, Enhanced methods for nickel recovery from low-grade ores and bleed streams, (https://blog.emew.com/enhanced-methods-for-nickel-recovery-from-low-grade-ores-and-bleed-streams)

Escuder-Viruete, J., Andjić, G., Baumgartner-Mora, C., Baumgartner, P. O., Castillo-Carrión, M., and Gabites, J., 2019, Origin and geodynamic significance of the Siuna Serpentinite Mélange, Northeast Nicaragua: Insights from the large-scale structure, petrology and geochemistry of the ultramafic blocks: Lithos, v. 340–341, p. 1–19.

Figueiredo, J., Cristina Vila, M., Fiúza, A., Góis, J., Futuro, A., Lurdes Dinis, M., and Martins, D., 2019a, A holistic approach in re-mining old tailings deposits for the supply of critical-metals: A Portuguese case study: Minerals, v. 9, p. 638.

Figueiredo, J., Vila, M. C., Góis, J., Biju, B. P., Futuro, A., Martins, D., Dinis, M. L., and Fiúza, A., 2019b, Bi-level depth assessment of an abandoned tailings dam aiming its reprocessing for recovery of valuable metals: Minerals Engineering, v. 133, p. 1–9.

Filippidis, A., 1985, Formation of awaruite in the system Ni-Fe-Mg-Si-O-H-S and olivine hydration with NaOH solution, an experimental study.: Economic Geology, v. 80, p. 1974–1980.

Frost, R. L., Dickfos, M. J., and Jagannadha Reddy, B., 2008, Raman spectroscopy of hydroxy nickel carbonate minerals nullaginite and zaratite: Journal of Raman Spectroscpoy, v. 39, p. 1250-1256.

Fuerstenau, M. C., Jameson, G. J., and Yoon, R. H., 2007, Froth flotation : a century of innovation: Society for Mining, Metallurgy, and Exploration, p. 891.

Garcia-Guinea, J., La Iglesia, A., Crespo-Feo, E., González Del Tánago, J., and Correcher, V., 2013, The status of zaratite: investigation of the type specimen from Cape Ortegal, Galicia, Spain: European Journal of Mineralogy, v. 25, p. 995–1004.

Giaramita, M. J., and Day, H. W., 1990, Error propagation in calculations of structural formulas: American Mineralogist, v. 75, p. 170–182.

Gillery, F. H., 1959, The X-ray study of synthetic Mg-Al serpentines and chlorites: American Mineralogist, v. 44, p. 143-152.

Government of Canada, 2021, Critical metals, (https://www.nrcan.gc.ca/our-natural-resources/minerals-mining/critical-minerals/23414)

Grguric, B. A., Rosengren, N. M., Fletcher, C. M., and Hronsky, J. M. A., 2006, Type 2 deposits: Geology, mineralogy and processing of the Mount Keith and Yakabindie Orebodies, Western Australia: Society of Economic Geologists, Special Publication, v. 13, p. 119–138.

Guiyin, Y., Shanghua, Z., Mingkai, Z., Jinaping, D., and Deyu, L., 1992, Jianshuiite; a new magnesic mineral of the chalcophanite group: Acta Mineralogica Sinica, v. 12, p. 69-77.

Hamilton, J. L., Wilson, S. A., Morgan, B., Turvey, C. C., Paterson, D. J., MacRae, C., McCutcheon, J., and Southam, G., 2016, Nesquehonite sequesters transition metals and CO2 during accelerated carbon mineralisation: International Journal of Greenhouse Gas Control, v. 55, p. 73–81.

Hamilton, J. L., Wilson, S. A., Morgan, B., Turvey, C. C., Paterson, D. J., Jowitt, S. M., McCutcheon, J., and Southam, G., 2018, Fate of transition metals during passive carbonation of ultramafic mine tailings via air capture with potential for metal resource recovery: International Journal of Greenhouse Gas Control, v. 71, p. 155–167.

Hamilton, J. L., Wilson, S. A., Morgan, B., Harrison, A. L., Turvey, C. C., Paterson, D. J., Dipple, G. M., and Southam, G., 2020, Accelerating mineral carbonation in ultramafic mine tailings via direct CO2 reaction and heap leaching with potential for base metal enrichment and recovery: Economic Geology, v. 115, p. 303–323.

Hazen, R. M., 1976, Effects of temperature and pressure on the crystal structure of forsterite: American Mineralogist, v. 61, p. 1280–1293.

Hill, R. J., and Howard, C. J., 1987, Quantitative phase analysis from neutron powder diffraction data using the Rietveld method. Journal of Applied Crystallography, v. 20, p. 467–474.

Himmelberg, G.R. and Loney, R.A., 1995. Characteristics and petrogenesis of Alaskan-type ultramafic-mafic intrusions, southeastern Alaska. USGS Prof. Paper 1564, 47 p.

Kandji, E. H. B., Plante, B., Bussière, B., Beaudoin, G., and Dupont, P. P., 2017, Kinetic testing to evaluate the mineral carbonation and metal leaching potential of ultramafic tailings: Case study of the Dumont Nickel Project, Amos, Québec: Applied Geochemistry, v. 84, p. 262–276.

Keays, R. R., and Jowitt, S. M., 2013, The Avebury Ni deposit, Tasmania: A case study of an unconventional nickel deposit: Ore Geology Reviews, v. 52, p. 4–17.

Kniess, C. T., De Lima, J. C., and Prates, P. B., 2012, The quantification of crystalline phases in materials: Applications of Rietveld method in Shatokha, V., ed., Sintering – Methods and Products, Intech, p. 293-316.

Ku, H. H., 1966, Notes on the use of propagation of error formulas: Journal of Research of the National Bureau of Standards, Section C: Engineering and Instrumentation, v. 70C, p. 263.

Lackner, K. S., 2003, A guide to CO_2 sequestration: Science, v. 300, p. 1677-1678.

Lafuente, B., Downs, R. T., Yang, H. and Stone, N., eds., 2016, The power of databases: The RRUFF project: Highlights in Mineralogical Crystallography, p. 1-29.

Lechler, P. J., and Desilets, M. O., 1987, A review of the use of loss on ignition as a measurement of total volatiles in whole-rock analysis: Chemical Geology, v. 63, p. 341-344.

Liao, L. X., Ryan, D. H., and Altounian, Z., 1991, Mössbauer determination of cobalt substitution in iron-based intermetallics: Journal of Applied Physics, v. 70, p. 6143-6145.

Lindsay, M. B. J., Moncur, M. C., Bain, J. G., Jambor, J. L., Ptacek, C. J., and Blowes, D. W., 2015, Geochemical and mineralogical aspects of sulfide mine tailings: Applied Geochemistry, v. 57, p. 157–177.

Liu, W., Li, X., Wang, M., and Liu, L., 2021, Research trend and dynamical development of focusing on the global critical metals: a bibliometric analysis during 1991–2020: Environmental Science and Pollution Research.

Locock, A. J., 2008, An Excel spreadsheet to recast analyses of garnet into end-member components, and a synopsis of the crystal chemistry of natural silicate garnets: Computers and Geosciences, v. 34, p. 1769–1780.

Lutandula, M. S., and Maloba, B., 2013, Recovery of cobalt and copper through reprocessing of tailings from flotation of oxidised ores: Journal of Environmental Chemical Engineering, v. 1, p. 1085–1090.

Mackay, I., Videla, A. R., and Brito-Parada, P. R., 2020, The link between particle size and froth stability - Implications for reprocessing of flotation tailings: Journal of Cleaner Production, v. 242, p. 118436.

March, A., 1932, Mathematische theorie der regelung nach der korn gestalt bei affiner deformation: Zeitschrift für Kristallographie, v. 81, p. 285–297.

Mellini, M., 1982, The crystal structure of lizardite 1T: hydrogen bonds and polytypism.: American Mineralogist, v. 67, p. 587–598.

Mellini, M., and Viti, C., 1994, Crystal structure of lizardite-1T from Elba, Italy: American Mineralogist, v. 79(11-12), p. 1194–1198.

Mervine, E. M., Wilson, S. A., Power, I. M., Dipple, G. M., Turvey, C. C., Hamilton, J. L., Vanderzee, S., Raudsepp, M., Southam, C., Matter, J. M., Kelemen, P. B., Stiefenhofer, J., Miya, Z., and Southam, G., 2018, Potential for offsetting diamond mine carbon emissions through mineral carbonation of processed kimberlite: an assessment of De Beers mine sites in South Africa and Canada: Mineralogy and Petrology, v. 112, p. 755–765.

Meyer, D. R., 1980, Nutritional problems associated with the establishment of vegetation on tailings from an asbestos mine: Environmental Pollution (Series A), v. 23, p. 287–298.

Miles, J., 2005, R-squared, adjusted r-squared: Encyclopedia of Statistics in Behavioral Science, v. 4, p. 1655-1657.

Mililli, B. F., 2014, Carbonation of nickel rich ultramafic tailings from Lord Brassey Mine, Tasmania: Honours Thesis, Melbourne, Australia, Monash University, 48 p.

Mindat, 2022, Annabergite, (https://www.mindat.org/min-240.html)

Mosier, D. L., Singer, D. A., Moring, B. C., and Galloway, J. P., 2012, Podiform chromite deposits—database and grade and tonnage models: US Geological Survey Scientific Investigations, Report, p. 45.

Ostadrahimi, M., Farrokhpay, S., Gharibi, K., and Dehghani, A., 2020, Determining iron grades of ores or concentrates containing sulfide minerals: Metallurgical and Materials Transactions B: Process Metallurgy and Materials Processing Science, v. 51, p. 505–509.

Parbhakar-Fox, A., Glen, J., and Raimondo, B., 2018, A geometallurgical approach to tailings management: An example from the Savage River Fe-ore mine, western Tasmania: Minerals, v. 10, p. 454.

Park, J., Kim, K., Lee, T., and Kim, M., 2019, Tailings storage facilities (TSFs) dust control using biocompatible polymers: Mining, Metallurgy and Exploration, v. 36, p. 785–795.

Pawley, G. S., 1981, Unit-cell refinement from powder diffraction scans: Journal of Applied Crystallography, v. 14, p. 357–361.

Peck, C., and Keays, R. R., 1990, Geology, geochemistry, and origin of platinum-group element chromitite occurrences in the Heazlewood River Complex, Tasmania: Economic Geology, v. 85, p. 765–793.

Potts, P. J., 1992, A handbook of silicate rocks analysis: Springer, US, 622 p.

Power, I. M., McCutcheon, J., Harrison, A. L., Wilson, S. A., Dipple, G. M., Kelly, S., Southam, C., and Southam, G., 2014, Strategizing carbon-neutral mines: A case for pilot projects: Minerals, v. 4, p. 399–436.

Power, I. M., Paulo, C., Long, H., Lockhart, J. A., Stubbs, A. R., French, D., and Caldwell, R., 2021, Carbonation, cementation, and stabilization of ultramafic mine tailings: Environmental Science and Technology, v. 55, p. 10056–10066.

Rampacek, C., 1982, An overview of mining and mineral processing waste as a resource: Resources and Conservation, v. 9, p. 75–86.

Rietveld, H. M., 1969, A profile refinement method for nuclear and magnetic structures. Journal of Applied Crystallography, v. 2, p. 65–71.

Sandalow, D., Aines, R., Friedmann, J., Kelemen, P., McCormick, C., Power. I., Schmidt, B., and Wilson, S. A., 2021, Carbon mineralization roadmap: ICEF Innovation Roadmap Project, 89 p.

Scarlett, N. V. Y., and Madsen, I. C., 2006, Quantification of phases with partial or no known crystal structures: Powder Diffraction, v. 21, p. 278–284.

Schoenberger, E., 2016, Environmentally sustainable mining: The case of tailings storage facilities: Resources Policy, v. 49, p. 119–128.

Sciortino, M., Mungall, J. E., and Muinonen, J., 2015, Generation of high-Ni sulfide and alloy phases during serpentinization of dunite in the Dumont Sill, Quebec: Economic Geology, v. 110, p. 733–761.

Siebecker, M. G., Chaney, R. L., and Sparks, D. L., 2018, Natural speciation of nickel at the micrometer scale in serpentine (ultramafic) topsoils using microfocused X-ray fluorescence, diffraction, and absorption: Geochemical Transactions, v. 19, p. 1–16.

Slack, J. F., Kimball, B. E., and Shedd, K. B., 2017, Cobalt, chapter F: Critical mineral resources of the United States — Economic and environmental geology and prospects for future supply: Professional Paper 1802-F, p. F1–F40.

Sovacool, B. K., 2019, The precarious political economy of cobalt: Balancing prosperity, poverty, and brutality in artisanal and industrial mining in the Democratic Republic of the Congo: Extractive Industries and Society, v. 6, p. 915–939.

Stanković, V., Milošević, V., Milićević, D., Gorgievski, M., and Bogdanović, G., 2018, Reprocessing of the old flotation tailings deposited on the RTB Bor tailings pond – a case study: Chemical Industry and Chemical Engineering Quarterly, v. 24, p. 333–344.

Stefaniak, K., and Wróżyńska, M., 2018, On possibilities of using global monitoring in effective prevention of tailings storage facilities failures: Environmental Science and Pollution Research, v. 25, p. 5280–5297.

Toby, B. H., 2006, R factors in Rietveld analysis: How good is good enough?: Powder Diffraction, v. 21, p. 67-70.

Turvey, C. C., Hamilton, J. L., and Wilson, S. A., 2018, Comparison of Rietveld-compatible structureless fitting analysis methods for accurate quantification of carbon dioxide fixation in ultramafic mine tailings: American Mineralogist, v. 103, p. 1649–1662.

Uehara, S., 1998, TEM and XRD study of antigorite superstructures. Canadian Mineralogist, v. 36, p. 1595–1605.

Viani, A., Gualtieri, A. F., and Artioli, G., 2002, The nature of disorder in montmorillonite by simulation of X-ray powder patterns: American Mineralogist, v. 87, p. 966–975.

Wang, F., Dreisinger, D., Jarvis, M., Hitchins, T., and Trytten, L., 2021, CO_2 mineralization and concurrent utilization for nickel conversion from nickel silicates to nickel sulfides: Chemical Engineering Journal, v. 406, p. 126761.

West High Yield Resources, 2013, Revised NI 43-101 technical report - Preliminary economic assessment Record Ridge Project British Columbia, Canada: SRK Consulting (U.S) Inc, 183200.020.

Wilson, S. A., Raudsepp, M., and Dipple, G. M., 2006, Verifying and quantifying carbon fixation in minerals from serpentine-rich mine tailings using the Rietveld method with X-ray powder diffraction data: American Mineralogist, v. 91, p. 1331–1341.

Wilson, S. A., Dipple, G. M., Power, I. M., Thom, J. M., Anderson, R. G., Raudsepp, M., Gabites, J. E., and Southam, G., 2009a, Carbon dioxide fixation within mine wastes of ultramafic-hosted ore deposits: Examples from the Clinton Creek and Cassiar Chrysotile deposits, Canada: Economic Geology, v. 104, p. 95–112.

Wilson, S. A., Raudsepp, M., and Dipple, G. M., 2009b, Quantifying carbon fixation in trace minerals from processed kimberlite: A comparative study of quantitative methods using X-ray powder diffraction data with applications to the Diavik Diamond Mine, Northwest Territories, Canada. Applied Geochemistry, v. 24, p. 2312–2331.

Wilson, S. A., Harrison, A. L., Dipple, G. M., Power, I. M., Barker, S. L. L., Mayer, K. U., Fallon, S. J., Raudsepp, M., and Southam, G., 2014, Offsetting of CO2 emissions by air capture in mine tailings at the Mount Keith Nickel Mine, Western Australia: Rates, controls and prospects for carbon neutral mining: International Journal of Greenhouse Gas Control, v. 25, p. 121–140.

Yavuz, F., Kumral, M., Karakaya, N., Karakaya, M. T., and Yildirim, D. K., 2015, A Windows program for chlorite calculation and classification: Computers and Geosciences, v. 81, p. 101–113.

APPENDIX

Table A.1. Quantitative X-ray diffraction data of mineralogical abundances in Record Ridge samples.

Sample Mineral	20RRP1-1 (wt%)	20RRP2-2 (wt%)	20RRP3-1A (wt%)	20RRP3-1C (wt%)	20RRP3-1W (wt%)	20RRP5-1 (wt%)	20RRP6-1 (wt%)
Lizardite	64.9		67.7	66.0	66.9	62.9	65.8
Antigorite	15.2		13.9	8.4	15.3	28.0	
Chromite	1.0		0.6	0.8	1.0	0.4	
Magnetite	10.4	5.7	9.0	8.9	8.1	8.7	4.4
Magnesite	5.4		1.9	5.0	3.9		
Brucite	3.1		0.5	1.3	0.2		
Orthoclase		46.0					
Actinolite		11.1					
Clinochlore		1.3					11.0
Albite		30.5					
Biotite		5.5					
Forsterite			6.4	9.1	4.5		13.2
Talc							3.3
Dolomite			0.1	0.5	0.1		0.8
Hydromagnesite							0.1
Pyroaurite							1.4
Total	100.0	100.1	100.1	100.0	100.0	100.0	100.0
Rwp [1] (%)	11.9	15.5	12.0	10.8	13.1	14.6	8.5
DW [2]	0.2	0.2	0.1	0.2	0.1	0.1	0.3
χ^{2} [(3)]	4.3	4.5	4.3	3.8	4.7	5.4	2.9

Table A.1. (continued). Quantitative X-ray diffraction data of mineralogical abundances in Record Ridge samples.

Sample Mineral	20RRP7-1 (wt%)	20RRP7-2 (wt%)	20RRP11-1 (wt%)	20RRP12-1A (wt%)	20RRP12-1C (wt%)	20RRP12-1W (wt%)	20RRP13-1 (wt%)
Lizardite	28.8		56.0	47.6	48.2	52.4	66.7
Antigorite			12.0				10.9
Chromite		0.6					
Magnetite	4.8	4.8	3.8	7.0	5.9	5.8	4.5
Magnesite							6.0
Brucite	0.6		2.5				
Orthoclase		2.2					
Actinolite	12.1	5.5		6.3	7.6	5.9	
Clinochlore	5.5	29.7	14.7	6.6	5.6	6.0	10.5
Albite		4.0					
Forsterite	43.0		3.8	30.0	29.6	27.7	
Talc	3.6		5.7				
Epidote		50.7					
Calcite	0.4		0.2	1.5	2.0	1.2	
Dolomite							1.4
Hydromagnesite			1.1	0.3	0.2	0.2	
Pyroaurite	1.3	1.3		0.9	0.9	0.7	
Gypsum		1.1					
Total	100.0	100.0	100.0	100.0	100.0	100.0	100.0
Rwp [1] (%)	7.4	9.8	7.8	8.1	9.2	8.5	6.4
DW [2]	0.4	0.3	0.3	0.3	0.3	0.3	0.5
χ^{2} [(3)]	2.4	3.1	2.6	2.8	3.1	2.9	2.3

[1]Weighted profile R-factor percentage indicating area under the peak unaccounted for by model.

[2]Durban Watson statistic for serial correlation.

[3]Chi-square statistic for goodness of fit.

Table A.2. Whole rock analysis for Lord Brassey samples.

ANALYTE CSA	LOD	UNIT	14LBM1-3	14LBM1-5	14LBM1-9	14LBM1-10	14LBM1-19
C	0.005	%	0.044	0.058	0.07	0.049	0.086
S	0.005	%	0.009	0.011	0.012	0.071	0.023

ANALYTE XRF	LOD	UNIT	14LBM1-3	14LBM1-5	14LBM1-9	14LBM1-10	14LBM1-19
LOI_V	-10	%	11.8576	11.3577	13.6273	12.62	13.4973
Al_2O_3	0.01	%	3	3.54	5.89	1.42	0.95
CaO	0.01	%	6.35	7.58	2.31	3.21	0.02
Cr_2O_3	0.01	%	0.39	1.01	0.63	0.67	0.32
Fe_2O_3	0.01	%	9.1	9.01	8.99	8.67	12.7
K_2O	0.01	%	<0.01	<0.01	<0.01	<0.01	<0.01
MgO	0.01	%	28.53	28.13	31.24	31.89	34.26
Mn_3O_4	0.01	%	0.26	0.17	0.17	0.2	0.11
Na_2O	0.01	%	0.03	0.03	0.04	0.02	0.03
P_2O_5	0.01	%	0.04	<0.01	<0.01	<0.01	<0.01
SiO_2	0.01	%	39.09	38.6	35.66	39.81	36.26
TiO_2	0.01	%	0.04	0.01	0.08	0.01	<0.01
V_2O_5	0.01	%	0.02	<0.01	0.02	<0.01	<0.01
Sum	0.01	%	87.02	88.35	85.23	86.45	84.98

Table A.2. (continued). Whole rock analysis for Lord Brassey samples.

ANALYTE CSA	LOD	UNIT	14LBM1-21	14LBM1-28	14LBM1-31	14LBM1-32
C	0.005	%	0.124	0.044	0.056	0.094
S	0.005	%	0.013	0.047	0.116	0.053

ANALYTE XRF	LOD	UNIT	14LBM1-21	14LBM1-28	14LBM1-31	14LBM1-32
LOI_V	-10	%	14.1086	12.65	12.7187	14.71
Al_2O_3	0.01	%	2.62	3.02	1.68	1.52
CaO	0.01	%	1.04	3.43	0.02	0.23
Cr_2O_3	0.01	%	0.91	0.96	0.72	0.53
Fe_2O_3	0.01	%	9.95	8.02	11.87	9.29
K_2O	0.01	%	<0.01	<0.01	<0.01	<0.01
MgO	0.01	%	33.73	31.82	34.05	35.12
Mn_3O_4	0.01	%	0.13	0.14	0.11	0.18
Na_2O	0.01	%	0.03	0.02	0.01	0.02
P_2O_5	0.01	%	<0.01	<0.01	0.01	<0.01
SiO_2	0.01	%	36.04	38.08	36.54	36.55
TiO_2	0.01	%	0.01	0.01	0.01	0.01
V_2O_5	0.01	%	<0.01	0.01	<0.01	0.01
Sum	0.01	%	84.75	85.88	86.22	83.88

Table A.2. (continued). Whole rock analysis for Lord Brassey samples.

ANALYTE ICP-OES	LOD	UNIT	14LBM1-3	14LBM1-5	14LBM1-9	14LBM1-10	14LBM1-19
Al	0.01	%	1.56	1.78	3.04	0.7	0.49
Ba	10	ppm	<10	<10	<10	<10	<10
Be	5	ppm	<5	<5	<5	<5	<5
Ca	0.1	%	4.4	5.1	1.6	2.2	0.1
Cr	10	ppm	2740	6821	4393	4642	2177
Cu	10	ppm	<10	<10	<10	<10	<10
Fe	0.01	%	6.38	6.17	6.25	5.82	8.85
K	0.1	%	<0.1	<0.1	<0.1	<0.1	<0.1
Li	10	ppm	<10	<10	11	<10	<10
Mg	0.01	%	17.15	16.36	18.57	18.36	20.4
Mn	10	ppm	1945	1234	1261	1525	841
Ni	5	ppm	954	1550	1196	2592	1951
P	0.01	%	0.02	<0.01	<0.01	<0.01	<0.01
Sc	5	ppm	29	10	16	7	6
Si	0.1	%	17.7	17.1	16	17.2	16.2
Sr	10	ppm	<10	<10	<10	<10	<10
Ti	0.01	%	0.02	0.01	0.05	<0.01	<0.01
V	5	ppm	96	53	109	37	21
Zn	5	ppm	26	24	40	28	32

Table A.2. (continued). Whole rock analysis for Lord Brassey samples.

ANALYTE ICP-OES	LOD	UNIT	14LBM1-21	14LBM1-28	14LBM1-31	14LBM1-32
Al	0.01	%	1.34	1.57	0.86	0.78
Ba	10	ppm	<10	<10	<10	<10
Be	5	ppm	<5	<5	<5	<5
Ca	0.1	%	0.8	2.4	0.1	0.2
Cr	10	ppm	6129	6459	5064	3735
Cu	10	ppm	<10	24	13	<10
Fe	0.01	%	6.78	5.52	8.28	6.34
K	0.1	%	<0.1	<0.1	<0.1	<0.1
Li	10	ppm	<10	<10	<10	<10
Mg	0.01	%	20.05	18.71	20.51	20.75
Mn	10	ppm	912	1077	791	1309
Ni	5	ppm	1666	1622	7179	1881
P	0.01	%	<0.01	<0.01	<0.01	<0.01
Sc	5	ppm	8	10	8	8
Si	0.1	%	16	17	16.4	16.1
Sr	10	ppm	<10	<10	<10	<10
Ti	0.01	%	0.01	0.01	<0.01	<0.01
V	5	ppm	41	48	39	31
Zn	5	ppm	41	39	33	44

Table A.2. (continued). Whole rock analysis for Lord Brassey samples.

ANALYTE ICP-MS	LOD	UNIT	14LBM1-3	14LBM1-5	14LBM1-9	14LBM1-10	14LBM1-19
Ag	1	ppm	<1	<1	<1	<1	<1
As	5	ppm	<5	<5	<5	<5	<5
Bi	0.1	ppm	<0.1	<0.1	<0.1	<0.1	<0.1
Cd	0.2	ppm	<0.2	<0.2	<0.2	<0.2	<0.2
Ce	0.1	ppm	2.1	0.7	0.2	0.4	0.1
Co	0.5	ppm	80.1	96.5	78.9	109	110
Cs	0.1	ppm	<0.1	<0.1	<0.1	<0.1	<0.1
Dy	0.05	ppm	0.51	0.11	0.2	0.07	<0.05
Er	0.05	ppm	0.34	0.1	0.14	<0.05	<0.05
Eu	0.05	ppm	0.06	<0.05	<0.05	<0.05	<0.05
Ga	1	ppm	2	4	3	1	<1
Gd	0.05	ppm	0.38	0.06	0.12	<0.05	<0.05
Ge	1	ppm	<1	1	<1	1	<1
Hf	1	ppm	<1	<1	<1	<1	<1
Ho	0.05	ppm	0.1	<0.05	<0.05	<0.05	<0.05
In	0.2	ppm	<0.2	<0.2	<0.2	<0.2	<0.2
La	0.1	ppm	0.7	0.3	<0.1	0.2	<0.1
Lu	0.05	ppm	0.05	<0.05	<0.05	<0.05	<0.05
Mo	2	ppm	<2	<2	<2	<2	<2
Nb	1	ppm	<1	<1	<1	<1	<1
Nd	0.1	ppm	1.3	0.2	0.1	0.1	<0.1

Table A.2. (continued). Whole rock analysis for Lord Brassey samples.

ANALYTE ICP-MS	LOD	UNIT	14LBM1-21	14LBM1-28	14LBM1-31	14LBM1-32
Ag	1	ppm	<1	<1	<1	<1
As	5	ppm	<5	<5	17	<5
Bi	0.1	ppm	<0.1	<0.1	0.4	<0.1
Cd	0.2	ppm	<0.2	<0.2	<0.2	<0.2
Ce	0.1	ppm	<0.1	0.5	0.1	<0.1
Co	0.5	ppm	109	93.8	146	122
Cs	0.1	ppm	<0.1	<0.1	<0.1	<0.1
Dy	0.05	ppm	0.09	0.06	<0.05	0.09
Er	0.05	ppm	0.08	<0.05	0.06	0.05
Eu	0.05	ppm	<0.05	<0.05	<0.05	<0.05
Ga	1	ppm	1	3	2	<1
Gd	0.05	ppm	0.05	<0.05	<0.05	<0.05
Ge	1	ppm	<1	<1	<1	<1
Hf	1	ppm	<1	<1	<1	<1
Ho	0.05	ppm	<0.05	<0.05	<0.05	<0.05
In	0.2	ppm	<0.2	<0.2	<0.2	<0.2
La	0.1	ppm	<0.1	0.3	<0.1	<0.1
Lu	0.05	ppm	<0.05	<0.05	<0.05	<0.05
Mo	2	ppm	<2	<2	<2	<2
Nb	1	ppm	<1	<1	<1	<1
Nd	0.1	ppm	<0.1	0.1	<0.1	<0.1

Table A.2. (continued). Whole rock analysis for Lord Brassey samples.

ANALYTE ICP-MS	LOD	UNIT	14LBM1-3	14LBM1-5	14LBM1-9	14LBM1-10	14LBM1-19
Pb	5	ppm	<5	<5	<5	<5	<5
Pr	0.05	ppm	0.31	0.07	<0.05	<0.05	<0.05
Rb	0.2	ppm	0.8	1.1	0.9	0.7	0.9
Sb	0.1	ppm	<0.1	<0.1	<0.1	<0.1	<0.1
Sm	0.1	ppm	0.3	<0.1	<0.1	<0.1	<0.1
Sn	1	ppm	<1	<1	<1	<1	<1
Ta	0.5	ppm	<0.5	<0.5	<0.5	<0.5	<0.5
Tb	0.05	ppm	0.07	<0.05	<0.05	<0.05	<0.05
Th	0.1	ppm	0.7	0.2	<0.1	<0.1	<0.1
Tl	0.5	ppm	<0.5	<0.5	<0.5	<0.5	<0.5
Tm	0.05	ppm	<0.05	<0.05	<0.05	<0.05	<0.05
U	0.05	ppm	<0.05	0.08	<0.05	<0.05	0.07
W	1	ppm	6	12	23	7	4
Y	0.5	ppm	2.5	0.7	1	<0.5	<0.5
Yb	0.1	ppm	0.4	0.1	0.2	<0.1	<0.1
Zr	0.5	ppm	5.3	<0.5	<0.5	<0.5	2.7

Table A.2. (continued). Whole rock analysis for Lord Brassey samples.

ANALYTE ICP-MS	LOD	UNIT	14LBM1-21	14LBM1-28	14LBM1-31	14LBM1-32
Pb	5	ppm	<5	<5	<5	<5
Pr	0.05	ppm	<0.05	0.06	<0.05	<0.05
Rb	0.2	ppm	1	0.7	0.8	0.6
Sb	0.1	ppm	<0.1	<0.1	<0.1	<0.1
Sm	0.1	ppm	<0.1	<0.1	<0.1	<0.1
Sn	1	ppm	<1	<1	<1	<1
Ta	0.5	ppm	<0.5	<0.5	<0.5	<0.5
Tb	0.05	ppm	<0.05	<0.05	<0.05	<0.05
Th	0.1	ppm	<0.1	0.1	<0.1	<0.1
Tl	0.5	ppm	<0.5	<0.5	<0.5	<0.5
Tm	0.05	ppm	<0.05	<0.05	<0.05	<0.05
U	0.05	ppm	<0.05	0.05	0.05	<0.05
W	1	ppm	8	5	10	2
Y	0.5	ppm	0.6	<0.5	<0.5	<0.5
Yb	0.1	ppm	<0.1	<0.1	<0.1	<0.1
Zr	0.5	ppm	<0.5	1.6	<0.5	<0.5

Abbreviations: LOD = limit of detection. CSA = carbon sulfur analysis. XRF = X-ray fluorescence. ICP-MS = inductively coupled plasma mass spectrometry. ICP-OES = inductively coupled plasma optical emission spectrometry.

Table A.3. Whole rock analysis for Record Ridge samples.

ANALYTE CSA	LOD	UNIT	20RRP1-1	20RRP2-2	20RRP3-1A	20RRP3-1C	20RRP3-1W	20RRP5-1	20RRP6-1
C	0.005	%	0.799	0.04	0.477	0.88	0.645	0.045	0.312
S	0.005	%	0.09	<0.005	0.068	0.08	0.049	0.048	0.073

ANALYTE XRF	LOD	UNIT	20RRP1-1	20RRP2-2	20RRP3-1A	20RRP3-1C	20RRP3-1W	20RRP5-1	20RRP6-1
LOI_V	-10	%	14.7485	1.75965	13.7786	14.66	14.17	13.05	13.3287
Al_2O_3	0.01	%	0.23	17.43	0.48	0.43	0.46	0.22	0.28
CaO	0.01	%	0.09	4.18	0.03	0.17	0.04	0.02	0.32
Cr_2O_3	0.01	%	0.47	0.02	0.45	0.39	0.47	0.31	0.52
Fe_2O_3	0.01	%	9.04	7.31	7.76	8.09	7.78	8.42	8.38
K_2O	0.01	%	<0.01	7.04	<0.01	<0.01	<0.01	<0.01	<0.01
MgO	0.01	%	38.67	2.77	37.81	37.58	38.01	36.76	38.01
Mn_3O_4	0.01	%	0.14	0.12	0.1	0.11	0.1	0.08	0.13
Na_2O	0.01	%	0.02	2.99	0.01	0.02	0.02	<0.01	0.01
P_2O_5	0.01	%	0.01	0.61	<0.01	<0.01	<0.01	<0.01	<0.01
SiO_2	0.01	%	36.63	54.85	39.66	36.44	39.63	41.93	37.23
TiO_2	0.01	%	<0.01	1.02	<0.01	<0.01	<0.01	<0.01	<0.01
V_2O_5	0.01	%	<0.01	0.04	<0.01	<0.01	<0.01	<0.01	<0.01
Sum	0.01	%	85.82	98.38	86.77	83.71	86.96	88.15	85.38

Table A.3. (continued). Whole rock analysis for Record Ridge samples.

ANALYTE CSA	LOD	UNIT	20RRP7-1	20RRP7-2	20RRP11-1	20RRP12-1A	20RRP12-1C	20RRP12-1W	20RRP13-1
C	0.005	%	0.206	0.084	0.172	0.295	0.332	0.22	1.217
S	0.005	%	0.015	<0.005	0.134	0.148	0.183	0.126	0.03

ANALYTE XRF	LOD	UNIT	20RRP7-1	20RRP7-2	20RRP11-1	20RRP12-1A	20RRP12-1C	20RRP12-1W	20RRP13-1
LOI_V	-10	%	8.11	7.68	13.16	9.85901	10.079	10.4	16.9183
Al_2O_3	0.01	%	0.26	21.28	0.26	0.27	0.29	0.29	0.23
CaO	0.01	%	2.17	12.86	0.19	1.61	2.13	1.53	0.68
Cr_2O_3	0.01	%	0.37	0.01	0.39	0.34	0.41	0.38	0.35
Fe_2O_3	0.01	%	7.31	13.41	7.16	9.16	8.37	7.84	8.35
K_2O	0.01	%	<0.01	0.04	<0.01	<0.01	<0.01	<0.01	<0.01
MgO	0.01	%	38.63	10.78	37.19	37.89	37.88	37.67	35.12
Mn_3O_4	0.01	%	0.14	0.24	0.11	0.1	0.1	0.1	0.12
Na_2O	0.01	%	0.03	0.18	0.03	0.03	0.02	0.04	0.02
P_2O_5	0.01	%	<0.01	0.29	<0.01	0.02	<0.01	0.03	0.01
SiO_2	0.01	%	41.12	32.27	39.62	38.76	38.63	39.86	36.51
TiO_2	0.01	%	<0.01	1.2	<0.01	<0.01	<0.01	<0.01	<0.01
V_2O_5	0.01	%	<0.01	0.08	<0.01	<0.01	<0.01	<0.01	<0.01
Sum	0.01	%	90.42	92.65	85.58	88.83	88.55	88.35	81.75

Table A.3. (continued). Whole rock analysis for Record Ridge samples.

ANALYTE ICP-OES	LOD	UNIT	20RRP1-1	20RRP2-2	20RRP3-1A	20RRP3-1C	20RRP3-1W	20RRP5-1	20RRP6-1
Al	0.01	%	0.1	8.65	0.23	0.21	0.23	0.11	0.14
Ba	10	ppm	<10	2410	<10	<10	<10	<10	<10
Be	5	ppm	<5	<5	<5	<5	<5	<5	<5
Ca	0.1	%	0.1	2.9	<0.1	0.2	0.1	0.1	0.3
Cr	10	ppm	3154	146	3054	2660	3141	1964	3484
Cu	10	ppm	<10	21	<10	30	<10	<10	<10
Fe	0.01	%	6.1	4.91	5.35	5.38	5.12	5.67	5.78
K	0.1	%	0.1	5.4	0.1	0.1	0.1	0.1	0.1
Li	10	ppm	<10	30	<10	<10	<10	<10	<10
Mg	0.01	%	22.34	1.53	22.04	21.69	21.55	21.22	22.5
Mn	10	ppm	920	890	648	750	719	533	954
Ni	5	ppm	2433	75	2215	2056	2116	1992	2199
P	0.01	%	<0.01	0.25	<0.01	<0.01	<0.01	<0.01	<0.01
Sc	5	ppm	<5	10	6	6	6	6	<5
Si	0.1	%	16	23.4	17.6	15.7	17	18.3	16.7
Sr	10	ppm	<10	1351	<10	47	10	<10	17
Ti	0.01	%	<0.01	0.58	<0.01	<0.01	<0.01	<0.01	<0.01
V	5	ppm	21	120	28	28	27	21	22
Zn	5	ppm	53	92	47	52	44	45	33

Table A.3. (continued). Whole rock analysis for Record Ridge samples.

ANALYTE ICP-OES	LOD	UNIT	20RRP7-1	20RRP7-2	20RRP11-1	20RRP12-1A	20RRP12-1C	20RRP12-1W	20RRP13-1
Al	0.01	%	0.13	10.79	0.11	0.13	0.14	0.13	0.13
Ba	10	ppm	<10	14	<10	<10	<10	<10	<10
Be	5	ppm	<5	<5	<5	<5	<5	<5	<5
Ca	0.1	%	1.5	8.5	0.2	1.1	1.5	1.1	0.5
Cr	10	ppm	2414	95	2549	2358	2881	2601	2448
Cu	10	ppm	<10	<10	11	21	31	42	<10
Fe	0.01	%	5.02	9.04	4.76	6.19	5.74	5.44	5.85
K	0.1	%	0.1	0.1	<0.1	0.1	<0.1	<0.1	<0.1
Li	10	ppm	<10	62	<10	<10	<10	<10	<10
Mg	0.01	%	22.86	6.16	21.29	22.22	22.5	22.77	21.15
Mn	10	ppm	996	1724	736	695	699	712	949
Ni	5	ppm	2248	19	2396	2217	2116	2212	1968
P	0.01	%	<0.01	0.12	<0.01	<0.01	<0.01	<0.01	<0.01
Sc	5	ppm	<5	47	<5	<5	<5	<5	<5
Si	0.1	%	18.4	14.5	17	17.1	17.2	17.9	16.5
Sr	10	ppm	<10	1906	11	31	36	26	29
Ti	0.01	%	<0.01	0.71	<0.01	<0.01	<0.01	<0.01	<0.01
V	5	ppm	21	400	19	20	22	20	25
Zn	5	ppm	43	29	36	27	25	25	40

Table A.3. (continued). Whole rock analysis for Record Ridge samples.

ANALYTE ICP-MS	LOD	UNIT	20RRP1-1	20RRP2-2	20RRP3-1A	20RRP3-1C	20RRP3-1W	20RRP5-1	20RRP6-1
Ag	1	ppm	<1	<1	<1	<1	<1	<1	<1
As	5	ppm	23	<5	16	16	16	27	251
Bi	0.1	ppm	<0.1	0.1	<0.1	<0.1	<0.1	0.3	<0.1
Cd	0.2	ppm	<0.2	0.2	<0.2	<0.2	<0.2	<0.2	<0.2
Ce	0.1	ppm	<0.1	135	0.1	<0.1	<0.1	0.5	<0.1
Co	0.5	ppm	130	29.7	109	108	111	100	123
Cs	0.1	ppm	<0.1	3.1	<0.1	<0.1	<0.1	<0.1	0.2
Dy	0.05	ppm	<0.05	4.52	<0.05	<0.05	<0.05	<0.05	<0.05
Er	0.05	ppm	<0.05	2.13	<0.05	<0.05	<0.05	<0.05	<0.05
Eu	0.05	ppm	<0.05	2.05	<0.05	<0.05	<0.05	<0.05	<0.05
Ga	1	ppm	<1	19	<1	<1	<1	<1	<1
Gd	0.05	ppm	<0.05	5.84	<0.05	<0.05	<0.05	0.07	<0.05
Ge	1	ppm	2	1	<1	<1	<1	2	1
Hf	1	ppm	<1	6	<1	<1	<1	<1	<1
Ho	0.05	ppm	<0.05	0.77	<0.05	<0.05	<0.05	<0.05	<0.05
In	0.2	ppm	<0.2	<0.2	<0.2	<0.2	<0.2	<0.2	<0.2
La	0.1	ppm	<0.1	71.9	<0.1	<0.1	<0.1	0.5	<0.1
Lu	0.05	ppm	<0.05	0.3	<0.05	<0.05	<0.05	<0.05	<0.05
Mo	2	ppm	<2	3	2	<2	5	<2	<2
Nb	1	ppm	<1	59	<1	<1	<1	<1	<1
Nd	0.1	ppm	<0.1	50.8	<0.1	<0.1	<0.1	0.5	<0.1

Table A.3. (continued). Whole rock analysis for Record Ridge samples.

ANALYTE ICP-MS	LOD	UNIT	20RRP7-1	20RRP7-2	20RRP11-1	20RRP12-1A	20RRP12-1C	20RRP12-1W	20RRP13-1
Ag	1	ppm	<1	<1	<1	<1	<1	<1	<1
As	5	ppm	26	9	28	28	24	24	31
Bi	0.1	ppm	<0.1	<0.1	0.1	0.2	0.2	0.2	0.2
Cd	0.2	ppm	<0.2	<0.2	<0.2	<0.2	<0.2	<0.2	<0.2
Ce	0.1	ppm	0.3	22.6	<0.1	<0.1	<0.1	<0.1	0.1
Co	0.5	ppm	117	47	107	115	114	116	99.7
Cs	0.1	ppm	0.1	0.6	0.3	<0.1	<0.1	<0.1	0.6
Dy	0.05	ppm	<0.05	4.99	<0.05	<0.05	<0.05	<0.05	<0.05
Er	0.05	ppm	<0.05	2.82	<0.05	<0.05	<0.05	<0.05	<0.05
Eu	0.05	ppm	<0.05	1.24	<0.05	<0.05	<0.05	<0.05	<0.05
Ga	1	ppm	<1	15	<1	<1	<1	<1	<1
Gd	0.05	ppm	<0.05	4.37	<0.05	<0.05	<0.05	<0.05	<0.05
Ge	1	ppm	<1	<1	1	<1	1	1	1
Hf	1	ppm	<1	2	<1	<1	<1	<1	<1
Ho	0.05	ppm	<0.05	0.95	<0.05	<0.05	<0.05	<0.05	<0.05
In	0.2	ppm	<0.2	<0.2	<0.2	<0.2	<0.2	<0.2	<0.2
La	0.1	ppm	0.2	10.3	<0.1	<0.1	<0.1	<0.1	0.2
Lu	0.05	ppm	<0.05	0.41	<0.05	<0.05	<0.05	<0.05	<0.05
Mo	2	ppm	<2	2	<2	<2	<2	<2	<2
Nb	1	ppm	<1	3	<1	<1	<1	<1	<1
Nd	0.1	ppm	0.1	14.1	<0.1	<0.1	<0.1	<0.1	<0.1

Table A.3. (continued). Whole rock analysis for Record Ridge samples.

ANALYTE ICP-MS	LOD	UNIT	20RRP1-1	20RRP2-2	20RRP3-1A	20RRP3-1C	20RRP3-1W	20RRP5-1	20RRP6-1
Pb	5	ppm	12	<5	<5	<5	<5	<5	<5
Pr	0.05	ppm	<0.05	3.18	<0.05	<0.05	<0.05	<0.05	<0.05
Rb	0.2	ppm	0.7	1.9	1.1	1	0.8	0.7	0.8
Sb	0.1	ppm	4.5	2.3	1.5	2.8	2.7	2.9	8.7
Sm	0.1	ppm	<0.1	3.8	<0.1	<0.1	<0.1	<0.1	<0.1
Sn	1	ppm	<1	<1	<1	<1	<1	<1	<1
Ta	0.5	ppm	<0.5	<0.5	<0.5	<0.5	<0.5	<0.5	<0.5
Tb	0.05	ppm	<0.05	0.7	<0.05	<0.05	<0.05	<0.05	<0.05
Th	0.1	ppm	<0.1	1.9	<0.1	<0.1	<0.1	<0.1	<0.1
Tl	0.5	ppm	<0.5	<0.5	<0.5	<0.5	<0.5	<0.5	<0.5
Tm	0.05	ppm	<0.05	0.42	<0.05	<0.05	<0.05	<0.05	<0.05
U	0.05	ppm	<0.05	1.01	<0.05	<0.05	<0.05	<0.05	<0.05
W	1	ppm	55	41	8	24	19	21	6
Y	0.5	ppm	<0.5	24.1	<0.5	<0.5	<0.5	<0.5	<0.5
Yb	0.1	ppm	<0.1	2.9	<0.1	<0.1	<0.1	<0.1	<0.1
Zr	0.5	ppm	4.3	77.3	<0.5	<0.5	2.5	<0.5	<0.5

Table A.3. (continued). Whole rock analysis for Record Ridge samples.

ANALYTE ICP-MS	LOD	UNIT	20RRP7-1	20RRP7-2	20RRP11-1	20RRP12-1A	20RRP12-1C	20RRP12-1W	20RRP13-1
Pb	5	ppm	<5	35	<5	<5	<5	<5	<5
Pr	0.05	ppm	<0.05	14.9	<0.05	<0.05	<0.05	0.14	<0.05
Rb	0.2	ppm	<0.2	239	0.4	0.4	0.6	0.5	0.8
Sb	0.1	ppm	3.3	0.4	3.1	3.9	3.5	7.5	8.6
Sm	0.1	ppm	<0.1	8.1	<0.1	<0.1	<0.1	<0.1	<0.1
Sn	1	ppm	<1	2	<1	<1	<1	<1	<1
Ta	0.5	ppm	<0.5	3.6	<0.5	<0.5	<0.5	<0.5	<0.5
Tb	0.05	ppm	<0.05	0.76	<0.05	<0.05	<0.05	<0.05	<0.05
Th	0.1	ppm	<0.1	20.2	<0.1	<0.1	<0.1	<0.1	<0.1
Tl	0.5	ppm	<0.5	0.9	<0.5	<0.5	<0.5	<0.5	<0.5
Tm	0.05	ppm	<0.05	0.3	<0.05	<0.05	<0.05	<0.05	<0.05
U	0.05	ppm	<0.05	6.09	<0.05	<0.05	<0.05	<0.05	<0.05
W	1	ppm	11	119	18	17	13	11	11
Y	0.5	ppm	<0.5	21.1	<0.5	<0.5	<0.5	<0.5	<0.5
Yb	0.1	ppm	<0.1	2.1	<0.1	<0.1	<0.1	<0.1	<0.1
Zr	0.5	ppm	1.9	274	1.3	10	<0.5	<0.5	2.5

Abbreviations: LOD = limit of detection. CSA = carbon sulfur analysis. XRF = X-ray fluorescence. ICP-MS = inductively coupled plasma mass spectrometry. ICP-OES = inductively coupled plasma optical emission spectrometry.

Table A.4. Calculated whole rock mineralogical compositions from integrating QXRD and EPMA data compared against measured values for Lord Brassey samples.

14LBM1-3 Oxide	Lizardite wt%	Antigorite wt%	Andradite wt%	Clinochlore wt%	Chromite wt%
LOI_V	7.906	2.381	0.094	0.799	0.000
Al_2O_3	0.725	0.218	0.475	1.104	0.050
CaO	0.066	0.020	4.115	0.003	0.003
Cr_2O_3	0.221	0.067	0.088	0.066	0.357
Fe_2O_3	2.706	0.815	3.091	0.348	0.263
K_2O	0.001	0.000	0.000	0.000	0.000
MgO	24.506	7.381	0.045	2.101	0.020
Mn_3O_4	0.125	0.038	0.006	0.001	0.003
Na_2O	0.002	0.001	0.001	0.000	0.000
P_2O_5	0.000	0.000	0.000	0.000	0.000
SiO_2	26.007	7.832	4.316	2.000	0.000
TiO_2	0.003	0.001	0.014	0.000	0.001
V_2O_5	0.000	0.000	0.005	0.000	0.003
NiO	0.087	0.026	0.000	0.009	0.000
SUM	62.355	18.780	12.250	6.431	0.700

Table A.4. (continued). Calculated whole rock mineralogical compositions from integrating QXRD and EPMA data compared against measured values for Lord Brassey samples.

14LBM1-3	SUM	Absolute Error	XRF	Absolute Error	Absolute Error	Relative Error
Oxide	wt%	wt%	wt%	wt%	wt%	%
LOI_V	11.180	0.391	11.858	0.035	0.678	5.718
Al_2O_3	2.572	0.614	3.000	0.014	0.428	14.267
CaO	4.207	0.383	6.350	0.010	2.143	33.748
Cr_2O_3	0.799	0.548	0.390	0.010	0.409	104.872
Fe_2O_3	7.223	0.912	9.100	0.021	1.877	20.626
K_2O	0.001	0.003	0.000	0.010	0.001	
MgO	34.053	1.650	28.530	0.057	5.523	19.359
Mn_3O_4	0.173	0.065	0.260	0.007	0.087	33.462
Na_2O	0.004	0.006	0.030	0.007	0.026	86.667
P_2O_5	0.000	0.000	0.040	0.007	0.040	100.000
SiO_2	40.155	1.667	39.090	0.010	1.065	2.724
TiO_2	0.019	0.011	0.040	0.010	0.021	52.500
V_2O_5	0.008	0.004	0.020	0.050	0.012	60.000
NiO	0.122	0.025	0.121	0.003	0.001	0.826
SUM	100.516	2.705	98.829	0.091	1.687	1.707

Table A.4. (continued). Calculated whole rock mineralogical compositions from integrating QXRD and EPMA data compared against measured values for Lord Brassey samples.

14LBM1-5	Lizardite	Antigorite	Andradite	Clinochlore	Chromite	Magnetite	Heazlewoodite	Diopside
Oxide	wt%	wt%	wt%	wt%	wt%	wt%	wt%	wt%
LOI_V	8.619	1.236	0.103	0.949	0.000	0.000	0.000	0.000
Al_2O_3	2.088	0.299	0.274	1.158	0.100	0.000	0.000	0.003
CaO	0.046	0.007	4.132	0.009	0.000	0.000	0.000	0.414
Cr_2O_3	0.251	0.036	0.130	0.048	0.210	0.000	0.000	0.001
Fe_2O_3	3.439	0.493	3.283	0.487	0.123	0.037	0.002	0.047
K_2O	0.005	0.001	0.000	0.001	0.000	0.000	0.000	0.000
MgO	26.513	3.801	0.039	2.505	0.048	0.000	0.000	0.300
Mn_3O_4	0.102	0.015	0.000	0.006	0.001	0.000	0.000	0.005
Na_2O	0.004	0.001	0.000	0.001	0.000	0.000	0.000	0.000
P_2O_5	0.000	0.000	0.000	0.000	0.000	0.000	0.000	0.000
SiO_2	26.503	3.799	4.263	2.420	0.000	0.000	0.000	0.900
TiO_2	0.006	0.001	0.008	0.001	0.001	0.000	0.000	0.000
V_2O_5	0.000	0.000	0.002	0.000	0.001	0.000	0.000	0.000
NiO	0.116	0.017	0.000	0.010	0.000	0.000	0.124	0.000
SUM	67.692	9.706	12.234	7.595	0.484	0.037	0.126	1.670

Table A.4. (continued). Calculated whole rock mineralogical compositions from integrating QXRD and EPMA data compared against measured values for Lord Brassey samples.

14LBM1-5 Oxide	SUM wt%	Absolute Error wt%	XRF wt%	Absolute Error wt%	Absolute Error wt%	Relative Error %
LOI_V	10.907	0.443	11.358	0.035	0.451	3.968
Al_2O_3	3.922	3.977	3.540	0.014	0.382	10.791
CaO	4.608	0.527	7.580	0.010	2.972	39.208
Cr_2O_3	0.676	0.749	1.010	0.010	0.334	33.069
Fe_2O_3	7.911	4.075	9.010	0.021	1.099	12.198
K_2O	0.007	0.014	0.000	0.010	0.007	
MgO	33.206	4.458	28.130	0.057	5.076	18.045
Mn_3O_4	0.129	0.101	0.170	0.007	0.041	24.118
Na_2O	0.006	0.027	0.030	0.007	0.024	80.000
P_2O_5	0.000	0.000	0.000	0.007	0.000	
SiO_2	37.885	3.389	38.600	0.010	0.715	1.852
TiO_2	0.017	0.043	0.010	0.010	0.007	70.000
V_2O_5	0.003	0.004	0.000	0.050	0.003	
NiO	0.267	0.934	0.197	0.003	0.070	35.360
SUM	99.544	8.106	99.635	0.091	0.091	0.091

Table A.4. (continued). Calculated whole rock mineralogical compositions from integrating QXRD and EPMA data compared against measured values for Lord Brassey samples.

14LBM1-9	Lizardite	Antigorite	Andradite	Grossular	Clinochlore	Brucite	Chromite	Magnetite	Jianshuiite
Oxide	wt%	wt%	wt%	wt%	wt%	wt%	wt%	wt%	wt%
LOI_V	8.254	2.840	0.079	0.020	0.439	0.110	0.000	0.000	0.036
Al_2O_3	3.860	1.328	0.190	0.049	0.584	0.000	0.101	0.001	0.000
CaO	0.060	0.021	1.648	0.425	0.014	0.000	0.001	0.000	0.002
Cr_2O_3	0.089	0.031	0.003	0.001	0.002	0.000	0.360	0.009	0.000
Fe_2O_3	3.480	1.197	1.255	0.323	0.314	0.000	0.274	1.135	0.001
K_2O	0.006	0.002	0.000	0.000	0.000	0.000	0.000	0.000	0.001
MgO	25.281	8.699	0.020	0.005	1.089	0.245	0.049	0.004	0.011
Mn_3O_4	0.071	0.024	0.003	0.001	0.006	0.000	0.003	0.001	0.192
Na_2O	0.004	0.001	0.001	0.000	0.002	0.000	0.000	0.000	0.002
P_2O_5	0.000	0.000	0.000	0.000	0.000	0.000	0.000	0.000	0.000
SiO_2	24.477	8.423	1.659	0.427	1.096	0.000	0.001	0.006	0.000
TiO_2	0.004	0.001	0.011	0.003	0.002	0.000	0.002	0.000	0.000
V_2O_5	0.000	0.000	0.003	0.001	0.000	0.000	0.002	0.000	0.000
NiO	0.079	0.027	0.000	0.000	0.001	0.000	0.001	0.002	0.012
SUM	65.665	22.594	4.872	1.255	3.549	0.355	0.794	1.158	0.257

Table A.4. (continued). Calculated whole rock mineralogical compositions from integrating QXRD and EPMA data compared against measured values for Lord Brassey samples.

14LBM1-9 Oxide	SUM wt%	Absolute Error wt%	XRF wt%	Absolute Error wt%	Absolute Error wt%	Relative Error %
LOI_V	11.778	0.525	13.627	0.035	1.849	13.571
Al_2O_3	6.113	2.138	5.890	0.014	0.223	3.786
CaO	2.171	0.598	2.310	0.010	0.139	6.017
Cr_2O_3	0.495	0.474	0.630	0.010	0.135	21.429
Fe_2O_3	7.979	2.717	8.990	0.021	1.011	11.246
K_2O	0.009	0.007	0.000	0.010	0.009	
MgO	35.403	3.144	31.240	0.057	4.163	13.326
Mn_3O_4	0.301	0.780	0.170	0.007	0.131	77.059
Na_2O	0.010	0.020	0.040	0.007	0.030	75.000
P_2O_5	0.000	0.000	0.000	0.007	0.000	
SiO_2	36.089	2.093	35.660	0.010	0.429	1.203
TiO_2	0.023	0.036	0.080	0.010	0.057	71.250
V_2O_5	0.006	0.005	0.020	0.050	0.014	70.000
NiO	0.122	0.053	0.152	0.003	0.030	19.843
SUM	100.499	5.261	98.809	0.091	1.690	1.710

Table A.4. (continued). Calculated whole rock mineralogical compositions from integrating QXRD and EPMA data compared against measured values for Lord Brassey samples.

14LBM1-10	Lizardite	Antigorite	Andradite	Clinochlore	Chromite	Magnetite
Oxide	wt%	wt%	wt%	wt%	wt%	wt%
LOI_V	9.032	2.460	0.089	0.252	0.000	0.000
Al_2O_3	2.279	0.621	0.102	0.272	0.087	0.000
CaO	0.044	0.012	1.885	0.001	0.001	0.000
Cr_2O_3	0.470	0.128	0.054	0.022	0.308	0.005
Fe_2O_3	4.366	1.189	1.452	0.104	0.235	0.666
K_2O	0.013	0.003	0.000	0.000	0.000	0.000
MgO	27.057	7.369	0.025	0.685	0.042	0.002
Mn_3O_4	0.116	0.032	0.003	0.001	0.003	0.000
Na_2O	0.016	0.004	0.001	0.000	0.000	0.000
P_2O_5	0.000	0.000	0.000	0.000	0.000	0.000
SiO_2	28.040	7.637	1.896	0.668	0.000	0.003
TiO_2	0.006	0.001	0.109	0.000	0.002	0.000
V_2O_5	0.000	0.000	0.007	0.000	0.002	0.000
NiO	0.100	0.027	0.000	0.003	0.000	0.001
SUM	71.539	19.483	5.623	2.008	0.680	0.677

Table A.4. (continued). Calculated whole rock mineralogical compositions from integrating QXRD and EPMA data compared against measured values for Lord Brassey samples.

14LBM1-10 Oxide	SUM wt%	Absolute Error wt%	XRF wt%	Absolute Error wt%	Absolute Error wt%	Relative Error %
LOI_V	11.833	0.428	12.620	0.035	0.787	6.236
Al_2O_3	3.361	1.805	1.420	0.014	1.941	136.690
CaO	1.943	0.380	3.210	0.010	1.267	39.470
Cr_2O_3	0.987	0.657	0.670	0.010	0.317	47.313
Fe_2O_3	8.012	3.031	8.670	0.021	0.658	7.589
K_2O	0.016	0.012	0.000	0.010	0.016	
MgO	35.180	2.584	31.890	0.057	3.290	10.317
Mn_3O_4	0.155	0.038	0.200	0.007	0.045	22.500
Na_2O	0.021	0.021	0.020	0.007	0.001	5.000
P_2O_5	0.000	0.000	0.000	0.007	0.000	
SiO_2	38.244	1.752	39.810	0.010	1.566	3.934
TiO_2	0.118	0.133	0.010	0.010	0.108	1080.000
V_2O_5	0.009	0.009	0.000	0.050	0.009	
NiO	0.131	0.061	0.330	0.003	0.199	60.286
SUM	100.010	4.793	98.850	0.091	1.160	1.174

Table A.4. (continued). Calculated whole rock mineralogical compositions from integrating QXRD and EPMA data compared against measured values for Lord Brassey samples.

14LBM1-19 Oxide	Lizardite wt%	Antigorite wt%	Andradite wt%	Clinochlore wt%	Chromite wt%
LOI_V	9.224	2.396	0.009	0.253	0.000
Al_2O_3	2.234	0.580	0.015	0.309	0.747
CaO	0.049	0.013	0.211	0.002	0.008
Cr_2O_3	0.269	0.070	0.004	0.013	2.653
Fe_2O_3	3.681	0.956	0.169	0.130	2.019
K_2O	0.005	0.001	0.000	0.000	0.000
MgO	28.372	7.371	0.002	0.668	0.363
Mn_3O_4	0.109	0.028	0.000	0.002	0.022
Na_2O	0.005	0.001	0.000	0.000	0.001
P_2O_5	0.000	0.000	0.000	0.000	0.000
SiO_2	28.362	7.368	0.214	0.646	0.004
TiO_2	0.006	0.002	0.003	0.000	0.016
V_2O_5	0.000	0.000	0.000	0.000	0.017
NiO	0.124	0.032	0.000	0.003	0.004
SUM	72.440	18.818	0.627	2.026	5.854

Table A.4. (continued). Calculated whole rock mineralogical compositions from integrating QXRD and EPMA data compared against measured values for Lord Brassey samples.

14LBM1-19	SUM	Absolute Error	XRF	Absolute Error	Absolute Error	Relative Error
Oxide	wt%	wt%	wt%	wt%	wt%	%
LOI_V	11.882	0.453	13.497	0.035	1.615	11.968
Al_2O_3	3.885	4.336	0.950	0.014	2.935	308.947
CaO	0.283	0.480	0.020	0.010	0.263	1315.000
Cr_2O_3	3.009	0.801	0.320	0.010	2.689	840.313
Fe_2O_3	6.955	4.308	12.700	0.021	5.745	45.236
K_2O	0.006	0.015	0.000	0.010	0.006	
MgO	36.776	4.842	34.260	0.057	2.516	7.344
Mn_3O_4	0.161	0.110	0.110	0.007	0.051	46.364
Na_2O	0.007	0.030	0.030	0.007	0.023	76.667
P_2O_5	0.000	0.000	0.000	0.007	0.000	
SiO_2	36.594	3.613	36.260	0.010	0.334	0.921
TiO_2	0.027	0.051	0.000	0.010	0.027	
V_2O_5	0.017	0.011	0.000	0.050	0.017	
NiO	0.163	0.205	0.248	0.003	0.085	34.349
SUM	99.765	8.660	98.395	0.091	1.370	1.392

Table A.4. (continued). Calculated whole rock mineralogical compositions from integrating QXRD and EPMA data compared against measured values for Lord Brassey samples.

14LBM1-21	Lizardite	Antigorite	Andradite	Clinochlore	Chromite	Magnetite
Oxide	wt%	wt%	wt%	wt%	wt%	wt%
LOI_V	9.887	1.910	0.018	0.224	0.000	0.000
Al_2O_3	1.439	0.278	0.033	0.253	0.143	0.002
CaO	0.020	0.004	0.577	0.001	0.000	0.002
Cr_2O_3	0.131	0.025	0.008	0.000	0.325	0.028
Fe_2O_3	2.986	0.577	0.485	0.140	0.194	3.129
K_2O	0.001	0.000	0.000	0.000	0.000	0.000
MgO	31.625	6.110	0.005	0.593	0.074	0.006
Mn_3O_4	0.075	0.015	0.002	0.003	0.002	0.003
Na_2O	0.001	0.000	0.000	0.000	0.000	0.000
P_2O_5	0.000	0.000	0.000	0.000	0.000	0.000
SiO_2	29.585	5.716	0.594	0.569	0.000	0.014
TiO_2	0.003	0.001	0.003	0.000	0.001	0.000
V_2O_5	0.000	0.000	0.001	0.000	0.002	0.000
NiO	0.168	0.032	0.000	0.002	0.001	0.001
SUM	75.921	14.668	1.726	1.785	0.742	3.185

Table A.4. (continued). Calculated whole rock mineralogical compositions from integrating QXRD and EPMA data compared against measured values for Lord Brassey samples.

14LBM1-21	SUM	Absolute Error	XRF	Absolute Error	Absolute Error	Relative Error
Oxide	wt%	wt%	wt%	wt%	wt%	%
LOI_V	12.039	0.389	14.109	0.035	2.070	14.671
Al_2O_3	2.148	1.107	2.620	0.014	0.472	18.015
CaO	0.604	0.371	1.040	0.010	0.436	41.923
Cr_2O_3	0.517	0.465	0.910	0.010	0.393	43.187
Fe_2O_3	7.511	1.391	9.950	0.021	2.439	24.513
K_2O	0.001	0.003	0.000	0.010	0.001	
MgO	38.413	1.365	33.730	0.057	4.683	13.884
Mn_3O_4	0.100	0.030	0.130	0.007	0.030	23.077
Na_2O	0.001	0.005	0.030	0.007	0.029	96.667
P_2O_5	0.000	0.000	0.000	0.007	0.000	
SiO_2	36.478	1.388	36.040	0.010	0.438	1.215
TiO_2	0.008	0.010	0.010	0.010	0.002	20.000
V_2O_5	0.003	0.002	0.000	0.050	0.003	
NiO	0.204	0.056	0.212	0.003	0.008	3.774
SUM	98.027	2.731	98.781	0.091	0.754	0.763

Table A.4. (continued). Calculated whole rock mineralogical compositions from integrating QXRD and EPMA data compared against measured values for Lord Brassey samples.

14LBM1-28	Lizardite	Antigorite	Andradite	Grossular	Clinochlore	Chromite	Magnetite
Oxide	wt%	wt%	wt%	wt%	wt%	wt%	wt%
LOI_V	8.153	2.192	0.169	0.027	1.100	0.000	0.000
Al_2O_3	2.086	0.561	0.031	0.005	1.291	0.016	0.000
CaO	0.031	0.008	2.380	0.387	0.001	0.000	0.000
Cr_2O_3	0.341	0.092	0.046	0.008	0.082	0.167	0.005
Fe_2O_3	3.645	0.980	2.076	0.338	0.416	0.189	0.798
K_2O	0.002	0.001	0.000	0.000	0.001	0.000	0.000
MgO	24.638	6.623	0.016	0.003	2.980	0.008	0.004
Mn_3O_4	0.116	0.031	0.001	0.000	0.003	0.002	0.000
Na_2O	0.000	0.000	0.000	0.000	0.000	0.000	0.000
P_2O_5	0.000	0.000	0.000	0.000	0.000	0.000	0.000
SiO_2	24.635	6.623	2.269	0.369	2.805	0.001	0.004
TiO_2	0.012	0.003	0.049	0.008	0.001	0.002	0.000
V_2O_5	0.000	0.000	0.002	0.000	0.000	0.002	0.000
NiO	0.154	0.041	0.000	0.000	0.022	0.000	0.002
SUM	63.813	17.155	7.039	1.145	8.702	0.387	0.813

Table A.4. (continued). Calculated whole rock mineralogical compositions from integrating QXRD and EPMA data compared against measured values for Lord Brassey samples.

14LBM1-28 Oxide	SUM wt%	Absolute Error wt%	XRF wt%	Absolute Error wt%	Absolute Error wt%	Relative Error %
LOI_V	11.641	0.398	12.650	0.035	1.009	7.976
Al_2O_3	3.990	2.625	3.020	0.014	0.970	32.119
CaO	2.807	0.534	3.430	0.010	0.623	18.163
Cr_2O_3	0.741	0.570	0.960	0.010	0.219	22.813
Fe_2O_3	8.442	1.755	8.020	0.021	0.422	5.262
K_2O	0.004	0.004	0.000	0.010	0.004	
MgO	34.272	2.271	31.820	0.057	2.452	7.706
Mn_3O_4	0.153	0.040	0.140	0.007	0.013	9.286
Na_2O	0.000	0.001	0.020	0.007	0.020	100.000
P_2O_5	0.000	0.000	0.000	0.007	0.000	
SiO_2	36.706	2.301	38.080	0.010	1.374	3.608
TiO_2	0.075	0.068	0.010	0.010	0.065	650.000
V_2O_5	0.004	0.005	0.010	0.050	0.006	60.000
NiO	0.219	0.165	0.206	0.003	0.013	6.311
SUM	99.054	4.607	98.366	0.091	0.688	0.699

Table A.4. (continued). Calculated whole rock mineralogical compositions from integrating QXRD and EPMA data compared against measured values for Lord Brassey samples.

14LBM1-31	Lizardite	Antigorite	Andradite	Clinochlore	Chromite	Heazlewoodite	Awaruite
Oxide	wt%	wt%	wt%	wt%	wt%	wt%	wt%
LOI_V	9.472	1.615	0.008	0.766	0.000	0.000	0.000
Al_2O_3	2.294	0.391	0.014	0.934	0.723	0.000	0.000
CaO	0.050	0.009	0.200	0.007	0.007	0.000	0.000
Cr_2O_3	0.276	0.047	0.004	0.038	2.569	0.000	0.000
Fe_2O_3	3.779	0.645	0.160	0.393	1.955	0.003	0.070
K_2O	0.005	0.001	0.000	0.001	0.000	0.000	0.000
MgO	29.135	4.968	0.002	2.021	0.352	0.000	0.000
Mn_3O_4	0.112	0.019	0.000	0.005	0.021	0.000	0.000
Na_2O	0.005	0.001	0.000	0.001	0.001	0.000	0.000
P_2O_5	0.000	0.000	0.000	0.000	0.000	0.000	0.000
SiO_2	29.124	4.967	0.202	1.952	0.004	0.000	0.000
TiO_2	0.006	0.001	0.003	0.001	0.016	0.000	0.000
V_2O_5	0.000	0.000	0.000	0.000	0.017	0.000	0.000
NiO	0.128	0.022	0.000	0.008	0.004	0.124	0.191
SUM	74.386	12.686	0.593	6.127	5.669	0.127	0.261

Table A.4. (continued). Calculated whole rock mineralogical compositions from integrating QXRD and EPMA data compared against measured values for Lord Brassey samples.

14LBM1-31	SUM	Absolute Error	XRF	Absolute Error	Absolute Error	Relative Error
Oxide	wt%	wt%	wt%	wt%	wt%	%
LOI_V	11.861	0.454	12.719	0.035	0.858	6.746
Al_2O_3	4.356	4.377	1.680	0.014	2.676	159.286
CaO	0.273	0.481	0.020	0.010	0.253	1265.000
Cr_2O_3	2.934	0.805	0.720	0.010	2.214	307.500
Fe_2O_3	7.005	4.357	11.870	0.021	4.865	40.986
K_2O	0.007	0.015	0.000	0.010	0.007	
MgO	36.478	4.882	34.050	0.057	2.428	7.131
Mn_3O_4	0.157	0.111	0.110	0.007	0.047	42.727
Na_2O	0.008	0.031	0.010	0.007	0.002	20.000
P_2O_5	0.000	0.000	0.010	0.007	0.010	100.000
SiO_2	36.249	3.643	36.540	0.010	0.291	0.796
TiO_2	0.027	0.051	0.010	0.010	0.017	170.000
V_2O_5	0.017	0.010	0.000	0.050	0.017	
NiO	0.477	1.322	0.914	0.003	0.437	47.812
SUM	99.849	8.838	98.653	0.091	1.196	1.212

Table A.4. (continued). Calculated whole rock mineralogical compositions from integrating QXRD and EPMA data compared against measured values for Lord Brassey samples.

14LBM1-32 Oxide	Lizardite wt%	Antigorite wt%	Andradite wt%	Clinochlore wt%	Brucite wt%	Chromite wt%
LOI_V	9.357	2.486	0.006	0.245	0.125	0.000
Al_2O_3	2.267	0.602	0.011	0.299	0.000	0.492
CaO	0.049	0.013	0.154	0.002	0.000	0.005
Cr_2O_3	0.273	0.072	0.003	0.012	0.000	1.747
Fe_2O_3	3.734	0.992	0.123	0.126	0.000	1.330
K_2O	0.005	0.001	0.000	0.000	0.000	0.000
MgO	28.783	7.648	0.002	0.647	0.280	0.239
Mn_3O_4	0.110	0.029	0.000	0.002	0.000	0.014
Na_2O	0.005	0.001	0.000	0.000	0.000	0.000
P_2O_5	0.000	0.000	0.000	0.000	0.000	0.000
SiO_2	28.773	7.645	0.156	0.625	0.000	0.003
TiO_2	0.006	0.002	0.002	0.000	0.000	0.011
V_2O_5	0.000	0.000	0.000	0.000	0.000	0.011
NiO	0.126	0.034	0.000	0.003	0.000	0.003
SUM	73.488	19.525	0.457	1.961	0.405	3.855

Table A.4. (continued). Calculated whole rock mineralogical compositions from integrating QXRD and EPMA data compared against measured values for Lord Brassey samples.

14LBM1-32 Oxide	SUM wt%	Absolute Error wt%	XRF wt%	Absolute Error wt%	Absolute Error wt%	Relative Error %
LOI_V	12.219	0.550	14.710	0.035	2.491	16.934
Al_2O_3	3.671	4.404	1.520	0.014	2.151	141.513
CaO	0.223	0.483	0.230	0.010	0.007	3.043
Cr_2O_3	2.107	0.794	0.530	0.010	1.577	297.547
Fe_2O_3	6.305	4.372	9.290	0.021	2.985	32.131
K_2O	0.006	0.015	0.000	0.010	0.006	
MgO	37.599	4.963	35.120	0.057	2.479	7.059
Mn_3O_4	0.155	0.112	0.180	0.007	0.025	13.889
Na_2O	0.006	0.031	0.020	0.007	0.014	70.000
P_2O_5	0.000	0.000	0.000	0.007	0.000	
SiO_2	37.202	3.664	36.550	0.010	0.652	1.784
TiO_2	0.021	0.049	0.010	0.010	0.011	110.000
V_2O_5	0.011	0.007	0.010	0.050	0.001	10.000
NiO	0.166	0.209	0.239	0.003	0.073	30.544
SUM	99.691	8.820	98.409	0.091	1.282	1.303